DESIGN PRINCIPLES OF A BROADBAND SINGLE-SHOT TRANISENT ABSORPTION SPECTROMETER

by

KELLY S. WILSON

A DISSERTATION

Presented to the Department of Chemistry and Biochemistry
and the Graduate School of the University of Oregon
in partial fulfillment of the requirements
for the degree of
Doctor of Philosophy

December 2020

DISSERTATION APPROVAL PAGE

Student: Kelly S. Wilson

Title: Design Principles of a Single-Shot Transient Absorption Spectrometer

This dissertation has been accepted and approved in partial fulfillment of the requirements for the Doctor of Philosophy degree in the Department of Chemistry and Biochemistry by:

Jeffrey A. Cina	Chairperson
Cathy Y. Wong	Advisor
Mark C. Lonergan	Core Member
Michael G. Raymer	Institutional Representative

and

Kate Mondloch Interim Vice Provost and Dean of the Graduate School

Original approval signatures are on file with the University of Oregon Graduate School.

Degree awarded December 2020

DISSERTATION ABSTRACT

Kelly S. Wilson

Doctor of Philosophy

Department of Chemistry and Biochemistry

December 2020

Title: Design Principles of a Broadband Single-Shot Transient Absorption Spectrometer

Single-shot transient absorption (SSTA) spectroscopy overcomes the limitations of conventional transient absorption (TA) instruments by spatially encoding the pump-probe time delay into the probe spatial profile. This enables the measurement of excited state dynamics of systems that evolve on time scales below the acquisition time of typical TA instruments. This dissertation describes techniques used to spatially encode the time delay and design principles that must be followed to accurately measure the excited state dynamics. Presented herein is the design and implementation of a homebuilt broadband SSTA instrument with a 60-ps time delay range and 100-nm spectral range capable of acquiring a transient spectrum within a few seconds. This instrument achieves the largest time delay range of any previously reported SSTA instrument.

This range is achieved through the use of a spatial light modulator which reshapes each beam to a flat-top profile, enabling a uniform excitation density and maintaining a good signal-to-noise ratio throughout the spatially encoded delay. A homebuilt, user-friendly software controls a range of scientific equipment, acquires and processes data at high acquisition rates, and corrects for evolving scatter and photoluminescence during SSTA measurements. Techniques are introduced that calibrate the spatial time delay and

spectral axes of the instrument and correct for deviations in the signal caused by variations in the pump profile.

Presented SSTA measurements of chemical systems exemplify research questions in materials science that can only be addressed using SSTA. First-ever SSTA measurements during film formation reveal an intermediate, highly fluorescent aggregates of pseudoisocyanine iodide with different excited state dynamics from the fully formed film. Measurements of hybrid organic-inorganic perovskite nanocrystals (NCs) reveal a transient spectral feature that reports on the surface quality of growing NCs. Preliminary TA measurements of organic electron donor:acceptor systems are presented and will direct future in situ SSTA measurements during thin film formation and thermal annealing. This instrument is capable of measuring the excited state dynamics of evolving systems like these and, for the first time, will provide insight into the relationship between intermediate excited state dynamics and other structural and photophysical characteristics.

This dissertation includes previously published and unpublished co-authored material.

CURRICULUM VITAE

NAME OF AUTHOR: Kelly S. Wilson

GRADUATE AND UNDERGRADUATE SCHOOLS ATTENDED

University of Oregon, Eugene
Brigham Young University – Idaho, Rexburg

DEGREES AWARDED

Doctor of Philosophy, Chemistry, 2020, University of Oregon
Bachelor of Science, Chemistry, 2014, Brigham Young University – Idaho

AREAS OF SPECIAL INTEREST

Ultrafast Spectroscopy
Python Programming
Instrumental Design and Control

PROFESSIONAL EXPERIENCE

Graduate Research Assistant, University of Oregon, 2015-present

Graduate Teaching Assistant, University of Oregon, 2014-2015, 2019

Adjunct Faculty Member, Brigham Young University – Idaho, 2014

GRANTS, AWARDS, AND HONORS

Travel Award from the Community for Minorities in STEM, University of Oregon, 2018

Nielson Scholarship, Brigham Young University – Idaho, 2013

PUBLICATIONS

Sadighian, J. C.; Wilson, K. S.; Crawford, M. L.; Wong, C. Y. Evolving Stark Effect During Growth of Perovskite Nanocrystals Measured Using

Transient Absorption. *Front. Chem.* **2020**, *8*. https://doi.org/10.3389/fchem.2020.585853.

Wilson, K. S.; Mapile, A. N.; Wong, C. Y.; Wong, C. Y.; Wong, C. Y. Broadband Single-Shot Transient Absorption Spectroscopy. *Opt. Express, OE* **2020**, *28* (8), 11339–11355. https://doi.org/10.1364/OE.390938.

Wilson, K. S.; Scott, M. N.; Wong, C. Y. Excited State Dynamics of Organic Semiconductors Measured with Shot-to-Shot Correction of Scatter and Photoluminescence. *Synthetic Metals* **2019**, *250*, 115–120. https://doi.org/10.1016/j.synthmet.2019.03.007.

Wilson, K. S.; Wong, C. Y. In Situ Measurement of Exciton Dynamics During Thin-Film Formation Using Single-Shot Transient Absorption. *J. Phys. Chem. A* **2018**, *122* (31), 6438–6444. https://doi.org/10.1021/acs.jpca.8b06248.

Wilson, K. S.; Scott, M. N.; Wong, C. Y. Single-Shot Transient Absorption Spectroscopy of an Organic Film. *MRS Advances* **2018**, *3* (59), 3453–3457. https://doi.org/10.1557/adv.2018.402.

Wilson, K. S.; Wong, C. Y. Single-Shot Transient Absorption Spectroscopy with a 45 Ps Pump-Probe Time Delay Range. *Opt. Lett., OL* **2018**, *43* (3), 371–374. https://doi.org/10.1364/OL.43.000371.

ACKNOWLEDGEMENTS

I thank Professor Cathy Wong for her continuous and valuable mentorship throughout my PhD. She took the risk of accepting me as her first graduate student with hardly even knowing me and allowing me to use Python for everything in the lab. Thanks goes to James Sadighian, Morgan Sosa, Michael Crawford, Madelyn Scott, and Zack Walbrun who all taught me valuable research skills and were great friends. Professor Hector Becerril taught me Python and showed me the wonders of physical chemistry. He inspired me to go to graduate school, encouraged me to write a Python book, and even let me teach a Programming for Chemists class.

My greatest blessings and support have been my wife Diana and four boys, Maxwell, Wesley, Pascal, and Lewis. I would not be the type of person I am today without them. I thank my parents, Kent and Liz, and Diana's parent, Chad and Christine, for always being there and teaching me humility, faith, and hard work.

This material is based upon work supported by the National Science Foundation under Grant No. 1752129. Acknowledgement is made to the Donors of the American Chemical Society Petroleum Research Fund for partial support of this research, 59424-DNI6.

This work is dedicated to Diana L. Wilson who supported me at every step.

TABLE OF CONTENTS

Chapter Page

Chapter Page

LIST OF FIGURES

Figure Page

Figure Page

CHAPTER I

INTRODUCTION TO SINGLE-SHOT TRANSIENT ABSORPTION SPECTROSCOPY TECHNIQUES AND PRINCIPLES

Includes unpublished co-authored material.

Zachary S. Walbrun designed four data figures in "SSTA Instrumental Design Principles" from data we collected together and analyzed using code that I wrote. Cathy Y. Wong provided editorial direction and assistance. Martin D. Gruber collected spectra and power measurements for the broadband probe generated in sapphire and argon media.

Introduction

Transient absorption (TA) is an ultrafast spectroscopic technique capable of monitoring the dynamics of short-lived electronically excited species. In this spectroscopy a pump pulse photoexcites a small fraction of the resonant species in a sample. A second probe pulse is used to measure the absorption of the system, and transient differential absorbance is obtained by comparing the absorption with and without the pump excitation. The differential absorbance can be used to identify transient populations of excited states since the absorbance lineshape of these states will differ from the ground state. The focus of this review is on the development and design principles of advanced TA techniques that can rapidly perform these measurements of photo-induced dynamics in unstable, evolving systems. This can enable the measurement of TA in situ, during some chemical or structural change, to provide insight on the impact of these changes on photo-induced dynamics.

TA signal can originate from both emissive and non-emissive excited states, making this spectroscopy useful for investigating excited state dynamics and fundamental processes that cannot be measured using time-resolved photoluminescence-based

spectroscopic techniques. TA instruments that can measure static samples that return to the same state before subsequent TA measurements are relatively simple to design and are now commercially available. This, along with the generally straightforward interpretation of typical TA data, has enabled the widespread use of TA spectroscopy in biological, chemical, and materials research. The capability of TA to answer a range of scientific questions in such systems is highlighted in the following examples. TA measurements of photosynthetic systems explained the processes of natural light-harvesting and photoprotective mechanisms.[1,2] After the photoexcitation of chlorophyll, a transient bleaching feature characteristic of the first excited state of chlorophyll rapidly decayed concomitant with the growth of features ascribed to a carotenoid excited state. This gave evidence of energy transfer between chlorophyll and the carotenoids, with the carotenoids then dissipating the excess energy to prevent photodegradation. TA can also be used to tune chemical design. Supramolecular assemblies of multiple dyes and fullerene derivatives can potentially be used as synthetic light harvesting complexes.[3] TA signals at different wavelengths correspond to excited state populations in each subunit in the complex, enabling the measurement of energy transfer rates between subunits. TA has been used to tune energy transfer rates by varying peripheral side chains, interunit lengths, and conjugation properties. The development of innovative photovoltaic materials has also been supported by TA. For example, TA spectroscopy was used to measure long-range electron and hole transport in solution-processed perovskite solar cells.[4] TA measurements of the perovskite with either an electron or hole extracting material identified the carrier dynamics in the perovskite. Diffusion lengths were determined by correlating the extraction time of electrons and holes obtained from TA

measurements with the thickness of the perovskite layer. TA can also provide design rules for materials, for example the choice of electron donor and acceptor materials in a bulk heterojunction for organic photovoltaic systems.[5] The growth of TA features associated with charge-transfer states have been correlated with the energy offset at the donor-acceptor interface to find that a low interfacial energy offset and a charge transfer state hybridized with a highly emissive local excited state will lead to more efficient organic photovoltaics. These examples, just a few from tens of thousands of studies that have utilized laser-based pump-probe measurements since its inception in the 1960s, demonstrate the value of this technique as a probe of systems involving excited species.

In these examples, as is typical for TA studies, the primary use of this time-resolved spectroscopy is the measurement of dynamics. The differential absorbance at any particular time delay between the pump and probe pulses holds limited information about the excited states. Instead, it is the *change* in the differential absorbance as a function of pump-probe time delay that can report on excited state dynamics. The time delay between the pump and probe pulses is varied to achieve a transient spectrum and track the evolving populations of different excited states. The time delay between the pump and probe pulses is typically controlled by changing the pathlength of one of the two beams using a retroreflector mounted onto a motorized translation stage. A transient spectrum is acquired by measuring the pump-induced changes to the probe transmission that, after analysis, reveals the excited state dynamics of the measured system. To acquire spectra at a sufficient number of pump-probe time delays to capture the dynamics of the relevant processes, spectra are measured at a range of translation stage positions and these measurements are repeated to attain an adequate signal-to-noise ratio (SNR). Even

with continual improvement in the stability of pulsed laser sources, significantly shorter data acquisition times have not been achieved owing to the time required to scan the stage. The minutes-to-hours needed to acquire a typical transient spectrum significantly restricts TA spectroscopy to systems that are stable for the duration of the measurement.[6]

Rapid acquisition of TA spectra is required to accurately characterize the excited state dynamics of unstable systems. This allows TA spectra to be measured in situ, during chemical or structural changes, joining a variety of characterization modalities that have aided in the understanding of evolving or unstable systems. For example, in situ absorbance and grazing incidence x-ray diffraction have been used to characterize methylammonium lead iodide perovskite degradation during exposure to humidity to find humidity-dependent degradation rates and the formation of an intermediate hydrated crystalline phase [7]. These observations are only possible with in situ measurements. Another example is the use of NMR in situ during lithium battery recharge cycles to characterize the formation of metallic lithium microstructures on the electrode that degrade the battery and can increase a risk of fire or explosion.[8] In situ measurements were required to observe the formation and shift of NMR peaks characteristic of lithium microstructures during each discharge/recharge cycle. In each of these evolving systems, the electronic structure likely co-evolves with the other properties that can be measured using in situ techniques. Considering that excited state dynamics can determine the functionality of a biological, chemical, or material system, it can be valuable to measure excited state dynamics in situ during structural or chemical change. The evolving dynamics can be determined in situ, during such changes, if TA measurements at all pump-probe time delays can be simultaneously acquired during sample evolution. A

sample will not have time to significantly change during the process of TA signal acquisition if a detector can simultaneously measure the transient signal from a range of time delays by somehow encoding the time delay information into a single pulse. Single-shot transient absorption (SSTA) techniques have been developed for this purpose. This article reviews the history of single-shot time-resolved measurements, dominant techniques used in modern SSTA instruments to encode the pump-probe time delay with a focus on spatial encoding, and design principles necessary for the application and use of such instruments.

Single-Shot Transient Absorption Techniques

Single-shot transient absorption techniques seek to acquire a transient in a single shot by measuring the signal over a range of pump-probe time delays at the same time. The dominant strategy to accomplish this is by encoding the time delay into the spatial profile of the probe beam which is then imaged onto an array detector. Different spatial locations on the array detector correspond to different time delays. This removes the requirement of moving the translation stage to a new position for each time delay measurement which significantly reduces the acquisition time needed to attain an adequate SNR to a few seconds or, in some cases, a single shot. Furthermore, noise in the signal between different time delays caused by shot-to-shot laser fluctuations is reduced. The idea of collecting an entire transient spectrum at once is not new. In the late 1960s, not long after the development of Q-switched pulsed lasers, Malley and coworkers took advantage of the finite time required for light to travel through a sample to spatially encode a time delay range into a sample.[9] In their implementation, a pump beam saturated the excited state of a dye sample. A probe beam was then transmitted through

the sample perpendicular to the excitation path of the pump. Thus, different spatial locations along the probe profile were excited by the pump beam at different times. This resulted in different levels of transient photobleaching being mapped onto the intensity profile of the probe, which was then photographed. Not long after, they reported a second technique for spatially encoding the time delay range into the probe using a stair-step optic called an echelon.[10] The next two sections detail the geometry and design considerations inherent in both the angled beam and echelon techniques employed to spatially encode the pump-probe time delay. The following section briefly highlights an alternative method for encoding the time delay into the temporal profile of the probe beam. Fig. 1.1 reports the time delay range and resolution reported for various instruments by their reference number.

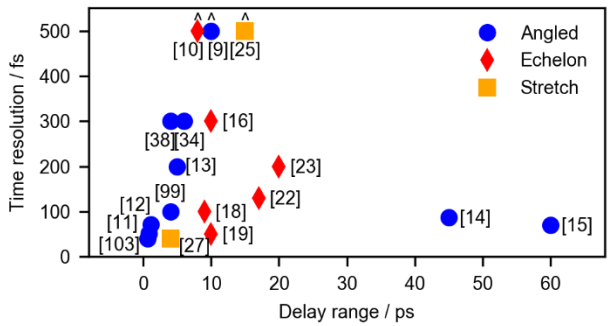

Fig. 1.1. Reported SSTA time delay ranges and time resolutions for instruments using angled beam (circle), echelon optic (diamond), and beam stretching (square) techniques. Labels refer to the reference number for each instrument. Instruments [9], [10], and [25] have a time resolution of 2, 6, and 1 ps, respectively.

Angled Beam Spatial Time Delay Encoding

The most extreme demonstration of the angled beam geometry used a pump and probe at a 90° angle,[9] shown in Fig. 1.2a. The pump propagates through the sample along one axis of a cuvette, while the probe propagates along another axis of the cuvette perpendicular to the pump. The probe is then imaged onto a photographic film where

different spatial locations on the film corresponded to different pump-probe time delays. In this orientation, the time delay range is determined by the propagation time of the pump beam across the sample region illuminated by the probe and is calculated as $t_{range} = d/c$ where d is the length of the pump-probe overlap region on the sample and c is the speed of light through the sample. This resulted in significant temporal smearing that lowered the time resolution. The time resolution may be limited by the time required for the probe to propagate through the sample in this geometry and is represented as $t_{res} = h/c$ where h is the thickness of the excited sample along the probe propagation axis. The time resolution of this instrument was significantly lower than the 1-ps pulse-width limited resolution attainable in typical TA measurements at the time. Another drawback to this geometry is that a sample must have a low optical density along the excitation axis, as the spectrum of the pump will change and become diminished as it passes through the sample. This will decrease and change the excited state population it generates along its trajectory which affects the measured dynamics.

In the late 1980s spatial encoding was used to autocorrelate 52-fs pulses using second harmonic generation (SHG) in a potassium dideuterium phosphate (KDP) crystal.[11] After interacting with a beam splitter, which creates two pulses of equal intensity, the pulses each travel along separate arms of an interferometer and are re-overlapped in the non-linear crystal. Instead of collinear alignment, which was common for autocorrelators at that time, or perpendicular alignment, as used by Malley, the wavefronts of the two incident beams are each at a 0.5° angle relative to the non-linear crystal, Fig. 1.2b. The beams are focused using cylindrical lenses such that the focal lines overlap spatially in the crystal. The intensity of SHG in the crystal depends on the spatial

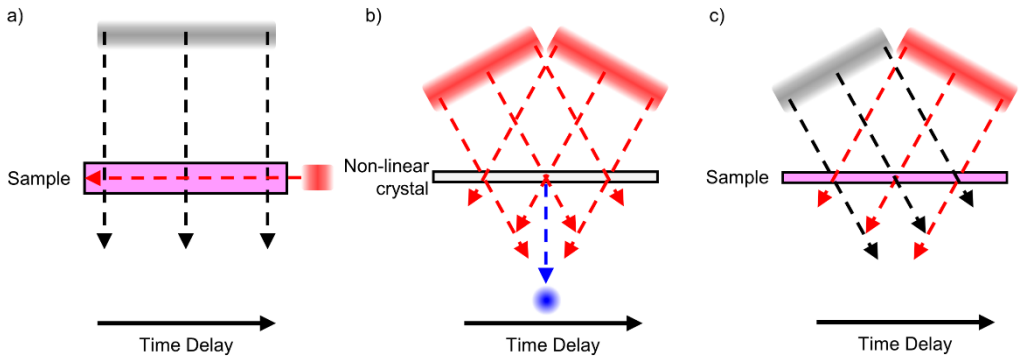

Fig. 1.2. Angled beam geometries used to spatially encode a time delay. Dashed arrows indicate beam propagation direction. Time delay is spatially encoded from left to right. a) Perpendicular geometry used in first reported SSTA measurements.[9] Pump (red) and probe (grey) transverse along perpendicular axes in the sample (pink). Time delay is encoded into the spatial profile of the probe beam. b) Beam geometry used in single-shot autocorrelators. Replicate beams (red) cross each other in a non-linear crystal at a small angle of incidence. Amplitude of SHG depends on the spatial and temporal overlap of the beams in the non-linear crystal and propagates along the bisector (blue) of the incident beam paths. c) SSTA beam geometry that encodes the time delay into the probe beam spatial profile and significantly improves time delay resolution compared to the geometry shown in (a).

and temporal overlap of the two beams. The SHG signal propagates along the bisector of the incident beams and is detected by an optical multichannel analyzer that images the KDP crystal. Pulse compression is determined by analyzing the spatial profile of the second harmonic signal. This operating principle is still used in many modern autocorrelators.

Dhar and coworkers performed SSTA measurements of an organic dye by applying the angled beam approach using a variation of the single-shot autocorrelator geometry, Fig. 1.2c.[12] A two-dimensional CCD detector imaged the probe beam at the sample, mapping the spatially encoded time delay along one axis of the detector. By employing a non-perpendicular orientation between the pump and probe, they were able to achieve a 1 ps time delay range with <50 fs resolution. Fig. 1.3a, which shows this same geometry, will be used to describe a generalized formula for the time delay range

using this technique. The probe (grey) and pump (red) are incident on the sample at angles of θ_{pr} and θ_{pu}, respectively. The size of the measured sample region of length d is determined by the size of the probe beam imaged by the detector. The time it takes for each beam to pass through the sample region (dashed) is calculated as the time difference between the arrival of each end of the beam onto the region and is calculated as $\Delta t = d \sin(\theta)/c$ where c is the speed of light. In this geometry, the time range is the sum of the time needed for each beam to cross the sample, $t_{range} = \Delta t_{pr} + \Delta t_{pu} = d[\sin(\theta_{pr}) + \sin(\theta_{pu})]/c$. The time resolution for this geometry is either determined by the pump and probe pulse durations or by the geometry of the incident beams and the sample thickness. Fig. 1.3b illustrates the impact of sample thickness on time resolution. The time required for the probe to traverse a sample of thickness h between the black dotted lines is $\Delta\tau_{pr} = h \cos(\theta_{pr})/c$. The pump interacts with the same region as it propagates between the red dotted lines, which requires a time of $\Delta\tau_{pu} = h\,|\cos(\theta_{pr}+\theta_{pu})|/[c\cos(\theta_{pr})]$. The time resolution is the difference between the propagation time for each beam across the region, $t_{res} = \Delta\tau_{pr} - \Delta\tau_{pu} = h\,[1 - |\cos(\theta_{pr}+\theta_{pu})|]/[c\cos(\theta_{pr})]$. Other factors such as focusing conditions and pixel width can influence the resolution as well.

SSTA instruments are not limited to measurements using a single-color probe. TA measurements using a broadband probe provide additional insights into excited state dynamic processes such as charge and energy transfer, as demonstrated by the examples previously.[1–5] In broadband SSTA instruments the probe beam is spectrally dispersed onto a 2D detector such that one axis records the spatially encoded time delay and the other records the spectral information. Furukawa et al. were the first to report a broadband SSTA instrument.[13] They reported a 5 ps time delay range and a wavelength

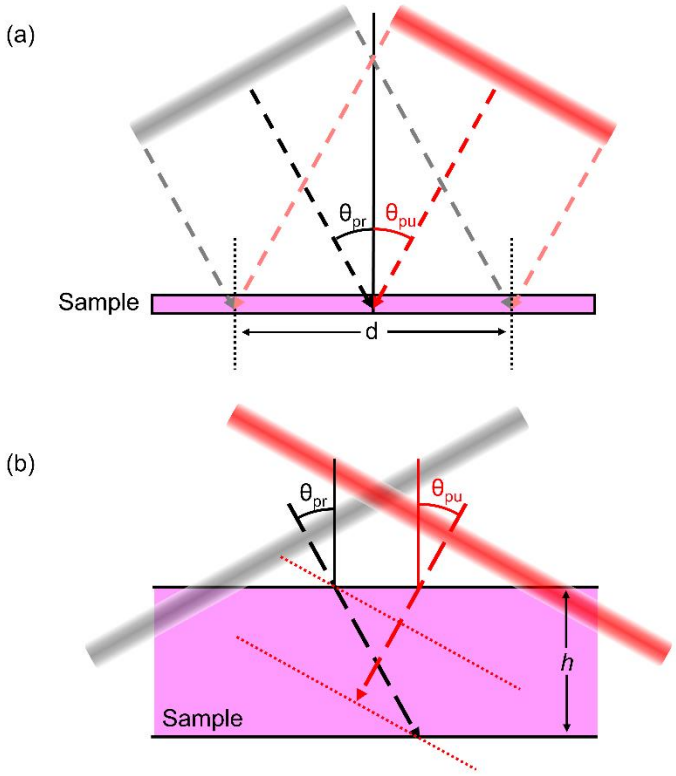

Fig. 1.3. Dependence of spatial time delay range (a) and resolution (b) on beam geometry. Probe (grey) and pump (red) beams are spatially overlapped onto a region of the sample (pink). Dashed arrows mark the propagation vectors of the beams. The incident angles of the probe, $\theta_{pr,}$ and pump, $\theta_{pu,}$ beams on the sample are indicated. (a) Dotted lines mark the edges of the pump-probe overlap region of length *d* imaged by the detector. Time delay range is the sum of the time required for each beam to propagate through the overlapped region. (b) Enlarged view of a sample of thickness *h* within the overlap region. A single spatial location of the probe profile indicated by the black dashed line is transmitted through the sample. Different spatial locations of the pump will photoexcite the probed sample between the red dotted lines. When pulse tilt and sample thickness limit the time resolution, the resolution is determined by the difference in time required by each beam to traverse the same region.

range from 420 to 620 nm with a data collection time of 30-60 s. They demonstrated agreement between SSTA and conventional TA measurements of the internal conversion of trans-β-carotene in benzene. We achieved the longest reported spatial time delay in any SSTA instrument for single-color measurements with a 45-ps time delay range [14] and were able to perform in situ SSTA measurements of an organic dye during dropcast film

formation.[6] We later reported the development of a broadband SSTA instrument with a 100 nm spectral range and 60 ps time delay range.[15]

Optical Echelon Spatial Time Delay Encoding

The time delay between pulses in TA instruments is commonly controlled by either changing the pathlength traveled by each pulse using a mirror mounted on a translation stage or by introducing different thicknesses of a high refractive index material into the beam path. Transmissive and reflective echelons apply these same techniques, but instead of applying the delay uniformly across the spatial profile of the beam, the delay is applied in incremental steps across the beam. This is accomplished by the stair-step structure in echelon optics as shown in Figs. 4a, 4b. An incident beam is split by each stair step in the echelon into a collection of pulses, each with its own time delay. In reflective echelons (Fig. 1.4a) the height of the stair step corresponds to a difference in pathlength created between neighboring pulses. The time delay step size is calculated as $\Delta t = 2\Delta x \sec(\theta)/c$ where Δx is the echelon step size, θ is the angle of incidence of the incoming probe beam, and c is the speed of light.[10] Similar to the reflective echelon, the time delay step size caused by a transmissive echelon (Fig. 1.4b) is dependent on the depth of each step. For a transmissive echelon, however, the delay is also dependent on the index of refraction, n, of the material in addition to the incident angle, θ, and step size, Δx, and is calculated as $\Delta t=(\Delta x/c)\,[(n^2 - \sin^2(\theta))^{1/2} - \cos(\theta)]$.[10] For both transmissive and reflective echelons, the time delay range induced by the echelon is determined by the number of steps and the depth of each step. The collection of delayed pulses is then focused onto the sample using a spherical lens, causing each pulse to pass through the same sample location, but at a different time, Fig. 1.4c. To avoid effects from

re-excitation of the sample from successive pump pulses, the echelon is always placed in the path of the probe beam and the probe pulse energy is lowered such that the ΔO.D. signal measured by each variably delayed probe pulse predominately results from excitation by the pump pulse and not from the excitation caused by preceding probe pulses. The pump and probe beams are overlapped in the sample, and a detector images the probe beam. Each stair step is evident in the image and its pump-probe time delay can be calibrated.

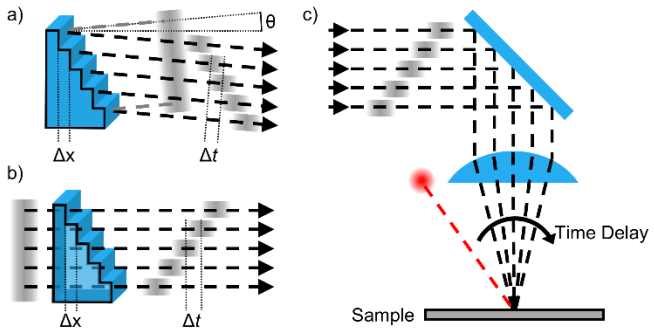

Fig. 1.4. Spatially encoded time delay using optical echelons with a step-size of Δ*x*. The probe (grey) is split into a collection of pulses with a delay step size of Δ*t*. a) Reflective echelon with probe incident angle of θ. b) Transmissive echelon. c) After reflecting off or transmitting through an echelon, a collection of probe pulses (grey) are focused using a spherical lens onto a sample. Time delay is encoded into the angle of incidence of each probe beam onto the sample. A pump beam (red) is spatially overlapped with the probe beams onto the sample.

After the initial use of an echelon for TA in 1971,[10] echelons were not reported in a single-shot setup until 2000 when Wakeham and Nelson reported a dual-echelon single-shot transient absorption instrument using two transmissive echelons.[16] One echelon induced a spatial time delay in the probe beam with 500-fs steps. The step axis of the second echelon was perpendicular to that of the first echelon and induced 25-fs time steps in the beam. This combination of echelons created a grid of probe pulses with coarse time delay from the first echelon along one axis and fine time delay from the second along the other axis. They imaged their grid of probe pulses onto a CCD camera and used images

with and without the pump exciting the sample to calculate a single-shot $\Delta T/T$ transient signal with 10 ps of time delay consisting of 400 time delay steps. With this, they performed the first measurements showing the change in transmission at the moment when pump-induced damage was caused in zinc titania glass and an explosive organic crystal, 1,3,3-trinitroazetidine.[17] These processes are irreversible, and thus could not be measured using a traditional TA instrument that relies on the sample returning to its original state before applying a subsequent pump-probe pulse pair. They later modified their instrument by placing a 50:50 beam splitter between the echelons and the focusing lens. The transmitted beam was focused onto the sample and acted as the probe. After the sample it was imaged onto one half of a CCD detector. The reflected beam was used as a reference beam to account for shot-to-shot fluctuations in the probe. It bypassed the sample and was imaged onto the other half of the same CCD detector. The group velocity dispersion of transmissive echelons is a significant consideration when working with femtosecond laser pulses. Dispersion is dependent on the thickness and wavelength dependent index of refraction of the transmissive optic. Pulse temporal stretching caused by transmissive optics can be compensated using standard pulse compression techniques, but compression of the pulses emerging from a transmissive echelon is more difficult as each portion of the probe beam has a different pathlength through the optic. The impact of dispersion on instrument response time may be minimal if the probe spectrum is relatively narrow. Shin and coworkers discussed the effect of temporal dispersion caused by fused silica echelons and found that with pulse-width limited 800 nm, 70-fs pulses, the instrument response time was approximately 100 fs.[18]

Shin et al. used their single-shot technique to measure the photolysis of triiodide ions to a diiodide anion and iodine atom within the crystalline lattice of three different organic molecules.[19] Until this point the ability to measure photochemical processes like photolysis using TA had been limited to liquid or gaseous samples where fresh sample could be supplied for each shot by flowing the sample through the measurement region. Measuring irreversible reactions in crystalline sample requires a single-shot technique. Using their transmissive-echelon-based SSTA instrument with a narrow-band probe, they identified spectral regions that were ascribed to each iodine species and performed single-shot measurements on fresh sample regions for different probe wavelengths. They were able to observe the decay of the broad absorption spectrum representing triiodide ions and the formation of diiodide and iodine fragments within 400 fs after exposure to a single UV pump pulse, allowing them to determine the rate of photolysis in each material. In 2018, they modified their instrument to perform single-shot transient reflectance spectroscopy to report on the dynamics and mechanism of the photo-induced phase transition of crystalline bismuth.[20] Previous experiments using time-resolved pump-probe measurements found evidence of this phase transition in crystalline bismuth after photoexcitation but were unable to reach any conclusions due to sample degradation. The use of SSTA enabled the acquisition of transient reflectance signal at high powers before degradation could occur.

Katayama and coworkers were the first to report wavelength resolved single-shot measurements using a reflective echelon where they characterized laser pulse durations from 150 fs to 6 ps.[21,22] In this technique they generated white light using a calcium fluoride crystal before reflecting the beam off an echelon. After the sample, the beam was

focused using a cylindrical lens onto the slit of a spectrometer where it was spectrally dispersed onto a CCD camera. The spatial time delay was imaged along the slit axis, perpendicular to the spectral dispersion axis of the spectrometer, yielding a 20 ps time delay range and spectral range of 420-630 nm.[23] This instrument was used to report on an ultrafast transition from a crystalline phase to an amorphous phase of a chalcogenide alloy, $Ge_2Sb_2Te_5$, which could be used as a rewritable material for optical data storage devices.[24] Since the transition from a crystalline phase to an amorphous phase is an irreversible event, conventional TA measurements are incapable of monitoring this transition. They were able to monitor the absorption change caused by the incident pump pulse and identify a rise time of 130-200 fs which they associated with the formation of a phonon frequency mode characteristic of amorphous $GeTe_6$. With this information they were able to propose a rearrangement of Ge atoms that would cause the phase transition. Additionally, they were able to show using their single-shot technique that the transition from crystalline to amorphous was unstable and reverted to the crystalline phase when the pump fluence was below a particular threshold.

Time Delay Encoding via Pulse stretching

The pump-probe time delay can also be encoded by stretching out the temporal duration of the probe pulse before interacting with the sample. This can be accomplished by supercontinuum generation or inducing temporal chirp in a dispersive medium such as an optical fiber or pulse stretcher, Fig. 1.5. This generates chirp in the probe pulse and encodes the time delay along the beam's spectral profile. After passing through the sample, the probe pulse can be imaged through a spectrograph onto a detector. This technique was first demonstrated by stretching a probe pulse and encoding a 15-ps time

delay range into a spectral range of 605-625 nm.[25] A grating stretcher has also been used to chirp an 800 nm probe pulse to encode a 160 ps in the spectral profile from 780 nm to 820 nm.[26] The probe pulse can also be stretched after a sample to simplify and accelerate the data acquisition process.[27] After stretching the probe pulse before a sample to spectrally encode a 4-ps pump-probe time delay, Kobayashi et al. further stretched the probe after the sample in a 3 km optical fiber into the ns regime, enabling the time delay to be recorded with low noise by a fast photodiode rather than a spectrometer. One of the primary challenges presented using beam stretching techniques is that each time delay is collected at a different spectral frequency. This is not a significant issue if the spectral feature in the TA signal is significantly broader than the probe bandwidth, but this technique is incapable of acquiring accurate dynamics when the probed TA feature is narrower than the bandwidth of the probe. The stretched probe pulse can also cause unintended transient sample changes. Artifacts owing to photoinduced changes in the refraction of the sample caused by the stretched probe pulse have been reported near time zero that persist for 10 ps,[26] which can mask the TA signal at short time delays, potentially limiting the utility of the pulse stretching strategy in some systems.

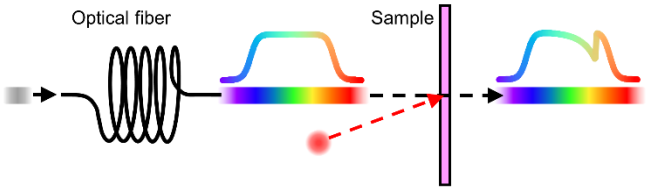

Fig. 1.5. Spectral time delay encoding. An ultrafast probe pulse (grey) is temporally chirped by an optical fiber to create a stretched probe pulse (rainbow). A pump pulse (red) is overlapped with the probe on the sample (pink). Time delay is encoded spectrally into the stretched probe pulse.

SSTA Instrumental Design Principles

The design principles discussed in this section may be pertinent to each of the SSTA techniques previously discussed. This section describes the techniques employed to calibrate the pump-probe time delay and is applicable to each technique. Uniform excitation by the pump beam is most important for angled beam SSTA, while uniform intensity in the probe beam is beneficial when using both angled beam and echelon implementations. These are each discussed in the next two sections. White light generation and the use of a broadband probe has been employed in each of the techniques and is discussed in the following section. Afterward, detection and dynamic background signals are discussed. The effect of heterogeneous samples on a spatially encoded signal is discussed in the final section, which primarily impacts angled-beam SSTA instruments. Particular emphasis will be given to the challenges and solutions inherent to the angled beam SSTA technique and instrumentation.

Time Delay Calibration of Single-Shot Transient Absorption Techniques

In typical TA measurements, the pump-probe time delay is generated by varying the pathlength in one of the two beams, usually using a retroreflector mounted on a translation stage in one arm of an interferometer. “Time zero” is the time delay where the pump and probe are temporally and spatially overlapped in the sample and is typically found by adjusting the stage position to find a sudden rise in signal intensity. Often signal from SHG in a non-linear crystal or the optical Kerr effect (OKE) in a transparent medium are used to find time zero. SHG or OKE signal arises only when the pump and probe are temporally overlapped and can be used to determine the duration of the pump and probe pulses. Time zero can also be identified by finding the sudden rise in signal for

a sample resonant with the pump, but pulse durations are more difficult to determine in this way. All other time delays are associated with positions on the translation stage using the position of time zero and the speed of light. Measurements are collected over a range of stage positions around time zero to measure a range of time delays and capture the excited state dynamics of the sample.

In single-shot transient absorption instruments the spatially or spectrally encoded pump-probe time delay no longer requires a change in the pathlength using a translation stage during measurements. Instead, the role of a variable delay stage in an SSTA setup is to calibrate the encoded time delay. Several groups have used measurements at different stage positions to show time zero appearing at different spatial locations.[12,14,15,21,26,28] The spatial time delay can be calibrated by correlating the translation stage position to the spatial location of the time zero signal. Common OKE media used for this purpose include solvents such as carbon disulfide [23,29] and dimethyl sulfoxide,[30] and solid plates such as quartz,[13] glass,[31] and lithium niobite.[24] Calibration with these media is advantageous because signal can be generated regardless of the pump wavelength and can be observed across the spectral range of the probe. Caution should be used when determining pulse compression in the angled beam geometry as the thickness of the sample may cause temporal smearing of the signal.[14] OKE signal can also be weak and difficult to measure since it is a non-resonant effect. We reported a time delay calibration method where a simple photoluminescent organic dye (either in film or solution) was used instead.[15] The advantage of this is that a thin film may be used, limiting temporal smearing due to sample thickness, and TA signals of photoluminescent samples are generally strong. Signal is measured as a function of the delay stage position, and the

resulting transients are convoluted with a step function. The location of the maximum of the convolution indicates the optimal overlap of the step function and signal, marking time zero. This method can be applied in both single-color and broadband measurements, however, the dye used must have signal across the spectral range of the instrument.

Uniform Excitation Along the Spatially Encoded Time Delay Axis

In typical TA measurements, the pump and probe beams are focused using spherical lenses and are spatially overlapped onto the sample. The signal measured by the probe is dependent on the excitation density caused by the pump. As long as the spatial overlap and pump intensity are consistent over the measured time delays, the transient signal will accurately reflect the excited state dynamics of the sample. In angled SSTA measurements, the pump and probe beams are focused using cylindrical lenses and are spatially overlapped onto the sample. The spatial time delay is encoded into the unfocused axis of the two beams. This means that spatial locations on the sample will be excited by different spatial locations in the pump beam profile. The pump intensity is not uniform, as demonstrated by the spatial profile of an approximately Gaussian pump profile we measured, Fig. 1.6a. At low pump fluence, this results in a single-shot transient spectrum that is the product of both the actual transient signal and the pump's spatial profile. This is demonstrated in a spatially encoded transient we collected of rhodamine 6G in water, Fig. 1.6b. The true transient is also plotted for comparison. The location of time zero is evident in the SSTA transient, but since rhodamine 6G has a long-lived excited state, the rest of the transient strongly resembles the pump profile itself. Signal from a long-lived dye can be used to divide out the excitation profile from the measured signal,[12] but this method is only suitable for instruments with a short spatial

time delay range. The gradual decay in the transient used to correct the pump profile can introduce a systematic error in the corrected single-shot transient in instruments with longer time delay ranges. Regions of the transient measured with low pump or probe intensity will also suffer from a decreased SNR, as seen in Fig. 1.6c before 5 ps and after 45 ps. Often this occurs at the edges of the spatial time delay range, which typically includes time zero, since the pump and probe pulses have lower intensity. A good SNR is particularly important near time zero to accurately determine fast dynamics. One solution to this is to significantly increase the pump intensity to achieve a good SNR ratio at the edges of the time delay range. However, TA signal only varies linearly with pump intensity at low pump fluences where non-linear effects such as exciton-exciton annihilation are negligible. Previous TA measurements of poly (3-hexylthiophene) (P3HT) thin films demonstrated that after exceeding a pump fluence threshold, exciton-exciton annihilation causes a non-linear dependence of signal intensity on pump fluence.[32,33] We use this prototypical conjugated organic polymer to illustrate the impact of non-linear effects on SSTA measurements in Fig. 1.7. The total pump intensity was set to 680 nJ to produce high signal intensity at the edges of the beam. In Fig. 1.7a, measurements were collected at two different translation stage positions 3.6 mm apart using a Gaussian pump profile such that time zero occurred at pixel 143 (green) near the edge of the pump profile and pixel 623 (red) at the peak of the pump profile. The sample is exactly the same for these two measurements, but it is evident that the measured dynamics near time zero appears to be dramatically different. Traditional transient absorption measurements were also performed at a range of translation stage positions, with each pixel serving as a TA detector while the translation stage position is varied.

Each pixel acquires its own transient at the pump intensity for that spatial location. If non-linear effects are present, the normalized transients measured by each pixel should manifest different dynamics. In Fig. 1.7b normalized transients from a low (pixel 143, green) and high (pixel 623, red) pump intensity region are compared with a transient collected below the pump intensity threshold to identify non-linear effects. It is evident that the transients do not agree near time zero. The sharp decay from pixel 623 at early time delays is attributed to exciton-exciton annihilation and demonstrates that non-linear effects are present when using the excitation density near the center of the beam profile. These examples demonstrate the need for a uniform pump fluence across the spatial time delay axis such that a good SNR can be achieved at the edges of the beam while avoiding non-linear effects near the center of the beam.

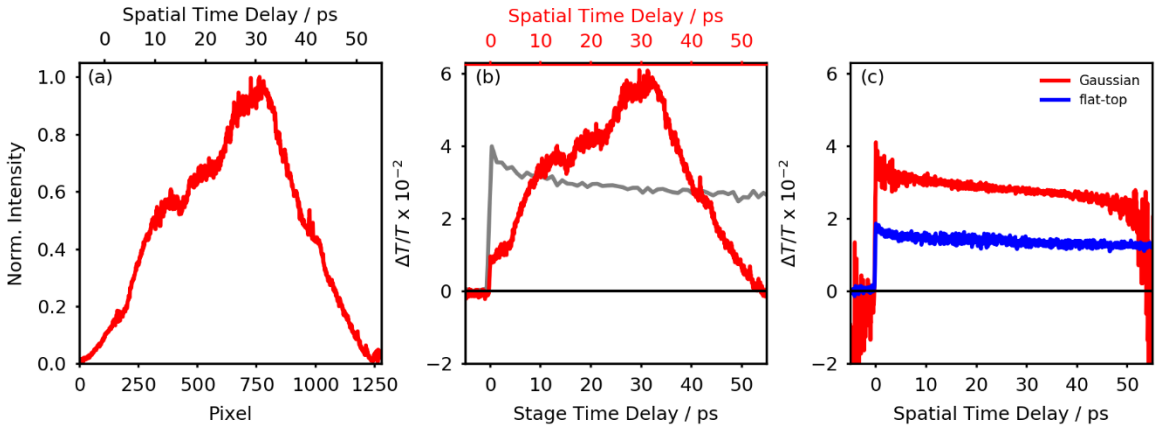

Fig. 1.6. Pump profile dependence of SSTA measurements of rhodamine 6G in water. Transient signal at 535 nm is shown in (b) and (c). Pump excitation is centered at 520 nm (a) Gaussian pump profile used in SSTA measurements. (b) SSTA measurement using the Gaussian pump profile prior to pump profile correction (red) and TA measurements using signal detected by pixel 600 (grey). (c) SSTA measurements using a Gaussian (red) and flat-top (blue) pump profile after pump profile correction.

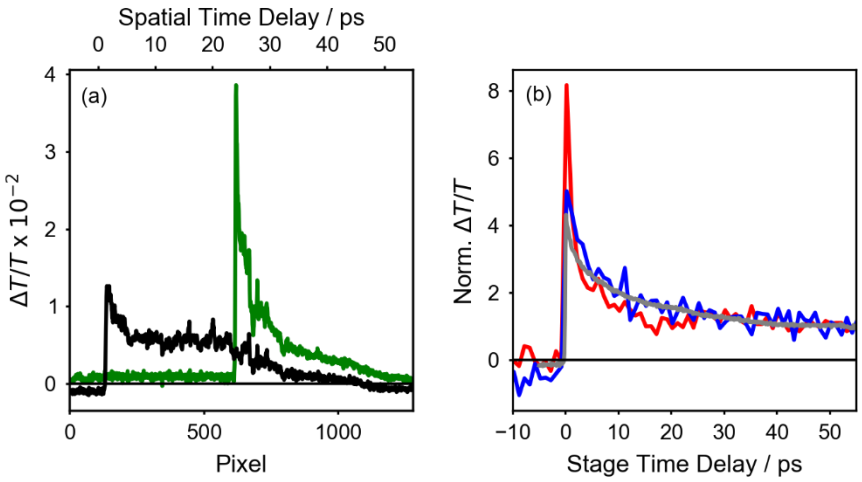

Fig. 1.7. Non-linear effects in SSTA measurements of a thin film of P3HT using a Gaussian pump profile. (a) SSTA transients at 570 nm without pump profile correction for a non-uniform pump profile at two translation stage positions 3.6 mm apart such that time zero occurs at a low (pixel 143, black) and high (pixel 623, green) pump intensity location. (b) TA transients measured using pixel 143 (blue) and 623 (red) over a range of stage positions are compared with a transient signal with no non-linear effects (grey). All transients are normalized by the average signal from 50-55 ps.

Achieving a spatially uniform pump beam and developing an accurate correction technique can both pose a significant challenge. Malley's work using a perpendicular pump-probe geometry enabled the pump to excite each time delay with approximately the same spatial profile but this strategy fails with higher optical density samples.[9] A common strategy has been to defocus the pump beam significantly to only use the flatter central region of the beam profile and correct for minor deviations using the measured pump profile. Makishima and coworkers used this approach while studying the excited state dynamics of β-carotene during degradation using SSTA,[34] enlarging their pump beam and clipping the edges to yield a nearly flat-top pump profile. This method is suitable for short spatially encoded time delays. However, for longer time delays expanding the pump profile the extent needed to yield a flat profile results in low energy densities that produce noisy SSTA measurements.

The pump profile must also be measured to correct for minor intensity deviations. Makishima et al. determined the pump profile by dispersing a photosensitive material into a polymer film which they exposed to the pump beam for a short time.[34] The amount of photodegradation at each spatial location was dependent on the exposure time and pump intensity at that location. By measuring changes in the absorption spectrum, they were able to determine the pump profile. This method relies heavily on the availability of a sample that is resonant with the pump and photodegrades in a well-characterized manner. For broadband measurements, both correction techniques assume the overlap of the pump with each wavelength in the probe is the same, but there may be a spectral dependence of the pump-probe overlap if one or both of the beams exhibit spatial chirp.

The challenge of non-uniform excitation for longer time delays can also be successfully addressed with the two-pronged approach of beam profile flattening and characterization. A spatial light modulator (SLM) can perform geometric beam shaping to transform a Gaussian profile into a flat-top profile without wasting pump intensity, as is the case in the defocusing solution described above.[14,35,36] Geometric beam shaping allows the beam profile to be completely redistributed to a new profile with minimal intensity loss.

Even with an SLM, the beam profile will not be a perfect flat-top and the small deviations in excitation density across the spatial time delay range must be corrected by characterizing the pump profile. We recently reported a similar technique to Dhar and coworkers using the transient signal from a sample.[15] Our method enables us to use any resonant sample to characterize the pump profile, even if it doesn't have long-lived, nearly constant decay across the time delay range. Traditional transients are first

measured with every pixel by performing SSTA measurements at a range of translation stage positions. These transients are compared to ensure that no sample regions are in the non-linear excitation regime, and then used to calculate an average transient spectrum of the sample that is independent of the pump intensity at any particular spatial location. The transient measured at each pixel is then divided by the average transient. This factors out the decay dynamics to yield the relative pump intensity for that pixel. The pump profile obtained from the pump intensity at each pixel can be used to correct SSTA measurements using a non-uniform pump excitation.

This correction method can be used for both single-color and broadband SSTA measurements and can correct for spatial chirp in the pump and probe. Spatial chirp in either beam can occur during generation of the beams, during transmission through optics, and can be induced by the SLM. This spatial chirp, along with wavelength-dependent optical focal lengths, causes the pump and probe profiles at the sample plane to exhibit spatial chirp. The correction method discussed above yields a different pump profile for each probe wavelength, which corrects for spatial chirp in the instrument.

The impact of combining beam shaping and pump profile correction is demonstrated in Fig. 1.6c (blue), where the noise is uniform and low across the entire spatially encoded time delay and the transient accurately represents the excited state dynamics of the measured dye. As noted above, this correction technique is only valid with low pump intensity where non-linear effects such as exciton-exciton annihilation are negligible. For broadband measurements, the calibration sample must have appreciable signal across the measured spectral range. Current work is being done in our lab to

demonstrate that measurements from multiple dyes can be combined to determine the pump profile across the spectral range.

Uniform Probe Along the Spatially Encoded Time Delay Axis

TA signal is typically reported as either differential absorbance or differential normalized transmission. While this means that the signal is independent of probe intensity, low probe intensity may result in a noisier signal. In typical TA measurements, signal acquisition time is determined by the time required to achieve a sufficient SNR ratio. The use of a Gaussian probe beam, Fig. 1.8a (red), in SSTA measurements will result in high noise at the edges of the beam, Fig. 1.8b (red). As mentioned above, a sufficiently high SNR is essential near time zero to accurately report on fast excited state dynamics. A uniform probe intensity, Fig. 1.8a (blue), will result in good SNR across the spatial time delay, Fig. 1.8b (blue). For both measurements shown in Fig. 1.8b a uniform pump profile was used and a pump profile correction was applied.

Multiple approaches can be used to generate a uniform probe profile. Malley and coworkers reported using a Ronchi ruling as an optical diffuser to create a more uniform probe profile.[9] A Ronchi ruling is a transmissive or reflective surface patterned with evenly spaced bars via photolithography and can serve as a diffraction grating. With coarse rulings the different diffraction orders spatially overlap, resulting in a more uniform probe beam profile. Defocusing the probe beam can also achieve a more uniform probe profile,[17,18,21,23] but as discussed for the pump profile, a significant amount of energy is discarded which poses a challenge if a large spatially encoded time delay is desired, and particularly if a broadband probe beam is used. Probe intensity can be

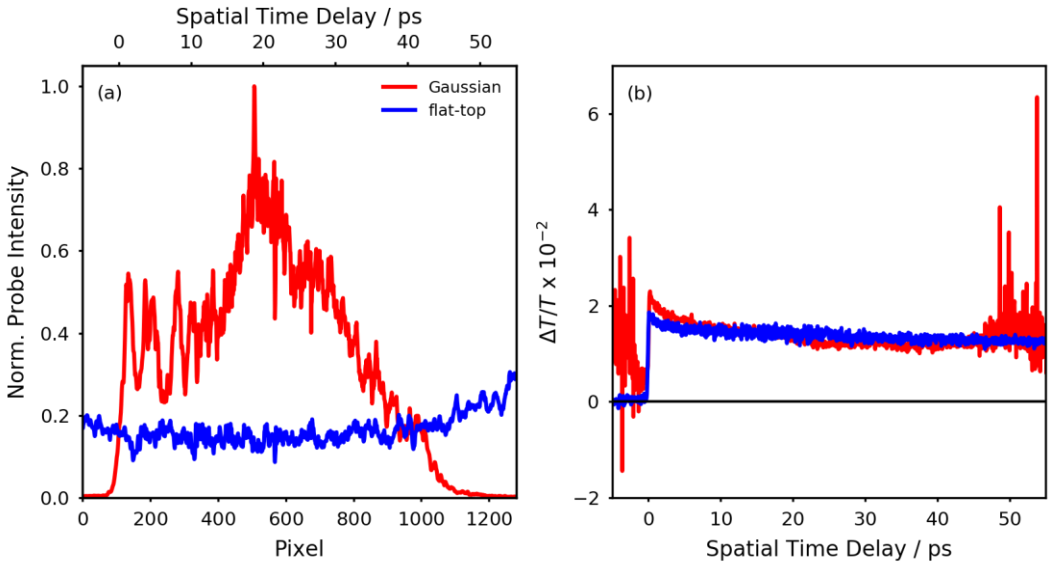

Fig. 1.8. Comparison of Gaussian and flat-top probe profiles in SSTA measurements of rhodamine 6G in water at 535 nm. (a) Probe profiles normalized by the peak Gaussian profile intensity are shown before (red) and after (blue) geometric beam reshaping. (b) 10-second SSTA measurements with a Gaussian (red) probe profile and flat-top (blue) probe profile.

conserved while flattening the probe spatial profile using geometric beam shaping, on a separate region of the SLM away from the pump beam.[15] The impact of a flat-top probe profile on the noise in a transient measured using SSTA is shown in Fig. 1.8b. The increased probe intensity at the edges of the spatially encoded time delay after beam shaping allows for a more precise measurement across the entire spatially encoded time delay.

Broadband Probe

TA measurements conducted with a spectrally broad probe provide significantly more information compared to those conducted with a "single-color" or spectrally narrow probe. In a traditional TA instrument the probe beam is focused using a spherical optic onto the sample and then directed through the entrance slit of a spectrograph and its associated array detector. In a spatially encoded SSTA instrument using tilted pulses, the probe is focused onto the sample using a cylindrical optic with time delay spatially

encoded onto the long axis of the beam. The beam is then imaged onto the slit of a spectrograph where it is dispersed onto a 2D array detector. One axis of the array detector encodes the spectral range while the other axis encodes the pump-probe time delay. Spherical aberrations caused by the imaging optics in the spectrograph affect the spectral dispersion from each location along the beam onto the detector. Calibration of the spectral axis is performed for each pump-probe time delay using either a calibration lamp with known spectral peaks or a set of narrowband notch filters across the spectral range.

Use of a broadband probe in an SSTA instrument presents an additional challenge. The size of the probe beam on the sample is orders of magnitude larger in an SSTA instrument as compared to a typical TA measurement, requiring a higher probe pulse energy than is provided by the most common methods of white light generation. Typically, a broadband probe pulse is created via white light generation (WLG) by focusing a pulsed laser into a transparent material. When the energy density of the pulse is sufficiently high, intensity-dependent components of the refractive index cause Kerr lensing and self-phase modulation, resulting in spectral broadening.[37] Sapphire and calcium fluoride are two common solid-state media used for white light generation in TA instruments. In our laboratory focusing an 800 nm 40-fs pulse with an energy of 610 nJ into a 3 mm sapphire window yielded white light from 475 to 750 nm with a pulse energy of 13 nJ, Fig. 1.9. Ferrari and coworkers reported the use of sapphire for their single-shot measurements of a 4 ps time delay range with a 120 nm spectral range, but this required an intensifier tube with single-photon sensitivity attached to their CCD detector and a time gate.[38] To avoid the experimental complexity of working with sensitive detectors and additional electronics and to enable the measurement of longer spatially encoded

pump-probe time delays, it is advantageous to increase the intensity of the broadband spectrum. However, WLG is very sensitive to input energy and focusing conditions with multi-filamentation occur if the pulse energy density exceeds a certain threshold.[39] This degrades the beam profile and can lead to spatially dependent energy fluctuations.[40] Further, high power densities are likely to burn solid state media. CaF_2, for example, is very sensitive to laser-induced damage and is typically translated during use. Liquid and gas media can also be used for WLG and can be capable of accepting higher power densities without incurring laser-induced optical damage. Furukawa et al. were the first to report a broadband SSTA setup with a time delay range of 5 ps and a spectral range from 430-620 nm.[13] They used a water cell as a WLG medium to produce probe pulses with sufficient energy. We have used a pressurized argon gas cell to a generate higher energy broadband probe pulses.[15] The spectral profile of the resulting pulses is shown in Fig. 1.9, with a total energy of 5.3 μJ generated from 800 nm, 40-fs pulses with an input energy of 580 μJ focused by a 2-m focal length mirror into a 1.6 m argon cell at a differential pressure of 0.73 bar above atmosphere. While the conversion efficiency is quite low, the input energy can be significantly higher owing to the use of a gaseous medium. Transient spectra with a 60 ps spatial time delay and a ~100 nm spectral range could be measured using this probe pulse energy.

Detection

Kodak film was used as the detector in the first reported single-shot measurements by Malley in 1969.[9] The invention of digital detectors has enhanced the sensitivity and quality of the acquired images and enabled more thorough analyses of measured signal. Modern scientific cameras generally belong to one of two structural

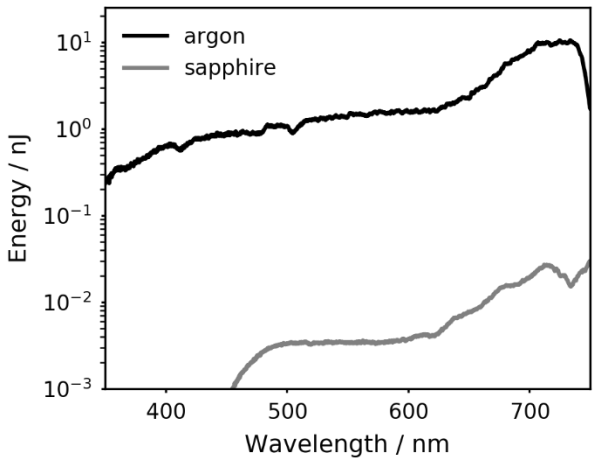

Fig. 1.9. White light generation spectrum comparison of argon (black) and sapphire (grey).

architectures. Charge-coupled device (CCD) detectors consist of an array of capacitors that become charged upon exposure to light. When the detector is read, electronic shift registers pass the charge from one capacitor to the next until it is read out by an analog-to-digital converter and transferred to a computer. A mechanical shutter is used to block the sensor during data transfer as extra light exposure will cause further charge build-up in pixels whose charge has not been collected. CCD cameras are known for high sensitivity, low electrical noise, and a large dynamic range. These features have established CCD cameras as the standard detector in many ultrafast spectroscopy labs. The second architecture is the complementary metal-oxide-semiconductor (CMOS) detector. The detector of a CMOS camera is an array of photodiodes, each with its own analog-to-digital converter. CMOS detectors do not require a mechanical shutter as the exposure is controlled digitally. CMOS cameras can acquire images at a faster rate than CCD cameras but also suffer from higher electric noise levels. Both have been employed in SSTA instruments.

Owing to the relatively slow speed of CCD detectors, many laser pulses are typically collected per image. For example, Makishima et al. used a 1 kHz laser source in their SSTA instrument, and images collected at the minimum exposure time for their CCD detector consisted of 20 laser pulses.[34] Werley et al. used a 50 ms exposure time with their CCD detected SSTA instrument.[41] While single-shot measurements actually can, in principle, encode a transient into a single pulse pair imaged onto the detector, the number of laser shots in a single measurement may still be limited by the slow data transfer rate of CCD detectors. To avoid measuring multiple pairs of laser shots, Dhar and Shin both down converted their laser repetition rate from 1 kHz to 20 and 10 Hz, respectively, to ensure that each image only consisted of one pulse-pair per image.[12,18] Slow data transfer rates continue to be a challenge for high-speed measurements with CCD detectors.

Despite the extra electric noise present in CMOS detectors, the ability to capture images at a higher rate makes them highly appealing. Many current CMOS detectors maximize the data transfer rate by splitting the detector into two halves, each with its own data transfer channel. Even with the higher data transfer rate available for CMOS detectors, a trade-off may need to be made between wavelength range and the number of laser shots per image. Using the 1 kHz laser and CMOS detector in our laboratory the image acquisition speed is rapid enough to measure only two shots per image with a 100 nm wavelength range.[15] Werley et al. analyzed the trade-off between a CCD detector with low electronic noise but slow data transfer rate and a CMOS detector with higher electronic noise but a faster data transfer rate.[41] They found that noise due to beam pointing and energy fluctuations were particularly noticeable when using CCD detector.

This was significantly reduced when using the CMOS detector to average fewer laser shots in one image, as these fluctuations are not as significant on a shot-to-shot basis. They concluded that the use of a CMOS detector in their instrument, despite the increased shot-to-shot noise, resulted in lower noise after averaging compared to the CCD detector. They did, however, identify that at very low light conditions, such as at low probe fluence, the total noise in the CMOS detector was larger than for the CCD detector. These are important considerations when choosing a detector for an SSTA instrument.

Contributions of Dynamic Background Signals

Pump-induced photoluminescence and pump scatter are additional challenges that must be considered in SSTA measurements. Each contributes to a shift in the baseline of the TA signal. In a typical TA measurement these background signals are constant across all of the measured time delays, so they can easily be corrected by subtracting the baseline signal before time zero from the entire transient. When the time delay is spatially encoded, each spatial time delay position has its own baseline. This is a significant concern when using SSTA to perform in situ TA measurements on samples undergoing an irreversible change as the scatter and photoluminescence may also evolve. Reported echelon and angled beam SSTA instruments have used a notch or bandpass filter to either block the spectral region of the pump beam or selectively permit only the spectral region of the probe into the detector.[13,17,21] This limits the spectral range that the probe can measure, and also may not work for photoluminescent samples as the spectral range of photoluminescence is often redshifted from the excitation wavelength and may be in the wavelength region of interest. Time-gating electronics can be used to block detection at

times where emission would dominate,[38] but this does not block pump scatter. A secondary chopper can be introduced to the probe line to eliminate these background contributions.[42] In typical TA and SSTA measurements, the probe beam intensity is measured with the pump beam unblocked, T_1, and blocked, T_0. The normalized differential transmission is calculated as $\Delta T/T = (T_1 - T_0) / T_0$. With an optical chopper in the probe beam, four different images are acquired, T_{11}, T_{01}, T_{10}, and T_{00}. The first (second) subscript indicates if the pump (probe) is present, 1, or not, 0, at the sample. T_{10} is subtracted from T_{11} to remove the contribution of pump scatter and photoluminescence. T_{00} is used to subtract the contribution from stray light and the electric dark signal from the detector. The scatter and photoluminescence corrected transient signal is calculated as $\Delta T/T = [(T_{11} - T_{10}) - (T_{01} - T_{00})] / (T_{01} - T_{00})$. This enables the collection of SSTA measurements where these unwanted contributions from scatter and photoluminescence caused by the pump are eliminated, even during *in situ* measurements where these contributions are expected to evolve throughout the measurement.

Spatially Heterogeneous Samples

Most of the reported SSTA measurements have been conducted on solutions, such as solvated samples, photoluminescent dyes,[12,14,29,43] β-carotene,[13,34,38] and perovskite nanocrystals during formation.[44] In each of these cases the solution ensures a uniform distribution of the sample across the spatially encoded time delay. The sample may be less spatially homogeneous in solid samples, such as in measurements of dropcast thin films of organic dyes and polymers.[6,15,42,45] While films may appear spatially homogeneous, subtle variations in optical density can result in small deviations in signal intensity that interfere with accurate SSTA measurements. This can be addressed by

translating samples through the measurement region, effectively averaging over the spatial heterogeneity in the sample. This becomes more complicated when different spatial locations in the sample actually have different excited state dynamics and not just small changes in signal intensity. We observed this in thin films of 6,13-bis(triisopropylsilylethynyl) pentacene where the transient signal measured in the crystalline domains is dependent on the orientation of the domain relative to the polarization of the incident beams. Current studies in our laboratory are aimed at determining the limits of heterogeneity that can be accurately measured using this type of SSTA instrument.

Conclusion and Perspective

SSTA is a powerful technique that can measure the photoinduced dynamics of unstable systems and irreversible photoinduced processes. Broadband transients can be obtained in as little as a pair of laser shots, depending on the sample and the choices made in the design of the instrument. However, the design and calibration of these instruments is significantly more complicated than a typical TA instrument. The achievable time delay range is dependent on the beam sizes, intensity, and incident angles onto the sample; the imaging optics; and the detector size rather than the translation range of a retroreflector. An optimal instrumental design balances the time delay range with resolution as time delay resolution may be affected by the sample thickness and incident angles of the beams. Care must be taken to calibrate the spatially encoded time delay and, if spectrally resolved, wavelength axis of the detector. Non-uniform pump or probe beams can influence the SNR at different spatial time delays and may result in non-linear processes that impede an accurate measurement of excited state dynamics. Additional

post-processing methods can be used to account for non-uniformity in the pump beam. Broadband SSTA measurements may require alternate WLG methods to achieve sufficient energy for the probe beam. Additional considerations such as dynamic pump scatter, photoluminescence, and sample heterogeneity will influence the SSTA signal but can be overcome with an optical chopper in the probe path, spatial averaging of the sample, and post-collection processing.

These design principles result in an instrument capable of measuring a wide array of systems that cannot be inspected using typical TA instrumentation, allowing for a deeper understanding of phase transitions, chemical syntheses, molecular aggregation, and light or environment induced reactions, degradation, or damage.[6,17,19,20,24,44] As the development and use of these techniques matures, questions in many realms of science can be addressed by measuring transient photoinduced spectral changes in the visible wavelength region during structural and chemical changes. In organic materials chemistry, questions regarding the impact of polymer annealing and the formation of molecular aggregates on photophysics can be probed.[46–51] The process of photodamage can be inspected in both materials and biology, such as during the denaturation of pigment-containing proteins . Rapid TA can also enable the measurement of far-from equilibrium systems. The photoinduced dynamics of these systems have never been investigated as they are often difficult to kinetically trap. For example, immature nanocrystals can be highly unstable, preventing their measurement during nanocrystal formation. Halide anions can segregate when lead-halide perovskites are photoexcited, but will re-mix when kept in the dark, making it difficult to understand this process without SSTA.[52] In this way, SSTA can be a powerful complement to existing in situ

structural characterization techniques. Further application of these design principles to different wavelength ranges (e.g. infrared) and non-linear spectroscopies (e.g. stimulated Raman spectroscopy) would broaden the scope and impact of time-resolved spectroscopy.

This dissertation will present my work developing a one-of-a-kind broadband SSTA instrument capable of measuring the excited state dynamics of evolving systems. In Chapter 2, the instrumental design principles including software development strategies will be presented. This chapter includes published co-authored material from Ashley N. Mapile, Madelyn N. Scott, and Cathy Y. Wong. Chapter 3 describes the novel techniques used to calibrate the spatial time delay and spectral axes of SSTA measurements. This chapter includes published co-authored material from Ashley N. Mapile and Cathy Y. Wong. Chapter 4 presents SSTA measurements of organic and hybrid organic-inorganic systems to demonstrate the capabilities of SSTA to measure excited state dynamics during thin film formation and nanocrystal growth. It also includes preliminary work for organic systems that will be studied in the future. This chapter includes published co-authored material from James S. Sadighian, Michael L. Crawford, and Cathy Y. Wong. It also includes unpublished work performed with Grant S. Hall, and Marc J. Foster.

CHAPTER II

INSTRUMENTAL DESIGN OF A SINGLE-SHOT TRANSIENT ABSORPTION SPECTROMETER

Includes co-authored material from:

> Wilson, K. S.; Mapile, A. N.; Wong, C. Y.; Wong, C. Y.; Wong, C. Y. Broadband Single-Shot Transient Absorption Spectroscopy. *Opt. Express, OE* **2020**, *28* (8), 11339–11355.
>
> Wilson, K. S.; Wong, C. Y. Single-Shot Transient Absorption Spectroscopy with a 45 Ps Pump-Probe Time Delay Range. *Opt. Lett., OL* **2018**, *43* (3), 371–374.
>
> Wilson, K. S.; Scott, M. N.; Wong, C. Y. Excited State Dynamics of Organic Semiconductors Measured with Shot-to-Shot Correction of Scatter and Photoluminescence. *Synthetic Metals* **2019**, *250*, 115–120.

Introduction and Instrumental Overview

Transient measurements are collected using a homebuilt broadband SSTA instrument shown in Fig. 2.1. The instrument employs the angled beam geometry discussed in Chapter 1 to encode the pump-probe time delay in the profile of the probe beam. A 1 kHz Ti:sapphire laser (Coherent) at 800 nm is split into two beam paths. One path pumps an optical parametric amplifier which generates pump pulses that can be tuned within the visible and IR spectrum. A prism compressor compensates for temporal dispersion yielding a pulse duration of ~40 fs at the sample. A neutral density filter adjusts the power of the pump pulse. A half-wave plate and polarizer optimize the polarization for use with an SLM (Meadowlark, 1920 × 1152 XY Phase Series SLM). A broadband probe pulse is generated in argon. Argon is used instead of other common solid-state media for WLG, such as sapphire or calcium fluoride, because it is capable of generating higher pulse energies needed for SSTA measurements while maintaining a sufficiently broad spectrum with reasonable stability.[53] 800 nm pulses are focused

approximately two-thirds of the way into a 1.6 m homebuilt argon gas cell using a concave mirror with a 2 m focal length. The cell, which is capped at each end by a 0.5 mm thick sapphire window, is evacuated with a vacuum pump and filled with high purity argon to a differential pressure of 0.95 bar. An iris attenuates the beam before entering the gas cell to optimize WLG. The probe path length is controlled via a retroreflector mounted onto a translation stage (Newport). This is not moved during SSTA measurements but is used to calibrate the spatial time delay, discussed in Chapter 3. The pump and probe beams are modulated using optical choppers with chopping frequencies of 250 and 125 Hz, respectively. After resizing each beam, the SLM reshapes both beams to a flat-top intensity profile, further discussed below. A cylindrical mirror limits spectral dispersion caused by the SLM in the probe beam. Cylindrical lenses focus both beams into a 22 mm line at the sample with a spatially encoded time delay caused by the 55° angle between them. The probe beam at the sample is imaged onto the 20 μm entrance slit of a grating spectrograph (Princeton Instruments, IsoPlane 160) coupled to a CMOS camera (Andor, Zyla 5.5, 2160 × 2560 pixels). To increase the data acquisition speed from the detector array during SSTA measurements, the area of interest of the camera is set to 180 × 2560 pixels. The camera exposure time is set to 1.3 ms and is triggered such that, during each exposure, two probe pulses hit the detector. One axis (2560 pixels) of the images acquired by the camera captures the spatially encoded time delay between the pump and probe beams, and the other axis (180 pixels) is spectrally resolved. Transient transmission, $\Delta T/T$, is calculated using four consecutively collected images from the camera. The camera is synchronized with the two choppers to yield images using the four possible exposure combinations by the pump and probe pulses, T_{11}, T_{10}, T_{01}, and T_{00},

where the first and second subscripts indicate the presence (1) or absence (0) of the pump and probe, respectively. Ambient background light (T_{00}) and signal arising from pump scatter and pump-induced photoluminescence of the sample (T_{10}) can be subtracted using this combination of images.[42] Each transient image represents a broadband transient spectrum with a time delay range of 60 ps and spectral range of 100 nm.

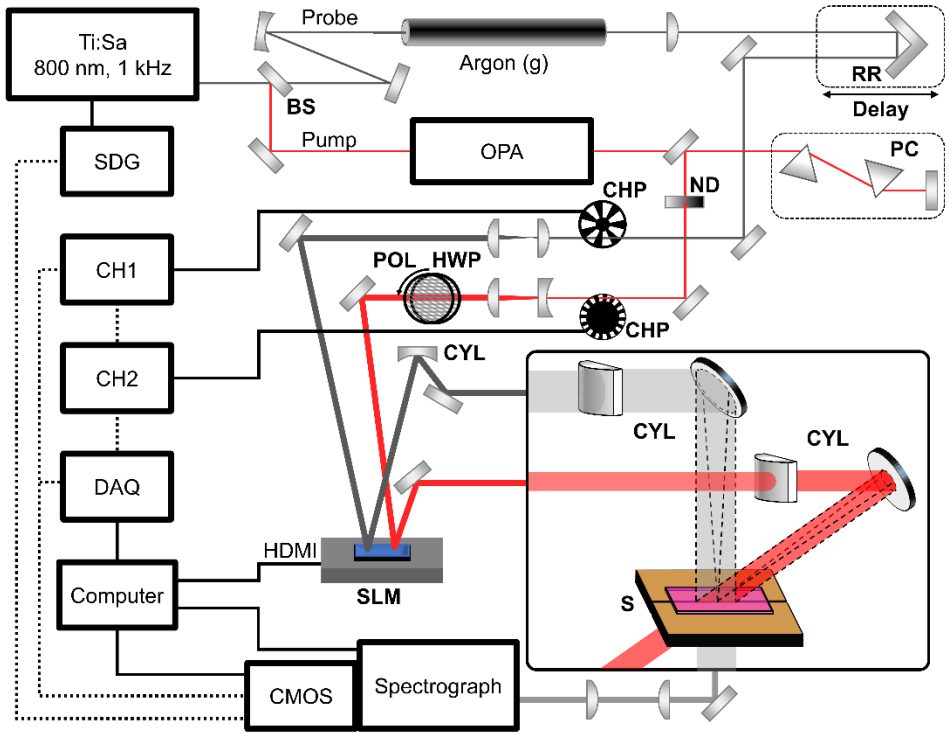

Fig. 2.1. Schematic of SSTA instrument. Argon (g), pressurized argon cell; BS, beam splitter; CH#, optical chopper controller; CHP, optical chopper; CMOS, camera; CYL, cylindrical lens or mirror; DAQ, data acquisition card; HWP, half-wave plate; ND, neutral density filter; OPA, optical parametric amplifier; PC, prism compressor; POL, polarizer; RR, retroreflector; SDG, synchronization and delay generation; SLM, spatial light modulator.

For each sample, the 100-nm spectral range acquired by the array detector is set via the spectrograph software. Calibration of the spectral axis of the image is discussed in Chapter 3. The pump and probe beams are reshaped to a flat-top profile and overlapped as described below. The probe energy was set to 10 nJ. The pump energy was set to 1.1 μJ, 730 nJ, and 400 nJ for cresyl violet, pseudoisocyanine (PIC), and P3HT

measurements, respectively. The pump fluence for each sample was in the linear regime. Measurements of P3HT were acquired while translating the film at a speed of 0.3 mm/s with a motorized linear actuator to average over any heterogeneity in the film. SSTA measurements are acquired at a range of translation stage positions corresponding to 120 ps of time delay typically with a step size of 1 ps. The spatially encoded time delay is calibrated, as described in Chapter 2. A correction for non-uniformity in the pump profile is performed following the procedures described in Chapter 3. Spectral calibration is only performed when the wavelength range of the spectrograph is adjusted. The remaining calibration procedures are performed once for each sample.

Instrument Communication and Triggering

The laser, CMOS detector, optical choppers, and computer all interface together to synchronize each instrument during data collection. The transistor-transistor logic diagram is shown in Fig. 2.2. A synchronization and delay generator (SDG) triggers the 1 kHz Ti:Sa laser. Another signal from the SDG triggers the CMOS detector at the same frequency. After a trigger, the CMOS detector acquires an image using a digital global shutter for the set exposure time. At the end of the exposure, the built-up charge is transferred to the readout node. The detector transfers the data from the readout nodes to the computer and waits for the next trigger from the SDG to begin the next exposure. In overlap mode the readout can occur during the exposure time of the next image. During exposure the camera does not accept a trigger from the SDG. Exposure time controls the number of shots acquired per image. The camera exposure time must be set for less than the time interval between neighboring shots to ensure that a trigger signal is not missed (e.g. 0.5 ms for 1 kHz image acquisition rate, 1.5 ms for 500 Hz image acquisition rate).

The detector outputs a trigger signal at the image acquisition rate. This triggers the probe optical chopper (Thorlabs) and a DAQ device (National Instruments). Any easy method to check if the camera is not missing a trigger from the SDG is to compare the input frequency detected by the optical chopper controller to the expected frequency dictated by the exposure time.

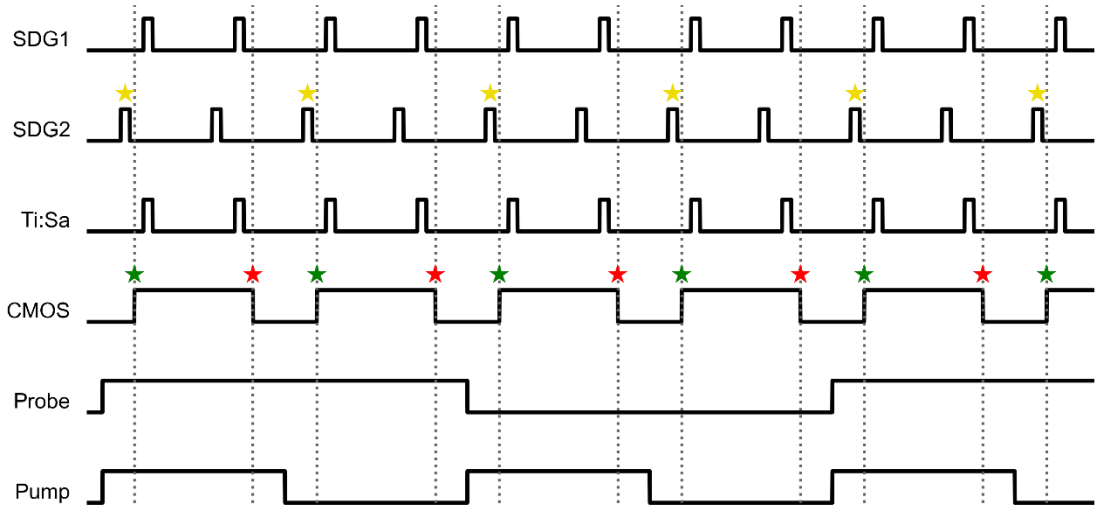

Fig. 2.2. SSTA instrument trigger schematic. SDG1 triggers the laser (Ti:Sa) and SDG2 triggers the detector (CMOS). Only triggers received by the CMOS detector while not acquiring an image are detected (yellow). The beginning (green) and end (red) of the exposure are marked by vertical lines. The probe and pump choppers block (low) and unblock (high) probe and pump pulse, respectively.

The probe optical chopper modulates the probe beam with a 1:4 ratio to the image acquisition rate such that two consecutive images are collected with the probe unblocked followed by two images with the probe blocked. The state of the probe optical chopper (blocked or unblocked) is detected by the software using the acquired probe intensity for each image. The probe optical chopper triggers the pump optical chopper with a 2:1 ratio such that acquired images alternate between the pump blocked and unblocked. The state of the pump chopper is detected by the digital input channel of a DAQ device that was

triggered from the image acquisition rate. The software detects a rising or falling signal in the pump output channel and assigns the pump chopper state to each acquired image.

Software Communication and Architecture

The software used to control the SSTA program was designed using Python 3 and the Qt widget toolkit. The program controls the CMOS detector, translation stage, data acquisition (DAQ) hardware. It also processes the incoming images to calculate a $\Delta T/T$ signal and saves them to four internal solid-state hard drives configured in a RAID 0 implementation. This configuration enables high speed data storage by splitting the data into chunks and writing each chunk to a separate hard drive, taking advantage of the maximum write speed of all four drives simultaneously. The software also includes plug-in options to include other custom instrumentation and software. This section describes the design principles built into the program to operate the equipment and collect data.

This program operates using parallel processing. This enables a smooth interface while both collecting and processing data. It is well known that Python uses a global interpreter lock (GIL) that limits a Python process to a single thread on the computer processor. This limits a program from multitasking, which is essential during SSTA data collection. Multiprocessing overcomes the limitation caused by the GIL and allows a parent process to create child Python processes, each with their own independent thread. Shared variables allow the processes to communicate while performing their own tasks independently. The SSTA parent process initiates the creation of the graphical user interface and orchestrates the transfer of user input variables and actions to the child processes. At startup, the parent process initiates a child process for each major component of the data collection process: CMOS detector, DAQ, translation stage,

calculations. To satisfy the demands of the data processing performed in the calculations process, four identical processes are created and share the analysis and saving tasks.

Each process has the same basic structure. During initiation the shared variables necessary for the child process to operate are passed into the new child process. After initiation, the process enters a loop that runs while the application is open. Event flags from the parent process describe which function from the child process should be run. At the close of the application, the child process receives the call to close from the parent process.

CMOS Process

Communication with the Andor Zyla 5.5 scientific CMOS detector is performed using a homebuilt Python wrapper around the c-based Andor 3 software development kit. In the wrapper code the library is imported into Python and c-type variables are paired with Python functions. The code transforms the c-based code into a class structure. In the SSTA CMOS detector child class, the camera is connected and default variables are set. The camera is operated with a 16-bit data encoding structure. A shared array from the parent process is used as the image buffer and can hold up to 500 16-bit images of a 1000 × 2560 dimension. The cycle mode is set to continuous where the detector will continuously acquire images until a stop acquisition flag is set. A digital global shutter is used which is typical for imaging pulsed light sources. The CMOS detector has built-in sensor cooling that keeps the detector at 1.7 °C. Internal processing in the detector includes a spurious noise filter and static blemish correction. The detector is set to overlap mode wherein image data is transferred to the computer as a new image is being collected. The user can select between a software trigger and an external trigger.

Software triggers can be sent using the Andor library. External triggers are received using an input BNC cable into the detector. The DAQ or another square waveform generator can be connected for testing purposes if necessary. During SSTA data collection the trigger mode is set to external where signal from the SDG triggers the detector.

During image acquisition buffer addresses for 500 images are added into a queue. The software writes incoming data from the detector to the first buffer address in the queue. The buffer address is then placed at the end of the buffer queue. To retain the data stored in the buffer, the software must copy the data from the buffer address before it is rewritten when it reaches the front of the queue again. Image acquisition can be acquired in two modes. Beam overlap and alignment mode is a basic acquisition mode where images can be acquired in either software or external trigger mode. The software mode is necessary for troubleshooting or general work when the laser is not on and sending triggers. During SSTA data collection a timer is created. The camera begins acquiring images at the trigger rate from the SDG. The detector acquires images during a pre-scan time (usually 40 s). This gives time for the optical chopper controllers to detect the outgoing trigger from the detector and the choppers to accelerate to the correct chopping frequency and phase. After the 40 s timer is concluded the calculation flag is set and the number of acquired images is tracked. Once the number of acquired images reaches the number dictated by the user for a particular translation stage position, the process sets the flag that indicates the need to move to a new translation stage position and the calculation flag is cleared. The camera continues to acquire images but will not set the calculation flag until it receives a signal that the stage is finished moving. When the run end signal is

raised, the image acquisition loop finishes, and the camera moves to idle mode. At close, the sensor cooling is disabled, and the camera is disconnected from the software.

DAQ Process

Communication with the NI DAQ uses an open-source Python wrapper to the NIDAQmx ANSI C library.[54] A shared array from the parent process is used as a buffer to store the pump chopper state. It has a buffer input of 500, matching the image buffer size. A digital channel connected to the output stage of the pump chopper controller detects the state of the pump chopper. A second channel is connected to the output trigger from the CMOS detector. The DAQ is triggered by the falling edge of the camera trigger. After the trigger, 15 data points are collected for a duration of half of the exposure time. During this time the measured input from the chopper will either have a rising edge (pump present) or a falling edge (pump blocked). During data acquisition the state of the pump is collected when the calculation flag is set at the same rate as images are acquired in the CMOS child process.

Translation Stage Process

The Newport translation stage is controlled by a motion controller (Newport, XPS-Q8). Python code provided with the controller is used to interface with the stage. Using the IP address of the motion controller on the local network, a transmission control protocol connection is established. The stage group number and translation range are input by the user. During initialization the stage position is reset before use. Unlike the other processes that are only operable during image acquisition, this process can receive commands from the user at any point after initiation. The process enters a loop and waits

for signals from the parent process. The translation stage position is calibrated to pump-probe time delay in picoseconds by

$$t = 2\,(p - p_0) / c \tag{2.1}$$

where p is the position of the stage (in millimieters), p_0 is the position of the stage (in millimeters) at a pump-probe time delay of 0 ps, and c is the speed of light (in millimeters per picosecond). The factor of 2 accounts for the in-and-out pathlength change in the probe path. During data collection the parent process detects when the stage has finished its command and signals to the CMOS process when to begin saving data again.

Calculations Process

The four child processes used to perform SSTA calculations all share the image and pump chopper state buffers and a data queue. Input parameters from the software include the image dimensions, optical chopping conditions, and calculation parameters. The image buffer is capable of holding 500 images up to a dimensional size of 1000 × 2560. The actual image dimensions used during data collection are generally much smaller and must be extracted from the buffer. During data collection the probe optical chopper is optional and, if used, can modulate the probe at a 2:2 on/off ratio or a 3:2 on/off ratio. These settings are passed from the parent process and are taken into account during data calculations. SSTA measurements can be performed using both wavelength and spatial time delay resolution or only using spatial time delay. For single-color measurements, the intensity measured by the detector is summed along the spectral axis of the image before calculating the transient signal.

SSTA signal is calculated based on the probe chopper settings. If the probe chopper setting is disabled, then the signal is calculated with the following formula with a

subscript referring to the presence of the pump. $\Delta T/T = (T_1 - T_0) / \overline{T_0}$ where T_1 and T_0 are the transmission of the probe with and without the pump exciting the sample, respectively. Alternating images are used for these two values. $\overline{T_0}$ is the average of the probe beam within a given data set from the buffer. It has been shown previously that noise in the transmission can result in a positive offset in the ΔT/T signal.[55] By averaging the normalizing factor over several laser shots, the impact can be mitigated. When the probe chopper is in use, the state of the probe beam is determined by the measured intensity in each of the images. The intensity of a central region of the image is averaged together and compared over a set of images. Once both the pump and probe chopper states have been acquired, the array positions for each of the four chopper state images is determined and the signal is calculated. If the parent SSTA software is ready to update the live view to the image, then the calculated signal is saved into a shared array. The data is then saved to its file location.

White Light Generation Using Argon

Background

White light generation in an argon gas cell has been reported previously to give a high energy, broad spectral range from 200 nm to 1300 nm.[53,56–58] Kosma et al. reported that high partial pressures of argon, and a longer focal length into the argon cell result in more efficient WLG. Both windowed and windowless gas cells were reported in their work. At longer pulse widths (45 fs) they reported better conversion at higher pressures which required that the cell be capped at each end with an optical window. When working at higher pressures with optical windows it is necessary to consider the

maximum pressure threshold that a window can withstand when designing the gas cell. The maximum differential pressure that can be supported by a window is modeled as

$$P = \frac{t^2 \cdot M}{r^2 \cdot K \cdot SF} \tag{2.2}$$

where *t* is the thickness of the window, M is the modulus of rupture inherent to the window material, r is the unsupported radius of the window, K is an empirical constant which is typically 0.75 if the window is clamped at the edges, and SF is the safety factor and is often chosen to be 4. A thicker window can support higher pressures but also induces temporal dispersion in the beam affecting the pulse compression before and after WLG. This section describes the gas cell design and construction.

Gas Cell Design

An argon gas cell was constructed using standard fittings and is shown in Fig. 2.3. The cell uses 1/2 NPT threaded pipe fittings for the length of the tube. The window is compressed by flanges between two Viton gaskets to create an airtight seal. Four 1/2"-13 screws are tightened incrementally, alternating between oppositely positioned screws. Uneven tightening can crack the window. The gaskets must be clear of dirt or debris to create a tight seal. An outlet valve is connected to a vacuum pump (Welch, DryFast 2037) and an inlet valve is connected to an argon gas cylinder (PurityPlus, 99.999%). A pressure sensor detects the difference between ambient pressure and pressure inside of the cell. A pressure relief valve can be used to quickly evacuate the cell or serves as a safety mechanism to prevent the windows from shattering. A first design used 1.6 mm quartz windows which has a modulus of rupture of 480 bar, giving a max internal pressure of 4 bar. Quartz is more susceptible to burns at the input energy density of the 800 nm beam and was replaced with 0.5 mm sapphire windows. Although sapphire has a

much higher index of refraction, the modulus of rupture is ~4400 bar and can withstand a much higher pressure. As a result, the window thickness could be much thinner to minimize dispersion while still maintaining a max pressure of 3.5 bar. Loctite 572 thread sealant is used to seal the joints together. It is compatible with the stainless-steel fittings used in the design and has a maximum pressure threshold of 690 bar. This sealant reacts anaerobically to solidify and will only harden when the fittings are sufficiently tightened. A continuous flow of nitrogen in the cell for 72 hours will ensure that any leaked sealant from the fitting will harden within the cell.

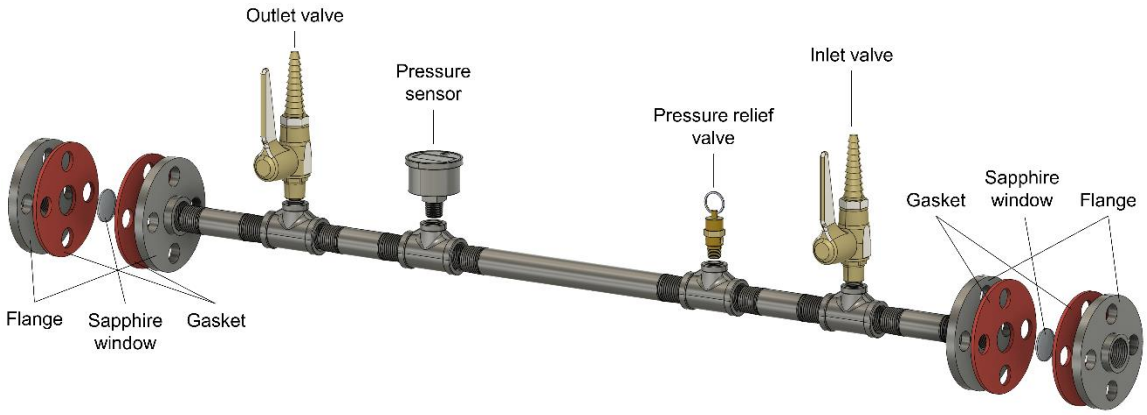

Fig. 2.3. Argon gas cell design.

Installation

A mirror with a 2 m focal length is used to focus the 800 nm beam into the gas cell. The mirror should be positioned such that the focal point is between 1/2 and 2/3 along the length of the cell. An iris is mounted before the beam inlet to attenuate the beam fluence into the cell. After the cell a lens collimates the beam, and a dichroic mirror with a reflective spectral range below 750 nm filters out the fundamental 800 nm beam.

Operation and Optimization

To pressurize the cell, both the inlet and outlet valves are opened to the vacuum pump line. After the differential pressure sensor reads below -0.9 bar, the outlet valve is

closed, and the argon regulator is opened. Efficient WLG requires a minimum differential pressure of 0.5 bar but is often operated at ~1.0 bar. Alignment procedures are described in Appendix A. After the beam is well aligned through the tube, the attenuating iris is opened until stable white light is observed. Visual inspection of the beam profile, color, and stability is sufficient for optimizing the input fluence. Optimal conversion can also be found by observing the spectral bandwidth using an Ocean Optics spectrometer or by transmitting the beam through a prism onto a piece of paper as shown in Fig. 2.4. A photoluminescence response is observed in the paper below 400 nm which is the most sensitive portion of the supercontinuum. This enables a visual view of the entire spectral range and can inform the viewer of the quality of WLG.

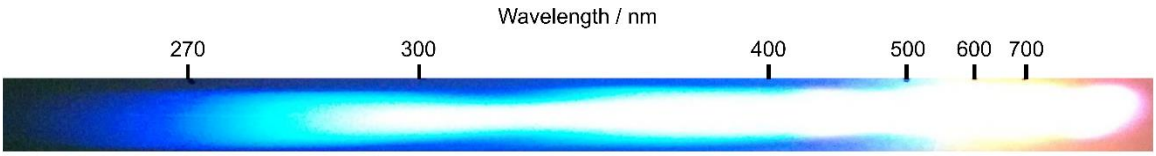

Fig. 2.4. Spectrally dispersed white light onto a piece of paper.

Geometric Beam Shaping Using a Spatial Light Modulator

Theory

The unique advance that has doubled the achievable spatially encoded time delay range in our SSTA instrument is the use of a phase-only SLM to reshape the pump and probe beam profiles. As discussed in Chapter 1, the spatial profile of the pump pulse determines the density of photogenerated species in each area of the sample that interacts with the pump. Above a certain density threshold, multi-body processes like exciton-exciton annihilation will occur, altering the observed dynamics. Spatially encoded dynamics will not be accurate if these processes occur in areas of the sample that interact with a high pump fluence, and not in other areas where the pump fluence is lower. Multi-

body processes depend non-linearly on the pump intensity and cannot be accounted for by normalization procedures. Unless the spatial profile of the pump is perfectly uniform, the dynamics of multi-body processes cannot be measured using this technique. If the photoexcitation density is below the threshold throughout the excitation volume, the same excited state dynamics should be induced at each spatial location, and any variation in pulse intensity can be accounted for by normalization. If pulse energy is lowered such that the excitation density is within the linear regime for the center of a beam with a typical Gaussian spatial profile, only a small spatial region of the profile will have enough intensity to yield signal with an adequate SNR. A uniform pump intensity at the sample facilitates a maximum excitation density across the spatial time delay range without causing many-body interactions that affect excited state dynamics.

While not directly influencing the excited state dynamics, a non-uniform probe beam impacts accurate acquisition of SSTA signal. As discussed in Chapter 1, a Gaussian probe profile will result in low probe intensity at the edges of the spatially encoded time delay. At low probe saturation on a detector, the SNR is often much lower compared to intensity that fills the dynamic range of the detector. Since the spatial location of time zero is often set at the edge of the probe beam, a Gaussian profile would result in noisier signal for time points where the dynamics is the fastest and requires high SNR to accurately analyze. A uniform spatial profile for the probe beam enables a uniform saturation level on the array detector, allowing the full dynamic range of the detector to be leveraged to increase the SNR of the measurement.

Beam Correction

A phase-only SLM can overcome this problem for both beams by using geometric beam shaping to spatially redistribute the intensity of an input beam profile, $i_1(x)$, into an output beam profile, $i_2(x)$. A geometrical distortion, $h(x)$, can redirect the intensity such that the total intensity of a particular slice of the input profile corresponds to a specific slice in the output profile with the same intensity,

$$i_1(x)\mathrm{d}x = i_2(h)\mathrm{d}h \ . \tag{2.3}$$

As shown schematically in Fig. 2.5a, i_1 can be Gaussian shaped (blue) that is partitioned into slices and redirected to form i_2, a high-order super-Gaussian with the desired even intensity profile (orange). The SLM applies this geometrical distortion by imparting additional phase to each spatial region of the beam profile,

$$\phi(x) = 2\pi \int h(x)\,\mathrm{d}x \ . \tag{2.4}$$

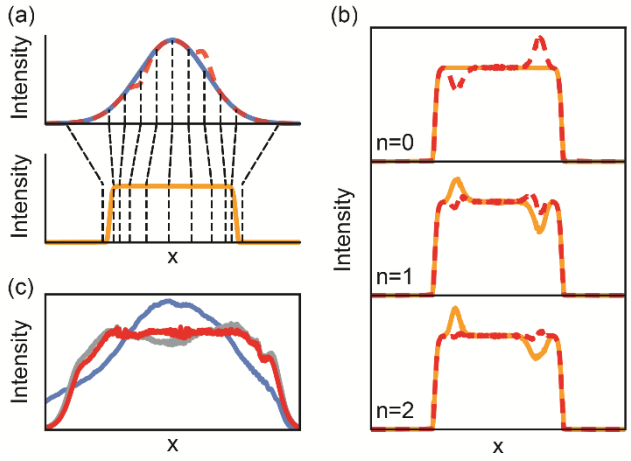

Fig. 2.5. Geometric beam shaping to achieve an even pump beam profile. (a) Theoretical Gaussian (blue) and imperfect Gaussian (red dashed) input beam profiles. Spatial distortions (black dashed) redistribute intensity to generate a target flat-top beam profile (orange). (b) Schematic of output profiles (red dashed) after n iterative corrections to the target output profile (orange) when using an imperfect Gaussian input profile. (c) Measured output profiles generated from input profile (blue), before correction (grey) and after nine iterations (red). Reprinted with permission from ref. 14 © The Optical Society.

The distortion $h(x)$ that redistributes i_1 into i_2 is obtained as follows. From Eq. (2.3), the cumulative intensities of the two profiles are related by

$$\int_{-\infty}^{x} i_1(x')\,\mathrm{d}x' = \int_{-\infty}^{h(x)} i_2(x')\,\mathrm{d}x' \tag{2.5}$$

such that the distortion can be calculated by

$$h(x) = F_2^{-1}\left[F_1(x)\right] \tag{2.6}$$

where $F_k = \int_{-\infty}^{x} i_k(x')\,\mathrm{d}x'$. While an analytical solution has been reported,[59] the actual output profile will not be a super-Gaussian if the input profile is not perfectly Gaussian, for example the dashed red curve in Fig. 2.5a.

This can be corrected by implementing a simple iterative algorithm to modify the target output profile, i_2, until the actual output profile, i_2', provides adequately even illumination at the sample position. On each iteration, the target profile is modified to

$$i_2^{(n+1)} = i_2^{(n)} + \left(i_2^{(n)} - i_2'\right) \tag{2.7}$$

where $i_2^{(n)}$ is the target profile after n iterations. The phase is calculated from h using Eq. (2.4-2.6), applied to the SLM, and the process is repeated until the measured intensity profile at the sample position is adequately even, shown schematically in Fig. 2.5b. This correction is shown for an actual beam in Fig. 2.5c. Additionally, a phase-encoded Fresnel lens is applied.[60] The pump intensity profile obtained from this process is used to excite the sample within the linear regime. A flat-top probe is also achieved using the same process.

The probe and pump beams are each incident on a different spatial region of the SLM. Each pixel of the SLM can be independently controlled to modify the phase of incident light. The imparted phase calculated using the procedures detailed above

reshapes the approximately Gaussian incident spatial profile to a flat-top profile at the sample using geometric beam shaping.[14,35]

In addition to a phase map that reshapes each beam, phase maps that emulate a prism and a lens provide further control over the incident beams.[61] The prism phase is $\phi_{prism} = a \cdot x$ where the constant a imparts linearly varying phase along a spatial coordinate, x, with $x = 0$ at the center of the SLM. This corresponds to the effect of a small-angle prism and results in a shift in the pointing of the beam. This redirects the reshaped beam away from the zeroth order reflection from the SLM, preventing this reflection from interfering with SSTA measurements. The lens phase is $\phi_{lens} = b \cdot x^2$ where the constant b changes the effective focal length of the lens. The beam focuses when $b > 0$ and defocuses when $b < 0$. The size of each beam at the sample is finely tuned by choosing two values of b to independently focus or defocus each beam.

The total phase mapped onto each beam by the SLM is simply the sum of the three phase components. Using both the prism phase and lens phase, the horizontal and vertical shift and focusing of each beam can be independently controlled. Additionally, the applied phase can be varied as a function of spatial location, resulting in variable focusing and shifting of the beam, shown below to be particularly useful for correcting undesirable focusing effects in the pump beam inherent to the experimental setup.

Non-uniform focusing of the pump

The steep incident angle of the pump beam at the sample results in non-uniform focusing at the sample position. The cylindrical lens focuses the pump to a line that is not parallel with the sample plane, Fig. 2.6a. The entire spatial profile of the pump pulse on the sample plane can be imaged by using a photoluminescent sample and opening the

entrance slit to the spectrograph such that it does not impede any part of the imaged photoluminescence, and directing the zeroth order reflection from the grating to the array detector. As shown in Fig. 2.6b (blue), the pump beam produces a bowtie-shaped area of excitation at the sample plane, resulting in a non-uniform energy density. We correct for this by using the SLM to apply a phase map that emulates a lens with a focal length that varies along the long axis of the pump beam,

$$\phi_{lens'} = \phi_{lens} + c \cdot x^3 \tag{2.8}$$

where c controls the amount of variable focusing. Different values of c are chosen for different parts of the beam to change the effective focal length of the cylindrical lens immediately before the sample to optimize the focal line at the sample plane. Additionally, small aberrations in the optics may cause the focal line to be slightly curved at the sample, making it impossible to pass uniformly through the entrance slit on the spectrograph. The focal line at the sample plane can be straightened by using the SLM to apply a variable shift using a modified prism phase,

$$\phi_{prism'} = \phi_{prism} + d \cdot x^2 \tag{2.9}$$

where d controls the amount of variable shift and is optimized for each location along the focal line.

In practice c and d are determined as follows. The pump profile is modified to consist of three peaks of equal intensity via geometric beam shaping using the SLM. With the spectrograph slit set at 20 μm (Fig. 2.6b, dashed lines), the integrated intensity of the uncorrected pump photoluminescence for the edge peaks are lower than the central peak due to the bowtie shape, shown in Fig. 2.6c (blue). Note that curvature of the imaged slit results from minor optical aberrations in the spectrograph and does not

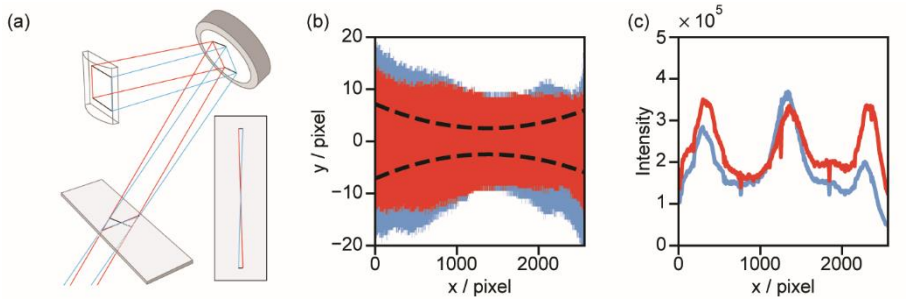

Fig. 2.6. Pump beam focus correction. (a) Pump beam focused onto the sample plane using a cylindrical lens with each side of the beam traced to its projection on the sample. Inset: Projection of pump onto sample, viewed from top. (b) Spatial profile of the pump beam on the sample plane without (blue) and with (red) focus correction. Colored pixels indicate locations where measured photoluminescence intensity, I_f, was above $\max(I_f)\cdot e^{-2}$ where $\max(I_f)$ is the maximum intensity for each column of pixels. Dashed lines mark the spectrograph entrance slit when set at 20 μm. (c) A three-peaked pump intensity profile through the 20-μm slit integrated along each column of pixels from (b) without focus correction (blue) and with focus correction (red). Reprinted with permission from ref. 15 © The Optical Society.

significantly impact results. The values of *c* and *d* are adjusted until the three peaks are of equal size, Fig. 2.6c (red). The zeroth order image of the corrected beam, shown in Fig. 2.6b (red), minimizes the bowtie shape. The three peaks are removed to yield a pump with a near-rectangular spatial profile and flat-top intensity profile at the sample plane, ideal for SSTA measurements. This correction can also be performed by viewing the spectral region of the sample photoluminescence caused by the pump and integrating across the spectral axis.

Dynamic Correction to Background Signals

Background

Normalized differential transmission is typically calculated by

$$\frac{\Delta T}{T} = \frac{T_{11} - T_{01}}{T_{01}} \tag{2.10}$$

where T_{11} is the measured intensity of the transmitted probe beam after the sample when the pump is also incident on the sample, and T_{01} is the intensity of the transmitted probe

beam without the presence of the pump. The measurements of T_{11} and T_{01} are usually conducted sequentially using an optical chopper to block alternate pump pulses. Structural features in an organic film can cause some scatter from the pump pulse to reach the detector and contribute to the T_{11} term. Photoluminescence (PL) caused by the excitation of the pump pulse will also contribute to the T_{11} term. This is usually not a significant problem when measuring systems at structural equilibrium since the intensities of scatter and PL do not change during the measurement. Further, when using typical implementations of TA without spatial encoding, the measurement at each pump-probe time delay is conducted on a single spot on the sample that yields a certain amount of scatter and PL. Thus, in measurements of samples at structural equilibrium using typical implementations of TA, contributions to the signal from scatter of the pump beam or pump-induced PL constitute a constant baseline in the signal and can simply be subtracted. Pump scatter and pump-induced PL is a more significant problem when measuring samples that are not at structural equilibrium since the amount of scatter and PL will change as the structure evolves. Further, if the pump beam is incident on a larger region of the sample, as is the case in many implementations of SSTA, any heterogeneity in the sample would result in a different amount of scatter at each location along the focal line. An evolving and heterogeneous sample in the spatial domain is a significant obstacle to the measurement of excited state dynamics during the process of film formation from solution.

In this section we report the use of an optical chopping scheme that enables the shot-to-shot correction of pump scatter and pump-induced PL. This extends the ability of the SSTA technique to the measurement of changing excited state dynamics in a variety of systems such as organic small molecules and polymers during the formation of organic

films from solution regardless of whether the amount of scatter or PL changes significantly during this process. We demonstrate this capability by measuring a highly photoluminescent solution of the organic small molecule dye sulforhodamine (SR), a film of SR, and a film of the prototypical organic semiconductor, P3HT with and without shot-to-shot PL and scatter correction. The advance presented in this work will enable the measurement of excited state dynamics during the complex non-equilibrium processes that comprise solution-based organic film formation.

Methods

Two optical chopping schemes are compared. In optical chopping scheme A, Fig. 2.7, the camera acquired images of the probe beam with the pump beam blocked (T_{01}) and unblocked (T_{11}) by using the optical chopper in the pump beam path. Further synchronization with the optical chopper in the probe beam path resulted in optical chopping scheme B which enabled the acquisition of images of pump scatter and pump-induced PL (T_{10}) and dark images with both pump and probe pulses blocked by the optical choppers (T_{00}). The optical chopper in the probe beam path had a duty cycle of 50%, with the phase set such that three pulses were transmitted followed by two pulses blocked, Fig. 2.7. This 3:2 ratio enabled acquisition of two corrected transients using each set of five laser shots, where the two transients were calculated using separate, but always temporally adjacent, measurements of T_{11} or T_{01}. This strategy optimized the fidelity of the differential measurement of T_{11} and T_{01} since adjacent laser shots are more likely to have correlated energies.[62] This ratio cannot be used when multiple pulses are acquired per image because of the 50% duty cycle of the probe optical chopper.

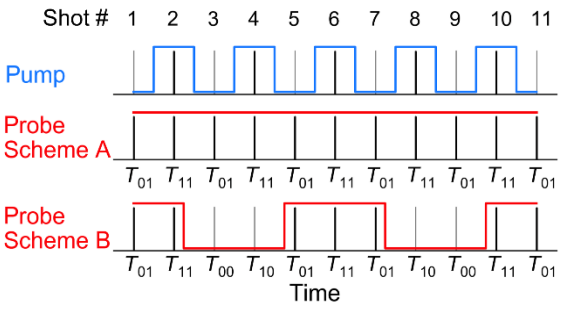

Fig. 2.7. Optical chopping scheme used for the pump (blue) and schemes used for the probe (red) without (A) and with (B) the additional optical chopper in the probe beam path. Reprinted with permission from ref. 3 © Elsevier B. V.

Discussion

Normalized differential transmission is calculated by Eq. 2.10 in a typical TA measurement using optical chopping scheme A. Optical chopping scheme B of Fig. 2.7b enables the collection of two additional pulse combinations, T_{10} and T_{00}, when only the pump pulse is incident on the sample and when neither pulse is incident on the sample, respectively. The normalized differential transmission can then be calculated by Eq. 2.11.

$$\frac{\Delta T}{T} = \frac{(T_{11} - T_{10}) - (T_{01} - T_{00})}{T_{01} - T_{00}} \tag{2.11}$$

When measured and calculated in this way, $\Delta T/T$ represents the change in transmission owing to the presence of the pump pulse, excluding any contributions from pump scatter or pump-induced PL. Note that the intensity measured when neither beam is incident on the camera, T_{00}, is the result of stray light and dark current from the camera. The signal from T_{00} is present in each of the other pulse combinations, including T_{10}. Since T_{10} is being subtracted from the T_{11} term, T_{00} must also be subtracted from the T_{01} term. The T_{00} term is included in optical chopping scheme B to enable the dynamic subtraction of this contribution. However, if T_{00} is shown not to change with time, this measurement could potentially be acquired only once, either before or after the SSTA measurement. This

would further reduce the time required to acquire enough signal to achieve an adequate SNR.

Fig. 2.8a compares $\Delta T/T$ for a SR solution calculated using Eq. 2.10 and 2.11, the equivalent of using optical chopping schemes A and B. The elevated baseline measured using optical chopping scheme A is comprised of pump scatter, pump-induced PL, stray ambient light, and dark current from the detector. This will be a constant baseline that can be simply subtracted if the sample is not changing and measured using a typical TA apparatus where the pump and probe beams are both focused to small spots on the sample. The baseline is automatically subtracted in optical chopping scheme B using Eq. 2.11. Fig. 2.8a shows the undesirable contribution from pump scatter and pump-induced PL, calculated by

$$\frac{T_{10} - T_{00}}{T_{01} - T_{00}}. \tag{2.12}$$

The contribution from stray ambient light and detector dark current are subtracted to isolate the contributions unique to the T_{10} measurement. The contribution of pump scatter and pump-induced PL to the baseline is not necessarily equal at all pixels when using a spatially encoded measurement technique, necessitating the measurement of the baseline at each pixel.

While the cuvette holding the SR solution may have scratches that cause spatially dependent scatter, the main source of the difference between the $\Delta T/T$ signal calculated using optical chopping schemes A and B is owing to the PL of the sample. The impact of the extra pump-induced signals on the measured $\Delta T/T$ signal depends on the PL yield of the sample, the number of scattering features at the sample, and the intensity of the change in sample transmission caused by photoexcitation by the pump, the latter of which is the

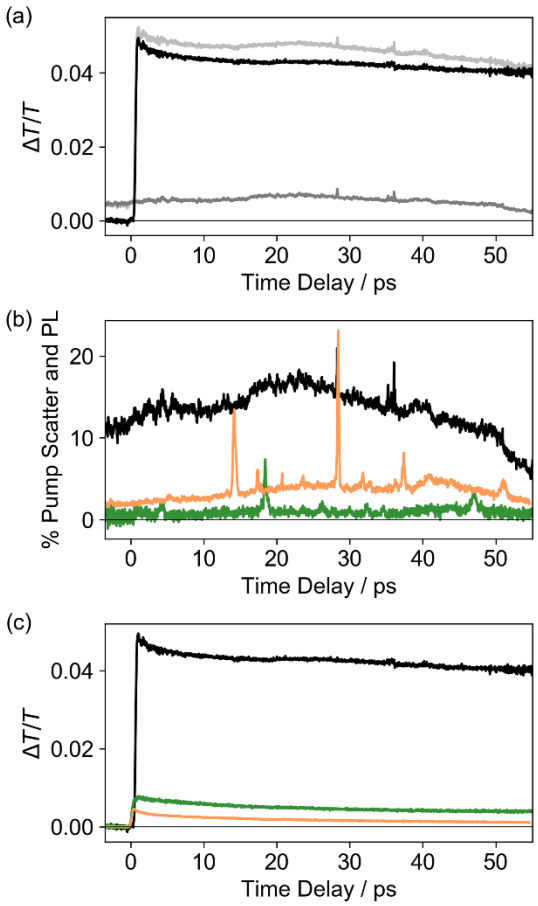

Fig. 2.8. Comparison of signal collected using optical chopping schemes A and B. (a) SSTA signal from SR collected using chopping scheme A (light grey), chopping scheme B (black), and the contribution of pump scatter and pump-induced PL as calculated using Eq. 2.12 (dark grey). (b) Percent of signal comprised by pump scatter and pump-induced PL for SR in solution (black), SR in a film (green), and P3HT (orange), calculated using the signal collected at a time delay of 40 ps using optical chopping scheme A as the nominal signal intensity. (c) Comparison of SSTA signal from SR solution (black), SR film (green), and P3HT (orange) using optical chopping scheme B after correction for pump scatter and PL using Eq. 2.11. Reprinted with permission from ref 3 © Elsevier B. V.

desired signal. Fig. 2.8b shows the percentage of the acquired signal using optical chopping scheme A that is comprised of the undesired pump scatter and pump-induced PL, where we use the signal at 40 ps as the nominal amplitude of the acquired signal. While the SR solution is photoluminescent and thus the undesirable contributions calculated by Eq. 2.12 have greater intensity, the differential transmission caused by the excited states is also fairly strong ($\Delta T/T \sim 4 \times 10^{-2}$). Once the SR molecules aggregate and form a film they are

not as photoluminescent, and while the film has more scattering features than the cuvette holding solution, the intensity of the undesirable contributions from scatter and PL is smaller in the film than in solution. Finally, the film of P3HT is neither highly photoluminescent nor highly scattering, but the signal generated by P3HT at the pump intensities that prevent photodamage and interactions between excited species is also lower (~4×10^{-3}, Fig. 2.8c). The small amount of scatter and PL from the P3HT film still constitutes ~3% of the desired $\Delta T/T$ signal, with spikes of contribution from pump scatter at time delays corresponding to spatial locations on the film with structural features that cause a particularly large contribution from scatter.

It is noteworthy that the amount of pump scatter and pump-induced PL measured for SR is different for the solution and the film. It is common for the PL yield and PL spectrum of organic small molecules and polymers to change as they aggregate and crystallize owing to the formation of H- or J-aggregates that may exhibit weaker or stronger PL, respectively.[63] Without accounting for this changing PL, measurements of the excited state dynamics during molecular aggregation using SSTA would be incorrect owing to the evolving contribution of PL. Films are, generally, also highly scattering in comparison to solutions. Not accounting for this dynamic contribution could invalidate an SSTA measurement during film formation.

In summary, we have performed SSTA measurements on prototypical organic semiconducting films comprised of small molecules (SR) or conjugated polymers (P3HT) as well as small molecules in solution (SR) exhibiting high PL. An optical chopping scheme is presented that enables the shot-to-shot correction of pump scatter and pump-induced PL. To our knowledge, this is the first demonstration of the use of a spatially

encoded time delay to measure the excited state dynamics of organic films with shot-to-shot corrections for pump scatter and pump-induced PL. Since these two contributions are dynamic as molecules aggregate and structural features evolve, this advance enables SSTA to measure the excited state dynamics of organic molecules as they form solution-cast films.

Deposition Stage Design

The sample stage for SSTA measurements requires a number of features that are unique for both the design and use of the instrument. A homebuilt sample stage with accurate positional, tilt, and temperature control is shown in Fig. 2.9. The pump-probe time delay is projected onto the spatial axis of the sample. To accurately acquire the time delay, the sample position must be imaged onto the spectrograph entrance slit. Imaging is accomplished through a 4f system with 200 mm and 150 mm plano-convex lenses as the objective and tube lenses, respectively. The tube lens is infinity focused for the spectrograph slit. The sample stage is brought into focus using a manual translation stages (Newport, 423) with a high-resolution micrometer (Newport, SM-25) attached to the side rails.

In situ SSTA measurements of samples during solution deposition or thermal annealing require tilt and accurate temperature control. Tilt control is essential for solution cast deposition methods. A non-level surface will affect the distribution of the solution onto the substrate and ultimately impact the film quality. The deposition stage is attached to two mounting rails using 1/4-20 screws into the bottom of the stage. The mounting rails rest on the side rails using three 1/4-80 ball-tipped screws (Thorlabs, F25SS116) which rest into recessed holes on the side rails. The ball-tipped screws are

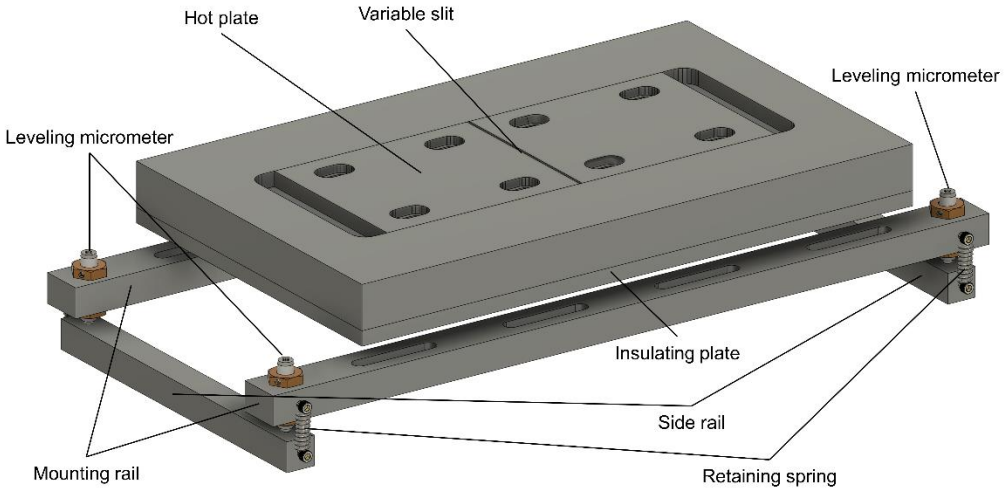

Fig. 2.9. Homebuilt sample deposition stage.

threaded into bronze bushings (Thorlabs, N80L7P) mounted in milled holes at the ends of the mounting rails. The mounting rails and side rails are also joined using springs mounted by 4-40 cap screws. Using a level at the measurement position, the three micrometer screws are adjusted. Temperature is controlled by two cartridge heaters embedded into the stage, one on either side of the variable slit beneath the adjustable copper hot plates. The temperature controller uses thermocouples to regulate the temperature of each half of the stage. In order to maximize contact between the hot plates and the sample, the hot plates' positions can be adjusted to minimize the slit width beneath the sample while still permitting the pump and probe beams to pass through. A tapered edge on each plate at the slit mitigates any imaging issues caused by clipping the probe beam as it defocuses after the sample position. Each plate is embedded in the larger plate by four 1/4-20 low profile screws. The larger plate improves temperature stability and uniformity across the hot plates. An insulating block limits heat flow from the larger plate to the mounting rails and positioning components. The planar stage surface enables access to the sample by other experimental equipment required during SSTA

measurements such as a sample translation stage, deposition equipment, and optical fibers for in situ absorbance and photoluminescence measurements. In order to protect the mirror located beneath the stage, a sheet of aluminum foil with a slit to permit the probe beam to pass through is installed. This prevents thermal radiation from affecting the mechanical components and mirror pointing.

CHAPTER III

CALIBRATION AND ANALYSIS OF SINGLE-SHOT TRANSIENT ABSORPTION MEASUREMENTS

Includes co-authored material from:

> Wilson, K. S.; Mapile, A. N.; Wong, C. Y.; Wong, C. Y.; Wong, C. Y. Broadband Single-Shot Transient Absorption Spectroscopy. *Opt. Express, OE* **2020**, *28* (8), 11339–11355.

Introduction

Calibration methods for typical TA measurements are straightforward. Spectral calibration is performed with a calibration light source across the one-dimensional array detector using standard calibration techniques. Time delay calibration was described by Eq. 2.1 using the translation stage positions relative to time zero and the speed of light. SSTA measurements require more involved spectral and time delay calibration techniques. One more axis of calibration is essential in SSTA measurements. In typical TA measurements, the signal at each time delay is acquired with the same pump intensity. When the time delay is spatially encoded, each time delay is acquired with its own pump intensity dependent on the spatial profile of the pump. In this chapter techniques for wavelength, time delay, and pump intensity calibration are detailed.

Wavelength Calibration

A HgAr calibration source (Ocean Optics) is collimated from an optical fiber and focused to a line at the sample plane, which is imaged through a spectrograph onto a 1000 x 2560 pixel area of interest on an array detector. Minor aberrations in the imaging optics (Fig. 3.1a) require that wavelength calibration be performed for each column of pixels.[64] A central column of pixels is spectrally calibrated by visual inspection. This initial calibration is then propagated from the center column to the edges of the image,

shown in Fig. 3.1a. To determine the position of each peak with sub-pixel resolution, the five pixels nearest to the previously assigned peak position in the neighboring column are averaged, weighted by their intensities. Fig. 3.1b shows the intensity profile for a spectral line at 763.511 nm from two pixel columns with symbols marking the intensity of the five pixels closest to the peak assignment from its respective neighboring column. A 3D surface correlating both pixel axes to wavelength is fit using a bivariate polynomial using the identified calibration peak locations across the image. This fit is then applied to the entire image, shown in Fig. 3.1c.

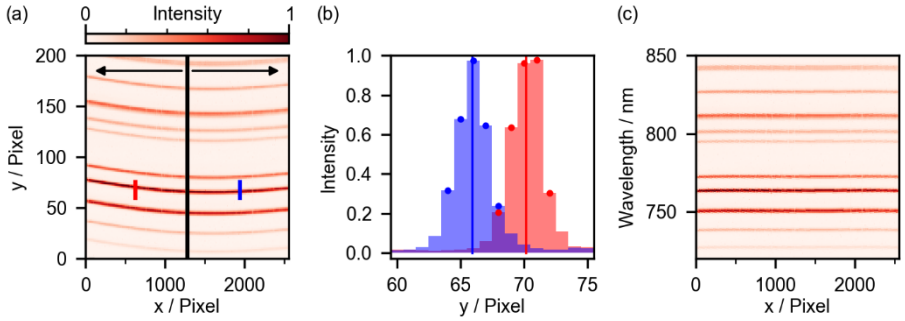

Fig. 3.1. Spectral calibration of the array detector. (a) Spectral lines of HgAr light source with aberrations. A central pixel column (black) is spectrally calibrated. The calibration is propagated to the edges of the image (arrows). Red and blue lines highlight pixel columns 633 and 1942, respectively, of the spectral line at 763.511 nm. (b) Pixel intensity profile of 763.511 nm spectral line for pixel columns 633 (red) and 1942 (blue). The central pixel position of each peak (lines) is determined by the weighted average of the marked pixels. (c) Spectrally calibrated image from (a). Reprinted with permission from ref. 15 © The Optical Society.

Time Delay Calibration

Each pixel in an acquired image reports on a particular pump-probe time delay when the probe beam is imaged onto the array detector. A uniform change in these time delays can be imparted by changing the path length of either the pump or the probe beam using a retroreflecting mirror on a translation stage, a mechanism used in typical TA instruments. SSTA measurements performed at a series of translation stage positions are used to calibrate the spatially encoded time delay since the delay imposed by the

translation stage can be precisely determined, as can the pixel at which time zero occurs.[10–12,20,27,65]

Since temporal chirp causes time zero to vary as a function of wavelength, a careful two-dimensional calibration must be performed to determine the relative pump-probe time delay of every pixel in the acquired images of spectrally resolved probe pulses. Minami et al. reported time delay calibration with spectral chirp using signal from a Kerr medium.[23] We demonstrate a calibration method that can be performed with any resonant sample.

SSTA measurements are performed at a series of different retroreflector positions. A broadband SSTA measurement at a particular retroreflector position (arbitrarily assigned to be 0 ps) is shown in Fig. 3.2a. Temporal chirp affects the horizontal pixel at which time zero is observed, resulting in the curve shown in Fig. 3.2a. At any particular wavelength, the pixel location of time zero shifts as the retroreflector is translated, Fig. 3.2b. The pixel at which time zero occurs is determined for each retroreflector position by finding the maximum of a step function (simulating time zero) convoluted with the signal along the pixel axis. The location of the maximum for this convolution corresponds to the best overlap between the simulated step function and the signal. This analysis is performed for each wavelength across the entire range of time delays induced by the retroreflector. Fig. 3.2c shows a 30-pixel strip of SSTA data around time zero for a few retroreflector positions. Using the identified pixel locations of time zero, a 3D surface correlating spatial pixels and wavelength to retroreflector time delays can be fit using a bivariate polynomial. This fit is then applied to the entire image, assigning a relative spatial time delay to each pixel at each wavelength. Agreement between the time delay

imparted by the translation stage with the spatially encoded time delay is shown in Fig. 3.2d.

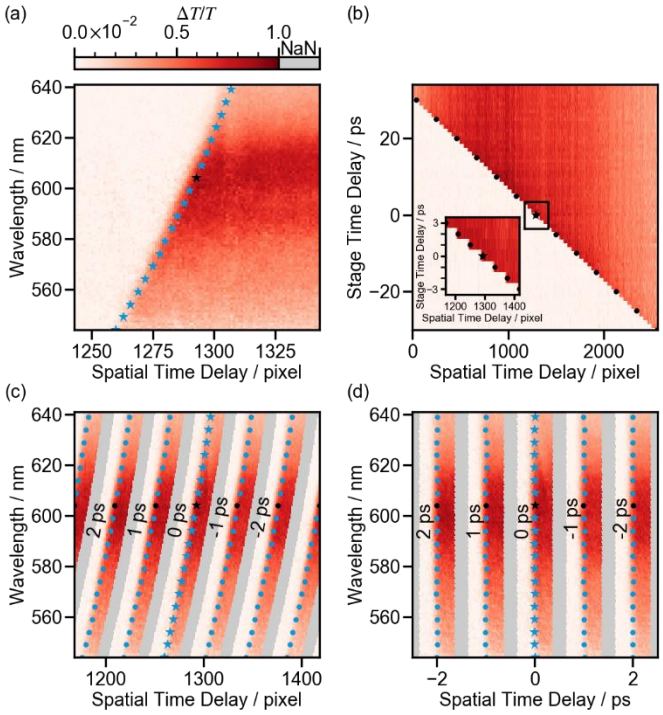

Fig. 3.2. Spatial pixel time delay calibration. Each marker represents the pixel location of time zero for a particular wavelength at a specific retroreflector stage time delay position. Time zero when the stage time delay is 0 ps is shown by stars, all other stage time delays are marked as circles. Time zero for 604 nm is shown by black symbols, all other wavelengths as blue symbols. (a) Broadband $\Delta T/T$ signal with the retroreflector stage set to a time delay of 0 ps. For each wavelength, the location of time zero corresponds to a different spatial time delay pixel (horizontal axis). (b) $\Delta T/T$ signal at 604 nm as function of spatial location and retroreflector positions. For each retroreflector position, the location of time zero corresponds to a different spatial time delay pixel (horizontal axis). Inset: Expanded region at stage positions near 0 ps. (c) Spatial $\Delta T/T$ signal where each strip (separated by grey) represents the signal around time zero at specific retroreflector positions (labels). (d) Analogous plot to (c) after spatial time delay calibration. Reprinted with permission from ref. 15 © The Optical Society.

Pump Profile Correction

Effect of the Pump Profile on SSTA Measurements

In order to obtain an accurate transient spectrum of the sample, the pump pulse must cause the same excited state dynamics throughout the entire excitation volume. The SLM in our instrument reshapes the pump pulse such that the excitation density across

the spatial time delay range is consistent, but any remaining imperfections in the uniformity of the resulting pump profile will impact SSTA measurements. For example, a flat-top target pump profile (Fig. 3.3a, grey) was used to generate a phase map to reshape the pump profile. SSTA measurements were acquired using a retroreflector stage position that caused the entire spatially encoded time delay range to be after time zero (Fig. 3.3b, grey). This signal should report the dynamics of the excited state population in cresyl violet as a function of time, but small residual deviations from a perfectly flat pump profile result in small amplitude differences in the SSTA signal since the intensity of the pump beam determines the intensity of the measured $\Delta T/T$ signal. The effect of the pump profile on SSTA measurements is more clearly demonstrated by using a pump profile modified to include three peaks (Fig. 3.3a, black), resulting in larger $\Delta T/T$ signal at pump-probe delay times that are measured in areas exposed to higher pump intensity (Fig. 3.3b, black). This SSTA signal clearly does not accurately report the excited state dynamics of cresyl violet.

Normalizing the Spatially Encoded Transient

We have developed a method that normalizes the $\Delta T/T$ signal by the pump intensity profile to reveal a transient spectrum that accurately describes the sample. Previously reported methods to normalize the signal by the pump intensity profile have drawbacks, such as requiring a separate detector [13] or requiring samples that are sensitive and exhibit particular behaviors at the pump wavelength.[34] We have found that photoluminescence detected images of the pump profile do not exactly match the strength of the measured $\Delta T/T$ signal. One correction strategy is to use signal from a long-lived dye at a time delay significantly after time zero assuming that changes in the signal are

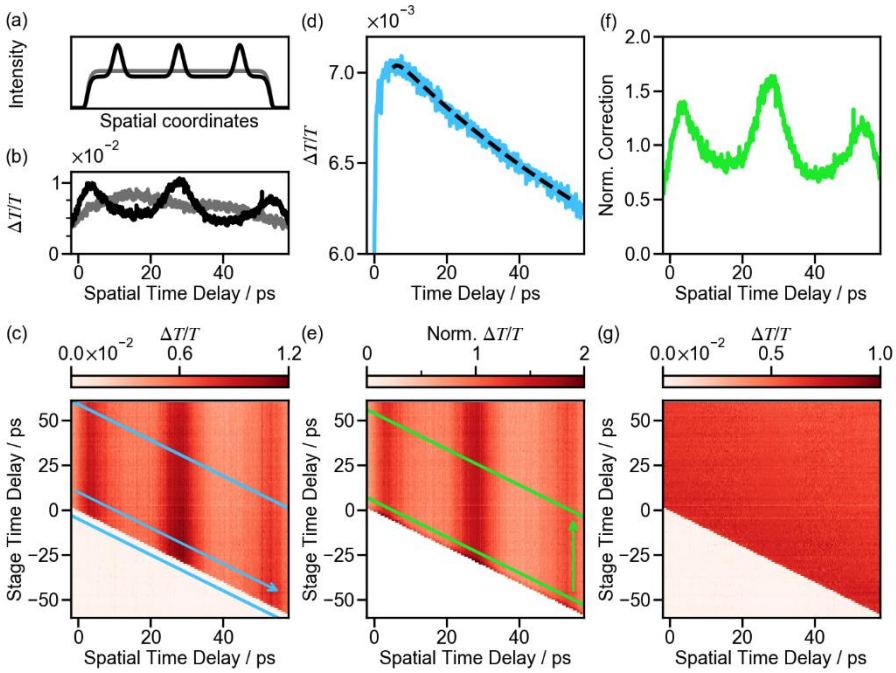

Fig. 3.3. Pump profile reshaping and correction for SSTA measurements of cresyl violet at a probe wavelength of 615 nm. (a) Target pump profiles used to reshape the pump beam with 3 peaks (black) and flat-top (grey). (b) Actual pump profiles measured using SSTA with target profiles in (a). (c) SSTA signal at 615 nm at different retroreflector time delay positions, where each vertical slice represents a traditional transient measured by each pixel and each horizontal slice is a spatially encoded TA signal using the 3-peaked pump profile from (b). The TA signal with corresponding relative time delays from each pixel in the blue box is averaged in the direction of the arrow. (d) The averaged TA signal (blue) is fit to a tri-exponential function (black) from 5 to 55 ps. (e) TA signal from (c) normalized by the tri-exponential fit from (d). The normalized signal in the green box is averaged for each pixel in the direction of the arrow to obtain the spatially dependent pump profile, (f). (g) The raw SSTA signal (c) is corrected using the extracted pump profile (f) to factor out the effects of a non-uniform pump profile. Reprinted with permission from ref. 15 © The Optical Society.

negligible over the time range of the spatially encoded signal.[12,43] This approach is valid for single-color SSTA with a small spatial time delay of 1 ps, but is insufficient when a longer time delay range of 60 ps is used. Herein, we demonstrate that our novel correction method is robust to significant deviations from a perfectly flat pump profile by using the pump profile with three peaks shown in Fig. 3.3a for broadband SSTA measurements of cresyl violet in methanol. This correction method is shown for the

transient at 615 nm and was repeated for each wavelength in the acquired broadband spectrum.

Each pixel on the detector can measure a separate transient by scanning the position of the retroreflector on a translation stage to achieve time delays from -60 to 60 ps, shown in Fig. 3.3c. The signal can be represented as

$$S_{measured}\left(x, t\left(x, d\right)\right) = I_{pump}\left(x\right) \cdot k \cdot S_{sample}\left(x, t\left(x, d\right)\right) \pm \sigma\left(x\right) \tag{3.1}$$

where $S_{measured}$ is the transient signal acquired by pixel x at time delay t, which is a function of both the pixel and translation stage position, d. The intensity of $S_{measured}$ is determined by the intensity of the pump, I_{pump}, and the inherent sample response, S_{sample}, at the location imaged by each pixel with k as a proportionality factor. The signal error, σ, for each pixel is the standard deviation of $S_{measured}$, and is usually the result of laser fluctuations and/or detector noise that is independent of pump-probe time delay. As a result of the relation in Eq. 3.1, three higher intensity peaks are evident across the spatial time delay axis in Fig. 3.3c when a pump profile that includes three peaks is used. While the signal intensity for each pixel depends on the pump intensity, S_{sample} is uniform for every pixel as long as the sample is spatially homogeneous within the excited region and the pump intensity is low enough to avoid interaction between excited species. The relationship between the pump intensity and the $\Delta T/T$ signal is linear when using these energy densities, allowing for the correction of non-uniformity in the signal using the pump profile. As a result, the average transient signal intensity from the same pump-probe time delay range for each pixel can be used as a normalization factor for that pixel to correct for the pump intensity. This is calculated by

$$I_{pump}(x) \propto \frac{1}{n(x) - m(x)} \sum_{i=m(x)}^{n(x)} S_{measured}(x, t(x, d_i)) \tag{3.2}$$

where d_i denote translation stage positions, enumerated from m to n. Indices m and n are determined by pixel x such that the time delay range $t(x, d_{m(x)})$ to $t(x, d_{n(x)})$ is the same for all x. The time delay range imposed by the translation stage is chosen such that the signal does not change sign during this time range and does not include time zero. This method for determining $I_{pump}(x)$ can result in artifacts if the signal intensity changes significantly relative to the time delay step size of the measurement. These artifacts are demonstrated in the next section.

The Impact of Translation Stage Step Size and Excited State Dynamics On Determining The Pump Profile

To determine the pump profile, SSTA measurements are taken at a range of translation stage positions, d_i, with a time delay step size of Δt_{step}, modeled in Fig. 3.4a. Transient signal is measured by each pixel, x, at time delays $t(x, d_i)$. Each pixel's time delay is shifted as a result of the angle between the pump and probe pulses. As Eq. 3.2 notes, the pump intensity is calculated by averaging signal within a particular time delay range which is chosen to be the same for each pixel and is denoted here as t_0 to t_1, shown in Fig. 3.4b. However, unless Δt_{step} is smaller than the time delay difference between adjacent pixels, the actual time delay range $t(x, d_{m(x)})$ to $t(x, d_{n(x)})$ for some pixels can be shifted up to $\Delta t_{step} / 2$ from the target time delay range. This is evident in Fig. 3.4b, where the measured time range for the blue pixel is significantly shifted from the time range measured by the green pixel. As a result, the average signal will not be calculated

from the exact same time delay range, which causes sawtooth artifacts in the calculated pump profile. This is shown in Fig. 3.4c, where the average signal from the blue pixel is calculated using a time delay range that is slightly earlier than the time delay range used to calculate the average signal from the green or purple pixels. The magnitude of the artifacts is dependent on Δt_{step} and the change in signal over Δt_{step}. Decreasing Δt_{step} will reduce the effect but can dramatically increase the data acquisition time for this calibration step and still may not fully remove the artifacts.

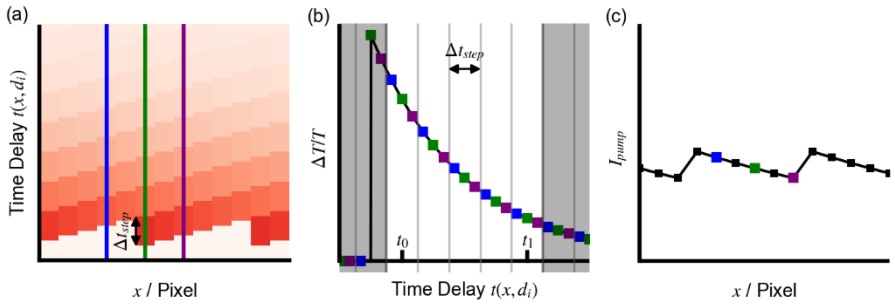

Fig. 3.4. The effect of the translation stage step size, Δt_{step}, on the pump profile calculated from Eq. 3.2. (a) Simulated $\Delta T/T$ signal (false color) for pixels at time delays $t(x,d_i)$ imparted at translation stage positions d_i. The translation stage time delay step size is Δt_{step}. Transients at different pixels (blue, green, purple) are compared in (b). (b) Transients from (a) are marked by symbols onto the full transient (black). Data outside the time delay range from t_0 to t_1 (gray) are excluded from Eq. (3.2). (c) The pump intensity calculated from the data in (b) using Eq. (3.2). Reprinted with permission from ref. 15. © The Optical Society.

To avoid effects resulting from any time-dependent component in the pump profile, $S_{measured}(x,t)$ could be normalized by $S_{sample}(t)$. S_{sample} is not directly known, but averaging the signal from all of the pixels using the same relative translation stage time delay range (Fig. 3.3c, blue box and arrow) results in an average transient signal, $\bar{S}_{measured}$, (Fig. 3.3d, blue) that is dependent on S_{sample} but not on the spatial pump profile.

The average transient signal, $\bar{S}_{measured}$, of all of the pixels is determined using SSTA measurements conducted at a series of translation stage positions that impose time

delays in steps of Δt_{step}, typically 1-3 ps, from -60 to 60 ps. This time delay range is double the spatially encoded time delay range of the instrument, 60 ps, which ensures that every pixel has 60 ps of data after time zero. To determine the average transient signal, a new array of time delays from -5 to 60 ps with a resolution of Δt^*_{step}, typically 0.1 ps, is defined where $\Delta t^*_{step} < \Delta t_{step}$. For each time point in the array, a fraction of the pixels (approximately $\Delta t^*_{step} / \Delta t_{step}$) have a data point that is within $\Delta t^*_{step} / 2$ of that time point. The signal from these pixels is averaged and assigned to that time point. Every time point in $\bar{S}_{measured}$ then consists of signal from pixels that are evenly distributed across the image. The SNR in this transient is significantly higher than the SNR for a transient from any individual pixel, ideal for use in normalizing the spatially encoded transient. For cresyl violet, the SNR of $\bar{S}_{measured}$ is ~270 vs. ~25 for an individual pixel. This results in an average transient signal of

$$\bar{S}_{measured}(t) = \bar{I}_{pump} \cdot k \cdot S_{sample}(t) \tag{3.3}$$

where $\bar{I}_{pump}$ is the average pump profile intensity at all of the pixels. $\bar{S}_{measured}$ has a lower SNR than the transient measured by any individual pixel. It is fit using a tri-exponential decay function (Fig. 3.3d, black). The fit equation, represented by $\hat{S}_{measured}(t)$, is evaluated for each pixel at each time delay, $t(x, d)$, resulting in a calculated signal for each pixel in the collected image. By dividing Eq. 3.1 (a vertical slice from Fig. 3.3c) by the calculated signal for each pixel, the dependence on the transient signal is removed and only the pump intensity remains,

$$\frac{S_{measured}\left(x,t\left(x,d\right)\right)}{\hat{S}_{measured}\left(t\left(x,d\right)\right)} = \frac{I_{pump}\left(x\right)}{\overline{I}_{pump}} \pm \frac{\sigma\left(x\right)}{\hat{S}_{measured}\left(t\left(x,d\right)\right)}. \tag{3.4}$$

$$= I_{norm}\left(x,d\right) \pm \sigma_{norm}\left(x,t\left(x,d\right)\right)$$

where I_{norm} is the normalized pump intensity at the corresponding pixel, *x*, and σ_{norm} is the error for each pixel. Fig. 3.3e shows I_{norm} over a range of time delay positions, with signal before time zero set to zero for clarity. Artifacts arising from the dynamics are removed since the intensity of I_{norm} is not time dependent.

Determining the Pump Profile from Normalized SSTA Measurements

The normalized pump profile correction factor is acquired by averaging over a time delay range using the following equation

$$\overline{I}_{norm}\left(x\right) = \frac{\sum_{i=m(x)}^{n(x)} w\left(x,t\left(x,d_i\right)\right)\cdot I_{norm}\left(x,d_i\right)}{\sum_{i=m(x)}^{n(x)} w\left(x,t\left(x,d_i\right)\right)} \equiv \frac{I_{pump}\left(x\right)}{\overline{I}_{pump}} \tag{3.5}$$

where the normalized intensity at each translation stage position for a pixel is weighted by

$$w\left(x,t\left(x,d_i\right)\right) = \sigma_{norm}\left(x,t\left(x,d_i\right)\right)^{-2}, \tag{3.6}$$

which is a common weighting scheme for data sets with variability in the error of each point. This is performed for every pixel across the chosen time delay range, which for cresyl violet was 5-55 ps. The time delay range and axis along which the data are averaged are represented in Fig. 3.3e by the green box and arrow, respectively. The effective pump profile at 615 nm is shown in Fig. 3.3f. Once this is acquired, the signal for each pixel is corrected by the pump profile. This is accomplished by dividing Eq. 3.1 by $\overline{I}_{norm}$, resulting in

$$S^{*}_{measured}\left(t\left(x,d\right)\right) = \bar{I}_{pump} \cdot k \cdot S_{sample}\left(t\left(x,d\right)\right) \pm \frac{\sigma\left(x\right)}{\bar{I}_{norm}\left(x\right)} \tag{3.7}$$

where the intensity of the signal, $S^{*}_{measured}$, is now determined by the average intensity of the pump profile across the spatial time delay axis and is no longer dependent on the pump's spatial profile. Fig. 3.3g shows the SSTA signal for all of the pixels from Fig. 3.3c after they have been normalized by the pump profile.

Comparison of SSTA and Conventional TA Measurements

Through this process, the impact of the three peaks in the pump profile has been corrected, resulting in spatially encoded transient signal representative of the sample. SSTA measurements of cresyl violet are compared with the extracted traditional transient spectra to validate this correction method. Fig. 3.5a shows the corrected SSTA spectra for cresyl violet. Horizontal slices represent transients at particular wavelengths. Vertical slices are transient spectra at particular time delays. Single-shot transients at different wavelengths (Fig. 3.5b, grey) are compared with $\bar{S}_{measured}(t)$ from Eq. 3.5 (Fig. 3.5b, dashed). The different dynamics measured at these two wavelengths is accurately captured by SSTA. A comparison of these transients with the three peaks in the pump profile show that the regions of the transients with poor SNR correspond to regions of the sample that are excited with lower pump intensity. This noise can be minimized by using a uniform pump profile. Single-shot transient spectra at 250 fs, 10 ps and 40 ps (Fig. 3.5c, solid) are compared with transients measured in a traditional manner (Fig. 3.5c, dashed), showing that SSTA accurately reports the red shift in the peak location during the first 10 ps.[66] The SNR for a transient measured using a single pixel is 25 after 55 min. of data collection. The SSTA transient has a SNR of 18 after 20 s of data collection.

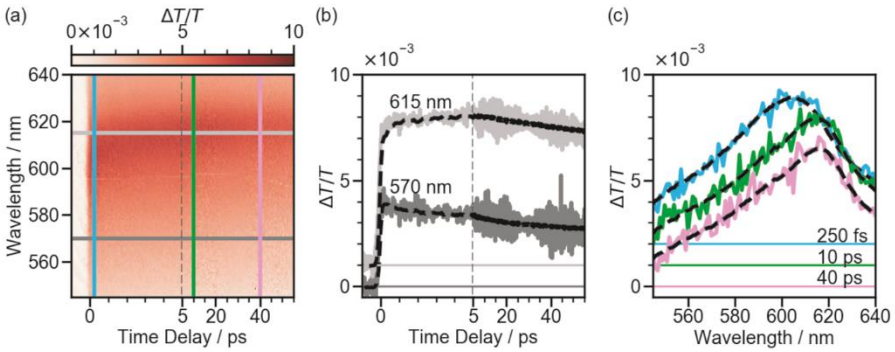

Fig. 3.5. Comparison of SSTA and traditional TA signal of cresyl violet in methanol. SSTA and traditional TA measurements were acquired in 20 s and 55 minutes, respectively, where the traditional TA signal is a composite of signal collected by all 2560 pixels of the detector. (a) Broadband SSTA signal with transients (horizontal) at 575 (dark grey) and 615 (light grey) nm compared with corresponding traditional TA measurements (b, black) at the same wavelength. Transient spectra (vertical) at time delays of 0.25 (blue), 10 (green), and 40 ps (purple) are compared with corresponding traditional TA measurements (c, black) at the same time delay. Vertical dashed lines in (a) and (b) denote a change in the time delay scale. Signal in (b) and (c) are offset by 0.001 for clarity. Reprinted with permission from ref. 15 © The Optical Society.

In this section, we have shown a method that corrects for spatial deviations in the pump intensity. While the SLM does generate a relatively uniform pump profile, raw SSTA data demonstrate that there are still artifacts that arise from subtle deviations from a perfectly uniform profile. This method compensates for such deviations, even when they are significant, as demonstrated by using a pump profile with three distinct peaks. Despite this robustness, a uniform pump profile is ideal because it maximizes the signal response across the transient spectra while staying in a linear excitation regime, which prevents noisy regions in the measured transients evident in Fig. 3.5b. The pump profile acquired using this process can be used for in situ SSTA experiments, where the sample is constantly changing during data acquisition.

CHAPTER IV

TRANSIENT ABSORPTION MEASUREMENTS OF DIFFERENT SYSTEMS

Includes co-authored material from:

Wilson, K. S.; Wong, C. Y. In Situ Measurement of Exciton Dynamics During Thin-Film Formation Using Single-Shot Transient Absorption. *J. Phys. Chem. A* **2018**, *122* (31), 6438–6444.

Sadighian, J. C.; Wilson, K. S.; Crawford, M. L.; Wong, C. Y. Evolving Stark Effect During Growth of Perovskite Nanocrystals Measured Using Transient Absorption. *Front. Chem.* **2020**, *8*, 897.

Includes unpublished co-authored material.

Grant S. Hall and Marc J. Foster contributed to CuPc, PCBM, and P3HT thin film depositions. Marc J. Foster also performed TA measurements of P3HT:PCBM films under my direction. All of the contents in this section were written by me.

In Situ Measurements of Pseudoisocyanine Iodide during Thin Film Formation

Background

The dynamics of bound electron-hole pairs, termed excitons, is important for chemical systems where the fate of excitons determines functionality, such as semiconducting small organic molecules that can serve as the active layer in organic photovoltaics,[67–71] organic electronics,[72–75] and organic light emitting diodes.[76–78] Organic molecules are attractive for these applications since they are synthesized and chemically tunable using earth abundant materials and can be deposited into films from solution using roll-to-roll methods that are scalable for high-volume, low-cost production.[79,80] However, owing to weak intermolecular forces between organic molecules, subtle changes in environmental conditions during the deposition process can affect the relative orientation of molecules within an aggregate, influencing the metastable structures that are kinetically trapped.[81] Since local molecular arrangement determines electronic

coupling, and electronic coupling governs electronic structure and exciton dynamics, the aggregate structure can dramatically impact the suitability of a molecule for any particular application. For example, J-aggregates, which are highly photoluminescent and useful in light-emitting devices, can form as solvent vaporizes during the solution deposition of an organic molecule such as PIC. The sharp, red-shifted peak in the linear absorption spectrum of PIC films is ascribed to these J-aggregates, Fig. 4.1a. Multiple experimental and computational studies of the structure of these J-aggregates do not agree,[82,83] suggesting that structure may be sensitive to aggregation conditions. The formation of these J-aggregates can be better understood by measuring the evolving electronic structure and exciton dynamics in situ during aggregate formation.

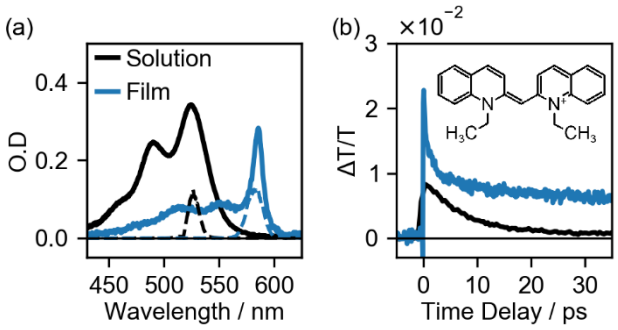

Fig. 4.1 (a) Absorption of PIC (solid) in solution and thin film and laser spectrum (dashed) used for each measurement. (b) TA measurements of PIC in solution and film collected using a translating retroreflector in 13 min and 40 min, respectively. Inset: Structure of PIC. Reprinted with permission from ref. 6 © The American Chemical Society.

Since linear absorption measurements can be completed quickly (< 1 ms) relative to the timescale of film formation (0.1 – 5 min), in situ measurements can help clarify how the electronic structure evolves during film formation. Exciton dynamics can be measured with femtosecond time resolution using TA spectroscopy.[84–86] Since the electronic structure clearly changes upon J-aggregate formation, it is unsurprising that the

exciton dynamics changes significantly as well, Fig. 4.1b. However, while in situ measurements of x-ray scattering,[87] linear absorption,[88] nuclear magnetic resonance,[89] and Raman spectroscopy[90] have proliferated, long data collection times have frustrated attempts to use in situ TA spectroscopy to measure the evolution of exciton dynamics during materials formation.

Transient signal is collected by photoexciting the sample using a pump pulse, and then measuring the transmission of the excited sample after a controlled time delay using a probe pulse. The time delay is typically controlled using a retroreflecting mirror on a motorized translation stage to vary the path travelled by one of the pulses. Thousands of laser shots are typically used for the transient absorption measurement at each time delay, and the procedure is repeated until an adequate SNR is achieved. This process typically requires many minutes to a few hours. Slowing down the process of film formation would enable the in situ measurement of exciton dynamics, but the structure of the resulting organic molecular aggregates can be extraordinarily sensitive to deposition conditions and the deposition process, as discussed above. Since the electronic structure depends on the aggregate structure, slowing down the aggregation process is not a viable strategy for determining the exciton dynamics during the aggregation of organic molecules. Instead, the measurement must be completed quickly relative to the materials formation process.

We employ the SSTA instrument, described in Chapter 2. These measurements capture a 45 ps time delay range with excellent SNR in a few seconds.[91] This enables the first-ever measurement of exciton dynamics in situ during film formation. The laser spectrum was tuned to overlap with the spectral feature at 583 nm ascribed to J-

aggregates,[92–94] Fig. 4.1a. The time delay is spatially encoded within the sample by expanding both the pump and probe beams, using a cylindrical lens to focus each beam to a line on the sample, and tilting the pump pulse relative to the probe pulse. SSTA instruments reported in literature that use either tilted pulses[95–103] or transmissive/reflective echelons[59,104–107] to spatially encode the pump-probe time delay have been used to measure exciton dynamics in molecules in solution[91,108,95] and in single crystals[104,105] during photodegradation. Spatially encoded TA has not been used to measure exciton dynamics during film formation, perhaps since it is commonly assumed that spatial encoding cannot accurately measure samples with spatial heterogeneity. In this work, we show that SSTA can accurately measure the ensemble exciton dynamics of a film of PIC molecular aggregates by translating the sample during the measurement to average over heterogeneity. We then use in situ SSTA during the formation of J-aggregates to reveal, for the first time, the exciton dynamics during the film formation process, including the exciton dynamics of an intermediate structure formed prior to the final, dry film. Concurrent in situ linear absorption and photoluminescence measurements support an intermediate stage consisting of highly photoluminescent J-aggregates with some remaining solvent, while the final stage consists of a dry thin film of disordered, less photoluminescent J-aggregates. The insights revealed by measuring practically relevant excitonic processes during materials formation with femtosecond time resolution using in situ SSTA will provide a deeper understanding of how functional materials are formed and enable a more rational approach to excitonic materials design.

Methods

A 1 kHz Ti:Sapphire (Coherent Astrella) laser produces 50 fs pulses that are tuned by an optical parametric amplifier to be resonant with the sample. After a beamsplitter, the probe pulse passes through a beam expander and a retroreflecting mirror mounted on a motorized delay stage (Newport, XPS-Q8) that is used to calibrate the spatially encoded delay and to collect transients in the traditional manner. The probe beam passes through a cylindrical lens and is normally incident on the sample. The pump pulse passes through a half-wave plate and a polarizer to set the pump:probe energy ratio to 10:1. After an optical chopper and beam expander, the pump interacts with a spatial light modulator (SLM, Meadowlark). An iterative algorithm is used to find a phase map for the SLM that results in a flat intensity profile at the sample position. The pump beam for these measurements is focused by a cylindrical lens and is tilted by 42.5° relative to the probe pulse.[91] The two beams are overlapped to a 20 mm x 25 μm line on the sample. After passing through the sample, the pump beam is blocked and the probe beam is imaged onto a CMOS camera (Andor Zyla 5.5). A 20 × 2560 image is taken for each shot using a 1 ms exposure time and each column is summed to generate a 1 × 2560 transmission image, T. The optical chopper blocks alternate pump pulses, and the normalized differential transmission, $\Delta T/T$, is $(T_{pump\ on} - T_{pump\ off}) / T_{pump\ off}$.

When using a spatially encoded time delay it is important to ensure that the entire measured volume of sample is photoexcited within the linear regime, without interaction between excitons. If one region of the spatial profile of the pump photogenerates a high density of excitons that could annihilate or interact, that spatial region will exhibit exciton dynamics that are different from regions with a lower exciton density. SSTA signals were

measured in a PIC film using pulse energies from 0.75 μJ to 2.0 μJ. As shown in Fig. 4.2, the spatially encoded exciton dynamics captured over this range of pump energies is indistinguishable, with a linear dependence of ΔT/T on pump energy. The pump pulse energy was set to 1.6 μJ for the measurements reported below.

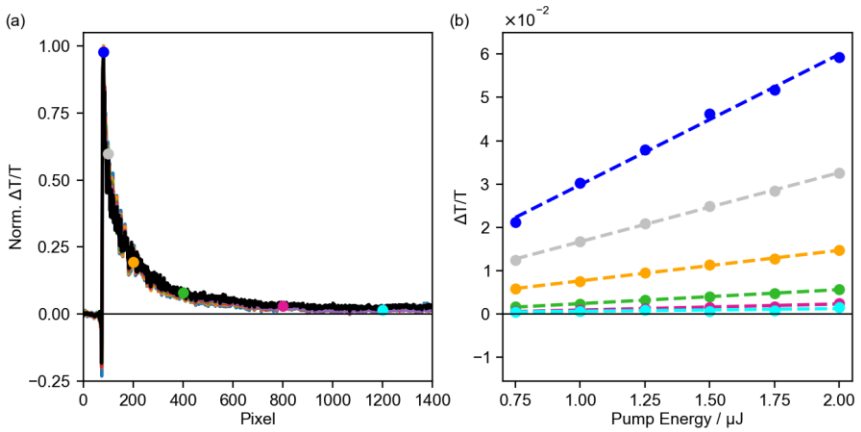

Fig. 4.2. (a) Overlay of normalized SSTA signal of a stationary PIC thin film during the intermediate stage for pump energies of 0.75, 1.00, 1.25, 1.50, 1.75, and 2.00 μJ. (b) Dependence of SSTA signal on pump energy before normalization. Colored circles correspond to the pixel being considered, shown in (a). Linear fits (dashed) demonstrate that the pump energy is within the linear regime throughout the excited region of the sample. Reprinted with permission from ref. 6 © The American Chemical Society.

Concurrent TA and SSTA measurements of a PIC film are used to calibrate the spatial time delay of the instrument, as discussed in Chapter 3. The film is translated during measurement to average over defects like dust particles or scratches. Spatially encoded transient signals are measured at a range of retroreflector positions. Time zero, the retroreflector position that results in the overlap of the pump and probe pulses in time, is different for each sample location along the focal line owing to the tilted pump pulse. The relationship between time zero and sample location is very close to linear. A cubic fit of the time zero positions accounts for small deviations from perfectly flat wavefronts and calibrates the pump-probe time delay range to an average of 22.8 fs/pixel.

Conjointly with SSTA measurements, in situ absorption and photoluminescence measurements are collected via optical fibers (Thorlabs, M28L01) into USB spectrometers (Ocean Optics, Flame-T-VIS-NIR and Flame-T, respectively) with integration times of 280 and 500 ms, respectively. Absorption measurements use a combined light source of a green LED (Uxcell, 510 nm) and a broadband LED (Thorlabs, MWWHL3) joined using a bifurcated 6:1 optical fiber (Thorlabs, TP22) and focused at the sample plane. photoluminescence measurements use a 532 nm LED laser excitation source. Because photoluminescence measurements are performed concurrently with SSTA, background photoluminescence from the ultrafast pulses is also detected. To correct for this, the LED laser is alternately switched on and off every second using a home-built circuit and the measurement with the laser on is subtracted by the in situ background obtained when the laser is off.

The sample stage consists of an aluminum block with a slot through which the pump and probe pulses can pass, oriented to allow samples to sit horizontally above the measurement slot during thin-film formation. In these experiments the temperature of the stage is controlled by a recirculating water chiller and maintained at 13 °C. A cover is placed over the apparatus to control airflow. A slow flow of nitrogen maintains a 29% humidity level. Microscope slides are sonicated in methanol and dried using nitrogen. PIC is dissolved in acetone through sonication and 0.4 mL are dropcast onto a 2” × 1” microscope slide on the cooled sample stage. In situ SSTA, absorption and photoluminescence measurements, as described above, are initiated simultaneously with dropcasting. Upon formation of the intermediate, a motorized actuator (Newport,

TRB25PP) translates the sample at a velocity of 0.3 mm/s until after the final film has formed.

Results and Discussion

Concurrent SSTA and TA measurements of a PIC thin film are used to calibrate the spatial time delay, as described above, and also to ensure that the SSTA instrument accurately measures dynamics of a film with some spatial heterogeneity. Vertical and horizontal slices from Fig. 4.3a correspond to exciton dynamics measured by translating the retroreflector and by using the spatially encoded time delay, respectively. The dynamics measured by translating a retroreflector agrees with the dynamics measured using the spatially encoded time delay, Fig. 4.3b, demonstrating the accuracy of the SSTA instrument. Using the spatially encoded time delay a SNR >20 can be achieved in 2 s, enabling the measurement of exciton dynamics in molecules as they aggregate to form films. The acquisition time and film area needed to average over spatial heterogeneity will depend on the degree and type of heterogeneity in the sample.

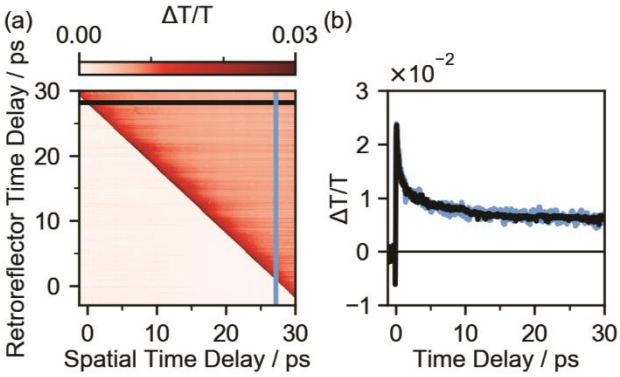

Fig. 4.3. Comparison of SSTA and traditional TA measurements of PIC. (a) SSTA measurements taken over a range of time delays generated by translating a retroreflector. (b) Slices from (a) show comparable exciton dynamics measured using traditional TA and SSTA collected in 14 min and 2 s, respectively. Reprinted with permission from ref. 6 © The American Chemical Society.

The process of PIC film formation occurs in ~30 s using our deposition method and conditions. In situ linear absorption, photoluminescence, and SSTA were measured during the thin-film formation process, Fig. 4.4. The plot of linear absorption as a function of real time, Fig. 4.4a, shows that molecular aggregation proceeds through three distinct stages, which we term the 'solution', 'intermediate', and 'film' stages, with clear changes in the spectral features at 0 s and ~20 s. In this work, we focus on the J-aggregates, which produce the strong, narrow absorption feature at 583 nm during the intermediate stage, between 0 s and 20 s. This feature then broadens (shown in Fig. 4.5) and slightly redshifts when it has formed a film. Absorption spectra collected during the solution, intermediate, and film stages are compared in Fig. 4.4b. The three stages of the aggregation process are also evident in the photoluminescence spectra, Fig. 4.4c. In solution, the photoluminescence is below the detection limit of our instrument. Upon formation of the intermediate stage, the film becomes highly photoluminescent at 583 nm. After undergoing the transition to the final film, the photoluminescence intensity decreases, the spectrum slightly red-shifts to 585 nm, both shown in Fig. 4.4d, and the line width broadens, Fig. 4.5.

SSTA was measured during film formation using laser pulses centered at 583 nm, resonant with the narrow band arising from J-aggregates. The exciton dynamics during the intermediate stage is clearly different from the dynamics measured in the film stage, as shown in Fig. 4.4e, where each SSTA transient is the average of 500 shots collected in 1 s while translating over a 12 mm × 0.3 mm area of sample. Fig. 4.4f compares transients collected during the intermediate and film stages. The TA signal immediately after photoexcitation is larger in magnitude during the intermediate stage than in the film

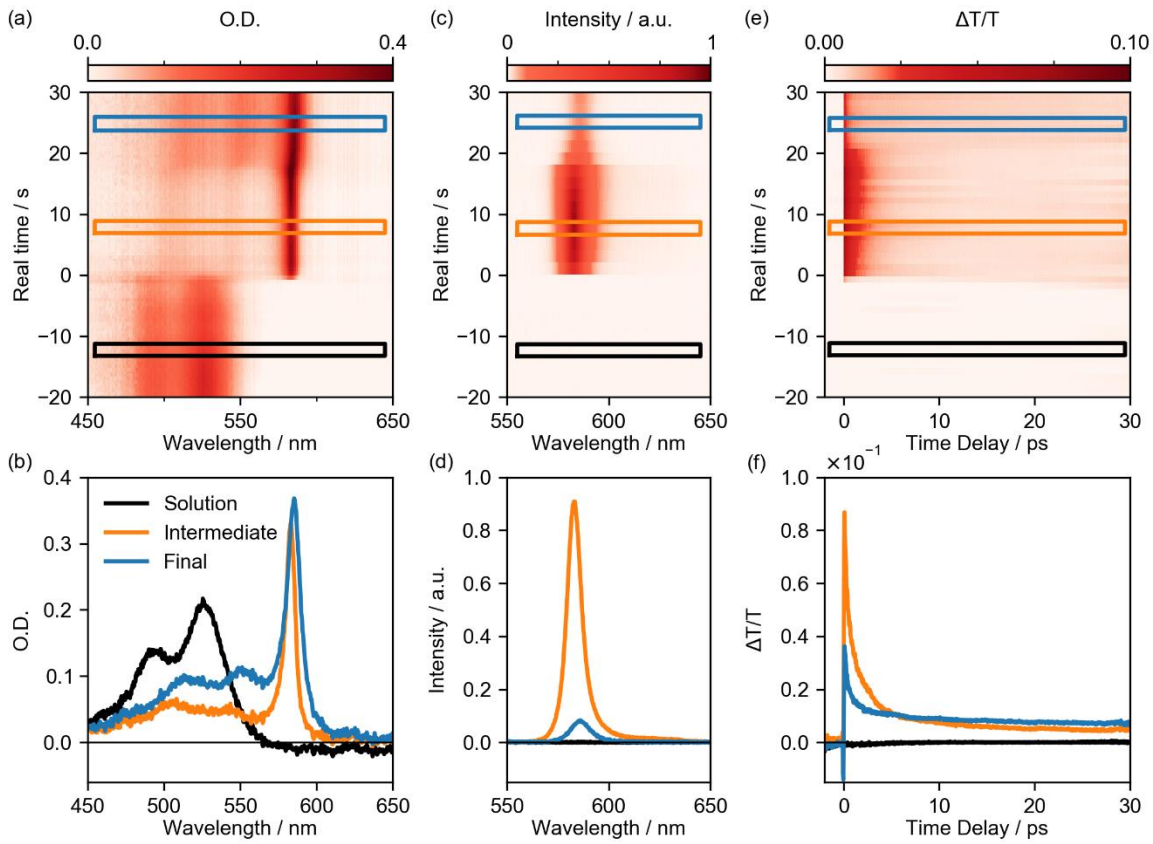

Fig. 4.4. In situ measurements of (a,b) absorption, (c,d) photoluminescence, and (e,f) SSTA during molecular aggregation into a film. (b) Absorption, (d) photoluminescence, and (f) SSTA measurements collected during the solution, intermediate, and final stages. Colored lines in (a,c,e) indicate the real time of data in (b,d,f). The one-color SSTA measurements were performed using the laser spectrum shown in Fig. 4.1a centered at 583 nm. Reprinted with permission from ref. 6 © The American Chemical Society.

stage, but both signals decay to the same magnitude by 10 ps. The TA signal collected during the intermediate stage can be fit using a bi-exponential function and a constant offset, $\Delta T/T = a_1 \exp(-t/\tau_1) + a_2 \exp(-t/\tau_2) + a_3$. This function cannot fit the TA signal collected during the film stage, and a tri-exponential must be employed, $\Delta T/T = a_1 \exp(-t/\tau_1) + a_2 \exp(-t/\tau_2) + a_3 \exp(-t/\tau_3)$. A rolling average of TA signal collected over 6 s was used for each fit. The shortest decay constant extracted from the fits of TA signal collected during the intermediate stage was statistically indistinguishable from that of the final stage, with an average of $\tau_1 = 0.31 \pm 0.06$ ps. Similarly, the second shortest time constant extracted from fits of both the intermediate and film stages are similar, with an

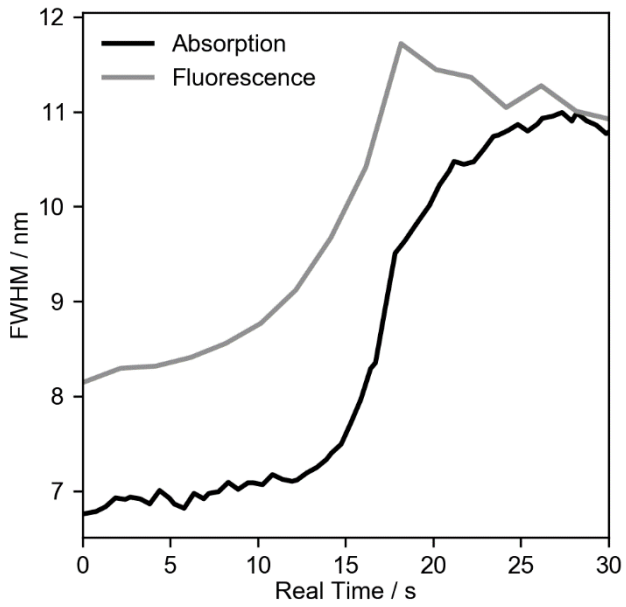

Fig. 4.5. Full width at half maximum (FWHM) of the J-aggregate absorbance and photoluminescence features measured in situ during the intermediate and final stages. Reprinted with permission from ref. 6 © The American Chemical Society.

average of τ_2 = 2.55 ± 0.53 ps. Since these two time constants remain the same as the sample evolves from the intermediate stage to the film stage, it is likely that the fast physical processes that result in these two exponential signal decays do not change. This is not the case for the longer physical processes. While the long-lived TA signal collected during the intermediate stage is well fit by a constant offset, a third exponential function must be used to fit the signal collected during the film stage, with a time constant of τ_3 = 96.7 ± 16.0 ps. This change indicates the emergence of a new, faster, physical process to return excitons to the ground state when the sample transitions from the intermediate stage to the film stage. The decrease in photoluminescence intensity suggests that this faster process is non-radiative, and out-competes the radiative process that is more prevalent during the intermediate stage. The evolution of the corresponding amplitudes for each of the time constants in the fits is shown in Fig. 4.6. The transition from the intermediate to the final stage is apparent at ~20 s. The contribution of the two faster

exponential decays to the overall SSTA transient signal decreases as the sample transitions from the intermediate stage to the film, while the amplitude of the long-lived component increases. It is notable that these dramatic changes in the photoluminescence intensity and the exciton dynamics are not matched by a dramatic change in the absorption lineshape. The redshift of the three distinct peaks in the absorption spectrum and the change in their peak intensity ratios upon transition from the intermediate stage to the film stage are quite subtle by comparison, shown in Fig. 4.7. The increased linewidth of the J-aggregate absorption and photoluminescence peaks upon transition to the film stage, shown in Fig. 4.5, suggests that the aggregates in the film are more disordered, potentially as a result of the vaporization of the last shell of solvent around the aggregates. Without a solvent shell, the aggregates will physically contact each other, potentially disrupting individual aggregate structures. This may introduce a fast quenching pathway and reduce the number of aggregates that fluoresce. This picture agrees with the measurements of Sorokin et al., who report that topological disorder and exciton-phonon coupling result in exciton self-trapping in films of PIC, observed as an increase in non-radiative relaxation and decrease in the luminescence quantum yield.[109] Photoluminescence measurements of PIC aggregates in solution by Cooper also support this picture.[110] The photoluminescence band was observed to split into two peaks at cryogenic temperatures. Fidder later supported Cooper's findings and found that the two aggregate structures with different photoluminescence yields can coexist within the same aggregate chain.[111] This suggests that multiple aggregate structures may be able to form and coexist when the aggregates contact each other as the final solvent shell is removed. The absorption and photoluminescence peak positions and intensities will be different for

each aggregate structure owing to the sensitivity of electronic structure to the precise arrangement of molecules. As the final solvation shell is stripped from the aggregates during the transition of our films from the intermediate state to the final state, it is possible that multiple aggregate structures are formed, resulting in spectral features that are broader and slightly shifted. A deeper analysis of the mechanism of photoluminescence quenching is currently being pursued. Further experiments using in situ grazing incidence wide-angle x-ray scattering during film formation could help distinguish structural difference between the intermediate and final film structures.[112,113]

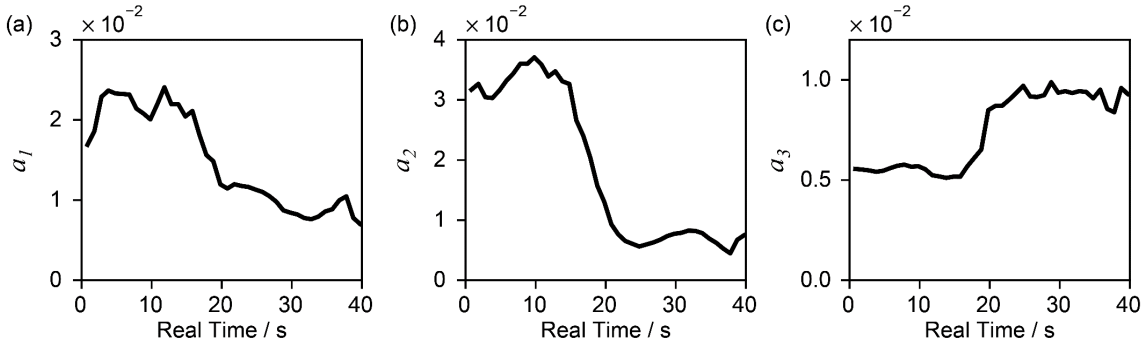

Fig. 4.6. Amplitudes of the three exponentials used to fit the transients collected in situ during the intermediate and final stages. Reprinted with permission from ref. 6 © The American Chemical Society.

Conclusion

For the first time, exciton dynamics has been revealed during thin-film formation by translating the thin film during SSTA measurements to average over heterogeneity. Future studies will explore the impact of heterogeneity on SSTA measurements and develop methods for detecting and filtering out severe heterogeneity. We reveal an intermediate stage during the film formation process that persists for approximately 20 s. The exciton dynamics during this stage of aggregation cannot be probed without SSTA. These data, in conjunction with in situ absorption and photoluminescence, provide insight into the electronic structure and exciton dynamics of materials that are not at structural

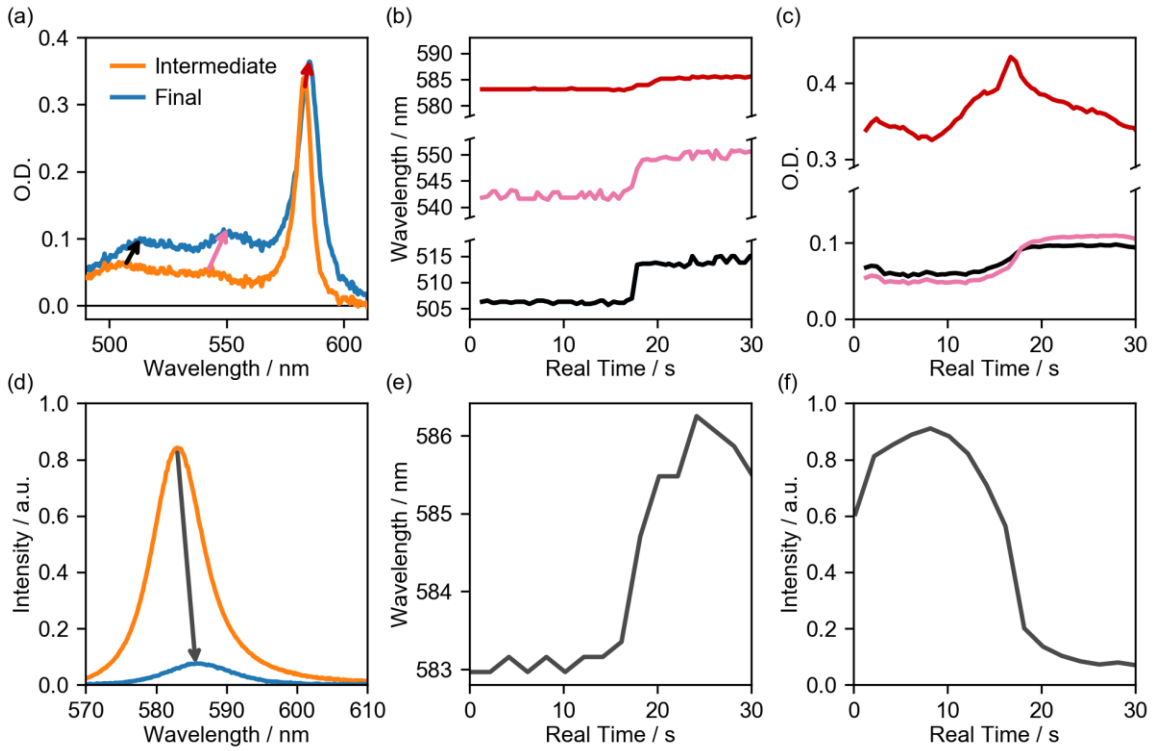

Fig. 4.7. (a) Absorbance spectra measured in situ during film formation. (b) The redshift upon transition from intermediate to final film is subtle for the J-band (top) in comparison to the higher energy absorption peaks (middle, bottom). (c) Optical density of the absorption peaks as a function of time during deposition. The relative intensity of the two higher energy absorption peaks invert during the transition from intermediate to final film. (d) photoluminescence spectra measured in situ during film formation. Upon formation of the final film, the photoluminescence feature redshifts slightly (e) and significantly decreases in intensity (f). Reprinted with permission from ref. 6 © The American Chemical Society.

equilibrium. The ability to measure properties that directly determine material functionality in situ during materials formation will provide valuable feedback for the rational design of functional excitonic materials. Understanding the evolution of exciton dynamics during the formation of organic molecular aggregates, the self-assembly of arrays of nanocrystals, or during chemical reactions will provide insight into how materials with a particular photophysics can be kinetically trapped.

Evolving Stark Effect of Perovskite Nanocrystal during Growth via Transient Absorption

Background

Lead halide perovskites have been investigated extensively as suitable materials for both light harvesting and light emitting devices.[114–117] Lead halide perovskite nanocrystals (NCs) are particularly appealing for light emitting devices due to their spectral tunability by varying the composition and size of the NCs.[118] The quality of the NC surface plays a significant role in the spectral characteristics and stability as the surface-to-volume ratio is large.[119–123] NCs are grown in solution with organic capping ligands that passivate and stabilize the surface. When the surface is poorly capped, localized energy states that reside in the bandgap of the material create trap states for excited species. Evidence for poor surface quality can be observed with absorbance and photoluminescence measurements during NC growth. Using a solvation-mediated synthesis of methylammonium lead iodide NCs ($MAPBI_3$), Sadighian et al. observed two stages during growth as evidenced by distinct spectral features in both absorbance and photoluminescence spectra.[124] During the first stage, the spectral features redshift suggesting NC growth. The second stage exhibits a broadening of the photoluminescence feature but minimal spectral shift. To further understand each stage, they quenched the reaction at several points during the synthesis and monitored the aging and degradation of the NCs via absorption and photoluminescence measurements. At early times, the spectral signatures decayed quickly whereas at later times exhibited greater stability. They proposed that a final ligation stage occurs wherein the NCs become fully capped, improving the stability of the NCs. The actual nature of the surface states cannot be

observed using absorption or photoluminescence measurements. Typical TA measurements are incapable of measuring the excited state dynamics as the system evolves on a minute-by-minute basis. In order to overcome this limitation, SSTA measurements were performed on $MAPbI_3$ NCs during growth. SSTA measurements could reveal the presence and nature of surface states during NC growth to support evidence for a final ligation stage. This section demonstrates that SSTA can be used to study and interpret the surface quality of $MAPbI_3$ NCs during growth.

Methods

MAPbI perovskite nanocrystals are synthesized using a previously reported solvation limited synthesis.[124,125] 460 mg PbI_2 and 127 mg of MAI are mixed in 40 mL of hexane. The solution is placed in a glass test tube. The tube is suspended in a sonicating bath which is used to mix the reaction. The temperature of the sonicating bath is stabilized by aluminum plates connected to a circulating bath set to 22 °C. 150 μL octylamine and 300 μL oleic acid are added to the solution. PbI_2 and MAI are insoluble in hexane and octylamine and oleic acid solubilize the precursors to initiate the reaction. Aliquots from the reaction are removed every 5 minutes for 60 minutes and every 10 minutes from 60 to 120 minutes. Each aliquot is filtered through a PTFE syringe filter (VWR) with a 0.45 μm pore size during the first 15 minutes. After 15 minutes a 1.0 μm PTFE pre-filter (Whatman Rezist) was used to filter out larger particulates. After 60 minutes, a 5.0 μm filter (Whatman Rezist) was added as well. The aliquots were placed into a quartz cuvette (Starna Cells, 48-Q-0.2) with a 0.2 mm pathlength. Absorption and photoluminescence measurements are performed on a homebuilt setup and collected before and after SSTA measurements. For absorption, a broadband light source

(Thorlabs, SLS201) is transmitted through an optical fiber (Thorlabs, M28L01) and focused onto the sample. After the sample a second lens focuses the light into a second optical fiber which directs the light to a spectrometer (Ocean Optics, Flame-T). photoluminescence measurements are performed using a 400 nm excitation laser (Thorlabs, CPS405. An optical fiber (Thorlabs, M95L01) positioned near the excitation spot directs the light into a spectrometer (Ocean Optics, Flame-T). Immediately after these measurements the sample is placed at the sample position of the SSTA setup. The SSTA setup is described in Chapter 2. SSTA measurements are performed for 60 seconds using a pump beam centered at 520 nm and a broadband probe beam. The spectral window collected by the CMOS detector is 540 nm to 635 nm. The pump profile is calibrated using SSTA measurements of cresyl violet.

Results and Discussion

The evolving electronic structure is evident in the absorption and photoluminescence spectra collected during NC growth, Fig. 4.8. Immediate growth of a broad, featureless photoluminescence peak centered at 595 nm and an absorbance peak centered at 525 nm are evidence for early stages of nucleation. photoluminescence increases and distinct spectral features are observed. At 30 minutes an absorption band at 575 nm reaches a peak intensity before fading away and giving rise to a new broader shoulder at 610 nm. The photoluminescence continues to increase with a broad peak at 635 nm dominating the spectrum. These are in agreement with previous reports.[124,125]

SSTA measurements at different time points during NC growth are shown in Fig. 4.9. A shift in the transient spectra within the first 500 fs has been attributed to carrier cooling.[126] After this initial shift, very little decay and no spectral change is observed

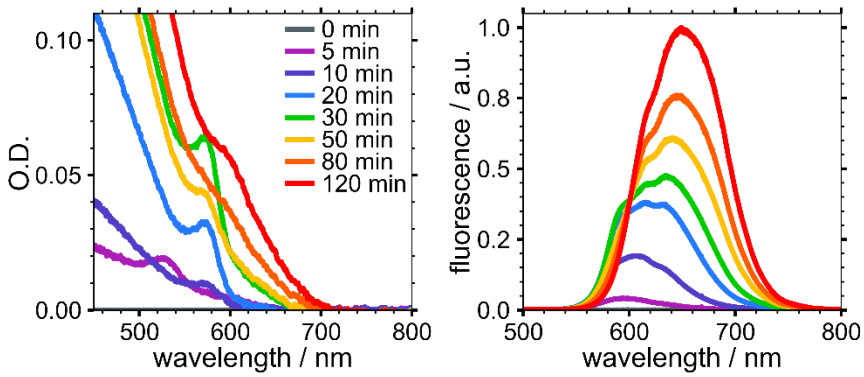

Fig. 4.8. Absorption and photoluminescence spectra of MAPbI perovskite NCs at different time points during growth. Reprinted with permission from ref. 2 by the authors.

across the 60-ps time delay window. A comparison of the fully grown NC transient spectrum in Fig. 4.9d agrees with previously reported results.[127] A negative feature observed in the intermediate stages at 20 and 30 minutes is centered at 582 nm does not coincide with any spectral features in the absorption or photoluminescence spectra from the same time points suggesting that neither ground state bleaching nor stimulated emission can explain this signal.

Conclusion

An explanation of the observed transient spectral features was found by my colleagues and published in ref. 44. They propose that these results report on the surface quality during NC growth and reveal increased ligation of the NCs in the final stages of growth. These measurements could not be performed without SSTA and are the first to demonstrate the capability of SSTA to study the evolving excited state dynamics of perovskite NCs during growth. Future work will employ this technique to further elucidate the nature of the intermediate NC excited state properties.

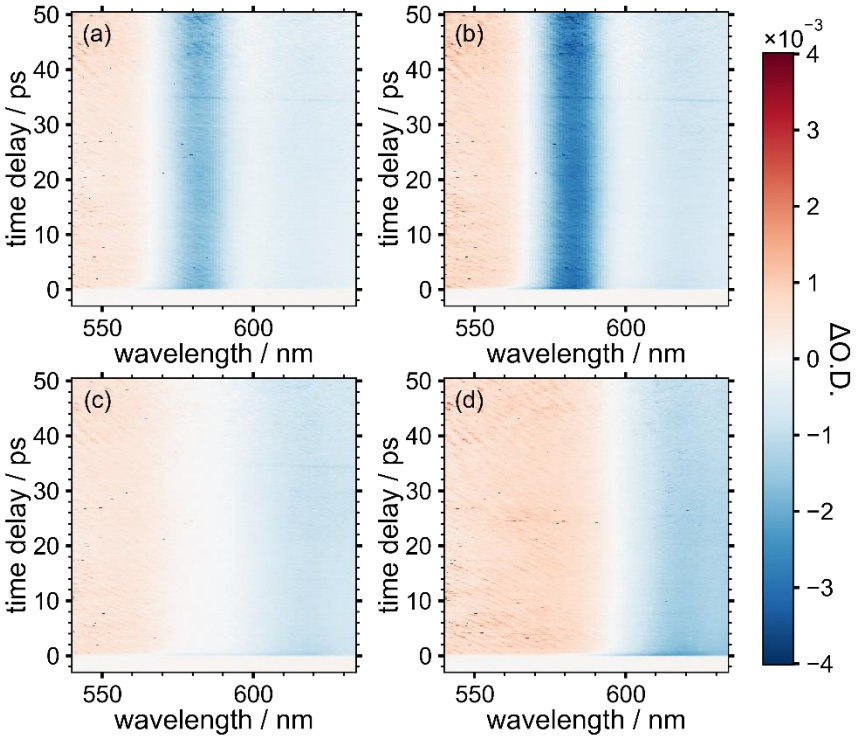

Fig. 4.9. SSTA measurements of MAPbI NC aliquots measured after (a) 20 min, (b) 30 min, (c) 50 min, and (d) 120 min after starting the reaction. Reprinted with permission from ref. 2 by the authors.

SSTA and Absorption Measurements of Electron Donor:Acceptor Systems

Background

Excited state dynamics of electron donor:acceptor (DA) systems determines the utility of such systems in photovoltaic devices. Organic photovoltaics are of particular interest as a cost-effective alternative to silicon solar cells with cheaper material and fabrication costs with the potential for solution processed deposition techniques.[128] Solution processing and other post-deposition techniques such as vapor or thermal annealing have been shown to improve solar cell efficiency. SSTA measurements can be used to monitor the excited state dynamics of a DA system during deposition and post-processing techniques. We have studied two model DA systems to investigate the evolving excited state dynamics during solution deposition and thermal annealing. In both cases we use phenyl-C61-butyric acid methyl ester (PCBM) as an electron acceptor.

Layered films of copper phthalocyanine (CuPc), an electron donor, with PCBM were investigated. Bulk heterojunction (BHJ) films of P3HT and PCBM were also investigated. Work presented herein is preliminary to in situ SSTA measurements during thin film depositions of CuPc and PCBM and during thermal annealing of P3HT and PCBM blended films.

CuPc is a common organic dye that forms fibrous chains when deposited as shown in Fig. 4.10.[129] It is insoluble in most common solvents making it an ideal candidate for layered DA deposition studies.[130] PCBM has been shown in previous studies of BHJ polymer PCBM blended films to intercalate between side chains of the polymer aggregates.[131,132] The ability of PCBM to intercalate well with the fibrous CuPc chains should be affected by the order of deposition. Our studies focus on the effect of deposition order on charge transfer between the donor and acceptor.

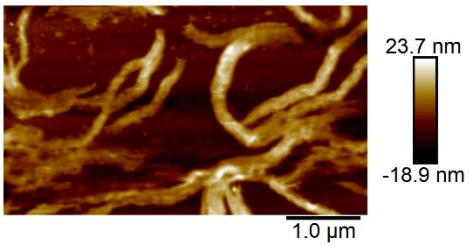

Fig. 4.10. Atomic force microscopy images of a CuPc film.

P3HT is a well-studied model polymer that forms a crystalline structure upon aggregation.[133] When deposited jointly with PCBM into a BHJ film, PCBM disrupts the crystalline aggregation pathway and results in a more amorphous structure.[134] However, upon thermal annealing the P3HT forms more crystalline domains and forces PCBM to the edges of these domains.[134–138] This results in an increase in power conversion efficiency from 0.79% to 3.15%.[139] Transient measurements by Marsh and coworkers demonstrated that upon thermal annealing that while the charge transfer rate decreases

upon thermal annealing by more fully separating the P3HT and PCBM regions, the rate of charge recombination significantly decreases as well, increasing the overall efficiency in the device.[46] We repeat Marsh's experimental procedure to set a baseline in preparation to measure the excited state dynamics during thermal annealing.

Herein we report preliminary transient spectra acquired for each of these two systems. Atomic force microscopy measurements of CuPc and PCBM are also presented. These results will give insight into what will be observed when SSTA measurements are performed.

Methods

Layered CuPc and PCBM films are desposited using a combination of dropcast and spincast techniques. A glass slide was cleaned using methanol. CuPc is dissolved in trifluoroacetic acid (TFA) at a concentration of 0.17 mg/mL. PCBM is dissolved in chloroform at a concentration of 1.5 mg/mL and 15 mg/mL for dropcasting and spincasting, respectively. Spincasting is used when PCBM is deposited first. A slide is filled with solution on a spin coater and left to evaporate for 1-2 minutes before spinning. After this the slide is spun at 700 rpm for 15 seconds. For dropcasting, a slide at room temperature is filled with PCBM solution and covered with 1" headroom to slow evaporation and prevent air currents from disrupting the formation process. CuPc is dropcast onto a glass slide heated to 40 °C. The slide is covered with 1" headroom to slow evaporation.

Atomic force microscopy measurements were performed on a solution deposited CuPc film using a commercially available atomic force microscope (Bruker, Dimension Icon). Measurements were collected in tapping mode using an 8 nm tip with a spring

constant of 40 N/m and resonant frequency of 320 kHz. CuPc measurements are shown in Fig. 4.10.

Bulk heterojunction P3HT:PCBM films are deposited using dropcast solution deposition. P3HT and PCBM are dissolved in chlorobenzene with a 0.15 mg/mL concentration. The slide is heated to 40 °C and covered with 1" headroom during formation. Films are thermally annealed on a hotplate with a set temperature above 100 °C.

Absorption measurements were collected using a homebuilt setup. A broadband light source (Thorlabs, MWWHL3) was transmitted through an optical fiber and focused onto the sample. A second lens after the sample focused the beam onto an optical fiber connected to a USB spectrometer (Ocean Optics, Flame-T). TA measurements of CuPc and PCBM were collected on a homebuilt traditional TA setup with an excitation wavelength of 605 nm. TA measurements of neat P3HT and blended P3HT and PCBM films were collected using the instrument described in Chapter 2. The spectrograph was set to 500, 600, and 700 nm and the data from each spectrograph position were stitched together.

Results and Discussion

Absorption measurements of CuPc and PCBM films are shown in Fig. 4.11. Neat CuPc and PCBM spectra agree with literature spectra. A comparison between the absorption spectra of CuPc on PCBM (green) and PCBM on CuPc (purple) show different spectral features with a shoulder peak at 575 nm for PCBM on CuPc. The CuPc on PCBM absorption spectrum can be fit using a linear combination of the neat CuPc and neat PCBM spectra but the PCBM on CuPc spectrum cannot be accurately modeled with

a simple linear combination. This suggests that the deposition order can influence the electronic properties of the system.

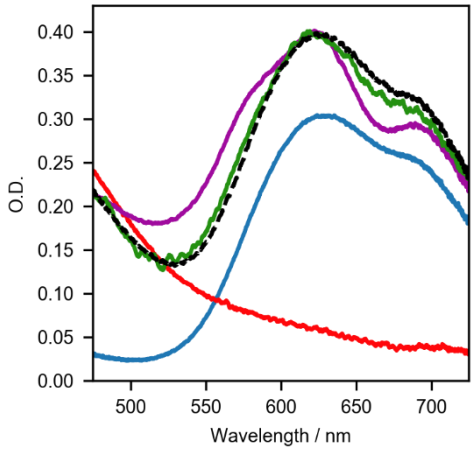

Fig. 4.11. Film absorption measurements of neat CuPc (blue), neat PCBM (red), CuPc on PCBM (green), PCBM on CuPc (purple), and a linear combination of neat CuPc and PCBM (black) spectra.

TA measurements of each of the four films is shown in Fig. 4.12. The spectral region at the pump excitation wavelength, 605 nm, masks signal impacted by pump scatter contributions. Neat CuPc and neat PCBM measurements are shown in Fig. 4.12a and 4.12b, respectively. PCBM does not have a resonant transition at 520 nm and does not have any significant signal across the spectral range. CuPc on PCBM (Fig. 4.12c) has the same spectral features as the neat CuPc TA signal (Fig. 4.12a) with broad excited state absorption and ground state bleach signals with a transition between them at 565 nm. PCBM on CuPc shows different spectral features with the transition from negative to positive at 550 nm and a loss of signal at 660 nm. While these features do not currently have an explanation, it demonstrates the impact deposition order has on the excited state features of the film.

Absorption measurements of P3HT and PCBM before and after annealing are shown in Fig. 4.13. Very little spectral change occurs due to annealing which agrees with

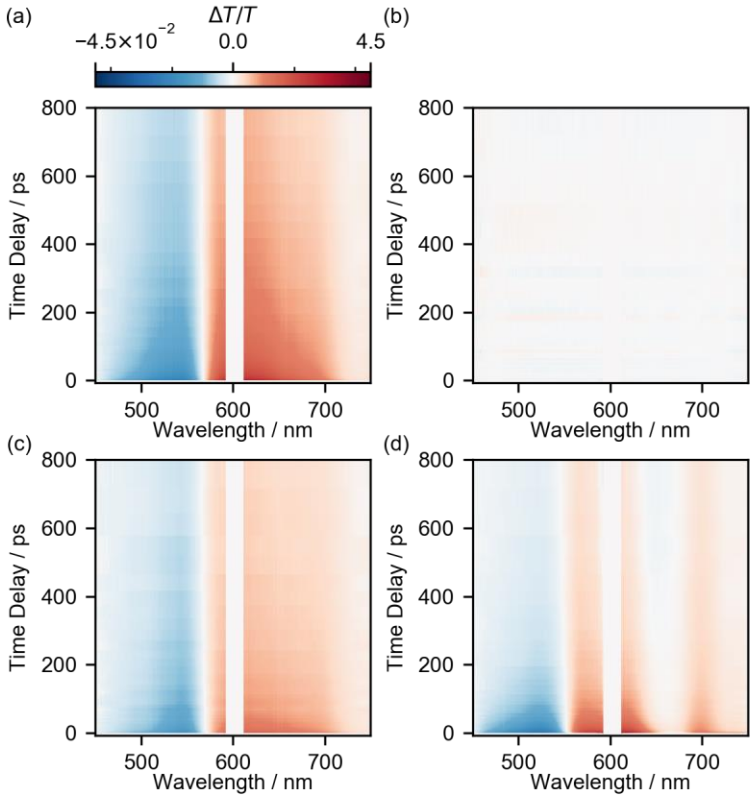

Fig. 4.12. TA measurements of neat CuPc (a), neat PCBM (b), CuPc on PCBM (c), and PCBM on CuPc (d) films. Pump excitation is centered at 605 nm and the spectral range from 592-612 nm is blocked to mask signal impacted by pump scatter.

the literature.[46] The impact of thermal annealing is more evident when comparing the transient measurements of the neat P3HT film with blended P3HT:PCBM films before and after annealing, as shown in Fig. 4.14. Disjointed continuities in the TA signal measured at 542 and 643 nm are artifacts caused by moving the spectrograph for each wavelength range but should not affect the brief analysis presented herein. For the neat P3HT film, three prominent ground state bleaching features are located at 520, 560, and 610 nm (Fig. 4.14a). A broad excited state absorption feature is observed above 645 nm. The relatively more intense spectral peak at 610 nm decays faster than the two other ground state bleach peaks. Marsh and coworkers attributed this to P3HT ordering.[46] The distinct features found in the neat P3HT signal are absent in the blended pre-annealed P3HT:PCBM film but upon thermal annealing become more prominent. This suggests

that annealing induces ordering of P3HT molecules in the film. The increase in excited state absorption observed above 630 nm in less than 1 ps suggests fast charge transfer from P3HT to PCBM. Upon thermal annealing, the charge transfer occurs over 30 ps, in agreement with previous reports.[46] It is notable that the dramatic changes in the transient signal accompany a subtle change in the absorption spectrum.

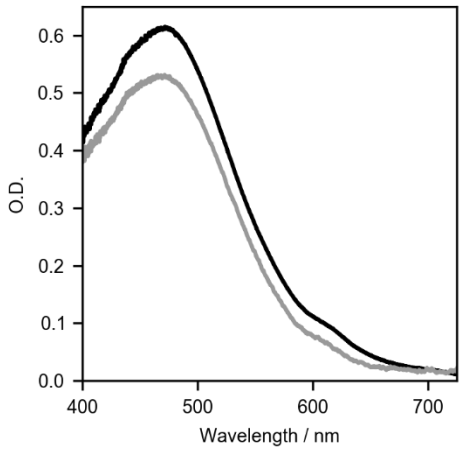

Fig. 4.13. Absorption of P3HT and PCBM BHJ film before annealing (grey) and after annealing (black).

Conclusion

TA measurements of organic donor:acceptor thin films can provide insight into the impact of physical ordering and structure on excited state dynamics. The deposition order of CuPc and PCBM impacts the excited state dynamics. Measurements of BHJ P3HT:PCBM films demonstrate the impact of thermal annealing of excited state dynamics. SSTA measurements for each of these systems will be performed in the future to study how the excited state dynamics evolves during layered solution deposition of CuPc and PCBM. The impact of deposition order on the excited state dynamics will also be further explored with supporting work using atomic force microscopy. In situ SSTA measurements will be performed during thermal annealing of P3HT:PCBM BHJ films to

study the evolving excited state dynamics. Further work will explore the temperature dependence of thermal annealing.

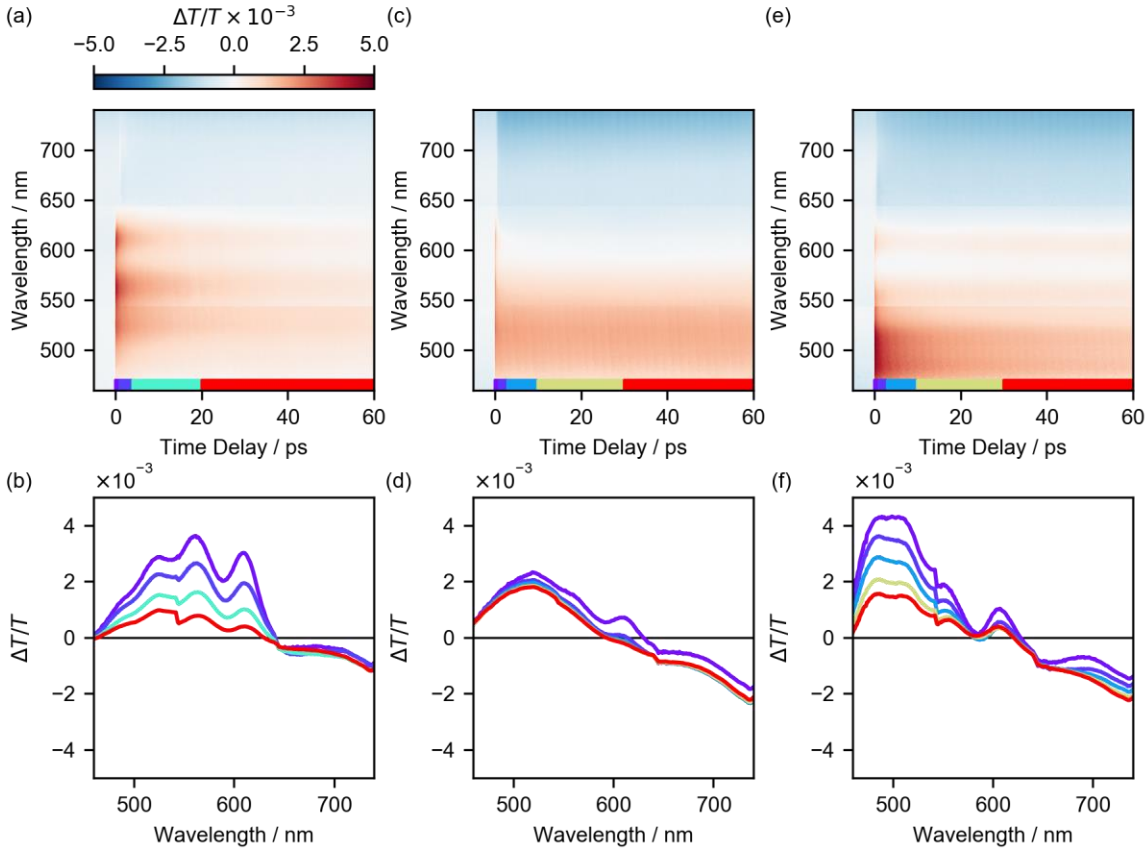

Fig. 4.14. TA measurements of neat P3HT (a,b), P3HT:PCBM before annealing (c,d), and P3HT:PCBM after annealing (e,f). (a), (c), and (e) show false color plots with a color legend at the base to show the time delay range averaged for each spectrum in (b), (d), and (f). The averaged time delay ranges for neat PIC are 0-1, 1-4, 4-20, and 20-60 ps. The averaged time delay ranges for P3HT:PCBM blended films are 0-1, 1-3, 3-10, 10-30, and 30-60 ps.

OUTLOOK

This dissertation has presented the design principles and applications of a state-of-the-art single-shot transient absorption spectrometer. Chapter 1 gives a brief introduction to transient absorption and its inability to collect the excited state dynamics of evolving or unstable systems. TA signal is collected by changing the pathlength, and consequently the time delay, between the pump and probe, which is typically accomplished by moving a retroreflector mounted onto a translation stage in the path of one of the beams. Each time delay position is collected until the SNR is sufficient, resulting in minutes to hours of data collection for a transient spectrum. Single-shot techniques have been developed to spatially encode the pump-probe time delay into a spatial axis of the probe beam, enabling the simultaneous acquisition of a range of time delays. This is accomplished through one of the following strategies: angled beam geometry, optical echelons, and pulse stretching. A study of design principles unique to SSTA was presented in Chapter 1 along with a comparison of strategies employed in different SSTA instruments reported in the literature to apply these principles.

Chapters 2-3 describe in detail a homebuilt broadband SSTA instrument with a spatially encoded 60 ps time delay range and a spectral range of 100 nm. This instrument exceeds the reported time delay range of all other SSTA instruments reported in the literature up to this point. This is accomplished through the use of a spatial light modulator, high energy white light generation, and unique calibration techniques. The SLM reshapes the pump and probe profiles to ensure uniform excitation by the pump with sufficient probe intensity across the time delay range. WLG in a homebuilt argon gas cell generates a broadband probe with sufficient energy for single-shot

measurements. Post collection calibration is performed for the time delay and wavelength axes of the acquired single-shot images. Correction for a non-uniform pump profile is also described.

Chapter 4 presents examples of different evolving systems where SSTA is well-suited to measure the accompanying excited state dynamics. In situ SSTA measurements during the molecular aggregation of PIC reveals an intermediate excited state with differing excited state dynamics from the same dye in solution or film. SSTA measurements during the growth of hybrid organic-inorganic perovskite NCs reveal intermediate excited state dynamics that indicate the surface quality of the NCs and can provide additional insight into the nature of the NCs during growth. Preliminary measurements of CuPc:PCBM and P3HT:PCBM thin films provide a future direction for SSTA measurement to study how charge transfer rates evolve during thin film deposition and thermal annealing. Each of the systems described in Chapter 4 demonstrate that the SSTA instrument can measure both solution and thin film samples.

Future work with this SSTA instrument will explore the relationship between intermediate excited state dynamics, electronic structure, and chemical structure of systems that evolve during solution deposition, NC growth, thermal annealing, or other processes. When coupled with other in situ techniques like absorption, photoluminescence, and x-ray scatter, SSTA will provide valuable feedback in the study and development of new materials and systems that could be used in photovoltaic or light emitting devices.

APPENDIX

SSTA ALIGNMENT PROCEDURES

General Techniques

Polaris Mirror Nobs

Polaris mirror mounts from Thorlabs consist of three knobs which control the vertical (V), horizontal (H) and diagonal (D) pointing of the mirror. For all two-mirror alignments, only V and H are used. D is designated as the "forbidden" nob. For all one-mirror alignments, all three nobs are used.

Alignment Rules

1. Remove any reflective jewelry or watches whenever your hands are on the table.
2. Always use a beam block after your second iris to contain the beam. This will prevent the beam from reflecting unexpectedly later in the path. Failure to do so could result in injury or damage to optics.
3. Always use small adjustments to ensure that your beam is contained and safe.
4. For periscopes or high-power beams, use appropriate laser goggles.
5. While aligning new mirror setups, ensure that all optics are secure and that you follow the beam with a beam block to contain it.
6. Make sure you are using the correct pair of irises for the path that you are aligning.

Two-Mirror Alignment

Two-mirror alignment is for aligning a beam straight between two irises using two mirrors (Fig. A.1). Do not use D; it is forbidden! You do not need 3-nobs for this alignment.

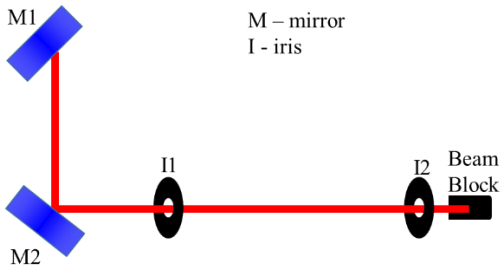

Fig. A.1. Two-mirror alignment optics configuration. M1 and M2 are used to align the beam through I1, and I2, respectively.

1. Always set up a beam block after your second iris.
2. Ensure I1 does not clip the beam. Close I2 so that a halo of the beam appears around the opening (see Fig. A.2).
3. Use V and H on M2 to align the beam onto the center of the I2. You can adjust the opening size of I2 and look at the beam on the beam block to help you judge how well centered you are.
4. Close I1 until you see a halo. Use V and H on M1 to align to I1.
5. Repeat steps 2-4 until the beam is centered on both I1 and I2.

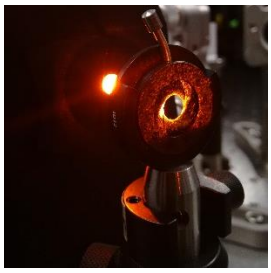

Fig. A.2. Halo of beam on iris.

One-Mirror Alignment

One-mirror alignment is for aligning a beam straight between two irises using one mirror (Fig. A.3). The mirror must have 3 nobs. The beam must be aligned straight going into this mirror. The goal of the D nob is to change where on the mirror the incoming beam is hitting and adjusting that to straighten out the beam.

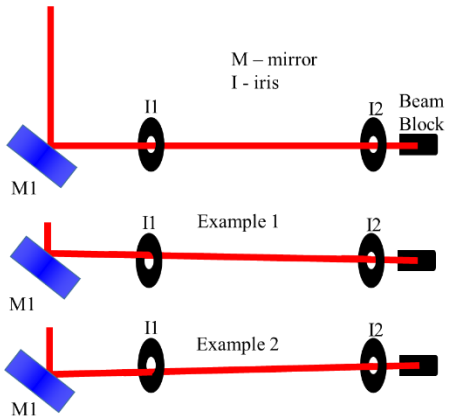

Fig. A.3. One-mirror alignment optics configuration with off-alignment examples. H and V knobs on M1 are used to align the beam to I2. D on M1 is used to align the beam to I1.

1. Use H and V to align M1 to I2.
2. Check I1 to see which side of the iris is clipping the beam. If clipping, see two cases below.
3. Example 1: turn D counterclockwise no more than a half turn, pulling the mirror back and causing the beam to hit the mirror closer to the axis through the irises.*
4. Example 2: turn D clockwise no more than a half turn, pushing the mirror forward and causing the beam to hit the mirror closer to the axis through the irises.*
5. Repeat steps 1-4 until the beam is centered on both I1 and I2.

*Note! Do not attempt to use D to align the beam to I1; it will not work.

Stage 1

Fig. A.4 shows the general alignment procedures for the pump and probe beams through Stage 1 of the setup. It is assumed that the 800 nm is already well aligned into the optical parametric amplifier (OPA).

Pump

The OPA converts the 800 nm beam to another wavelength in the spectrum. This line is the pump beam (black). In Stage 1 the pump is resized using a convex and concave mirror setup. A periscope lowers the pump height for the prism compressor. The pump is compressed in the prism compressor. The alignment procedures inside the prism

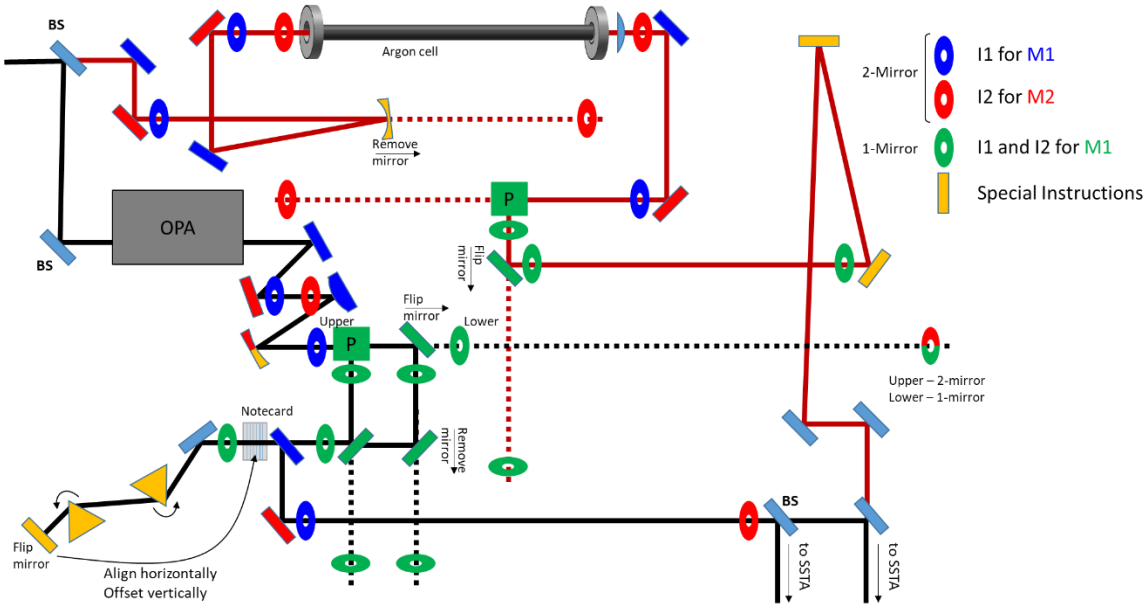

Fig. A.4. Stage 1 alignment procedures. The pump path (black) and probe path (red) are shown. Mirror colors correspond to 1-mirror (green) and 2-mirror (blue and red) alignment procedures. Special instructions are marked with orange. Pale blue optics are rarely adjusted or not described in this section. BS, beam splitter; OPA, optical parametric amplifier; P, periscope.

compressor are described but not the process for compression. The beam is sent to the single-shot transient absorption (SSTA) setup. The following irises are used for alignment:

1. “OPA Tall” or “OPA short” irises (OPA)
2. Periscope irises (PER)
3. “Before prism” (BP)
4. “After prism” (AP)

The pair of OPA irises to use are based on the exit-port used by the OPA. This is determined by the wavelength of light generated by the OPA. The periscope irises are an iris mounted on an optics tube for I1 and a screw centered in a spacer for I2. Before prism irises are shared by both the SSTA and traditional TA setups. Each setup has its own pair of AP irises.

Exiting the OPA. OPA irises are used. Two-mirror alignment procedures are used. Fig. A.5 shows optics layout. There are no special instructions.

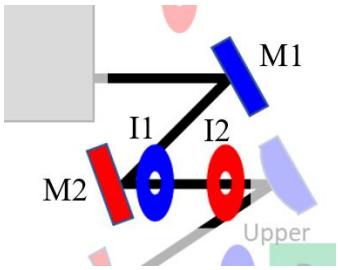

Fig. A.5. Alignment exiting the OPA. M1 and M2 align the beam through I1 and I2, respectively.

Resizing the Beam. OPA irises are used. Two-mirror alignment procedures are used. Fig. A.6 shows optics layout. M1 (blue) is a 750 convex mirror, M2 (red/yellow) is a 1000 mm concave mirror. M2 is secured in an XY-translation mount which is used to center the beam from M1 onto M2. M2 is also mounted on a translation stage.

The upper mirror of the periscope must be flipped out of the beam path for alignment. The beam must be collimated before alignment. Collimation is performed by putting a removable mirror between I1 and I2 and sending the beam across the room. The translation stage position of M2 is adjusted until the apparent size of the beam across the room matches the size of the beam after M2. Once collimated, the standard 2-mirror alignment procedure is used.

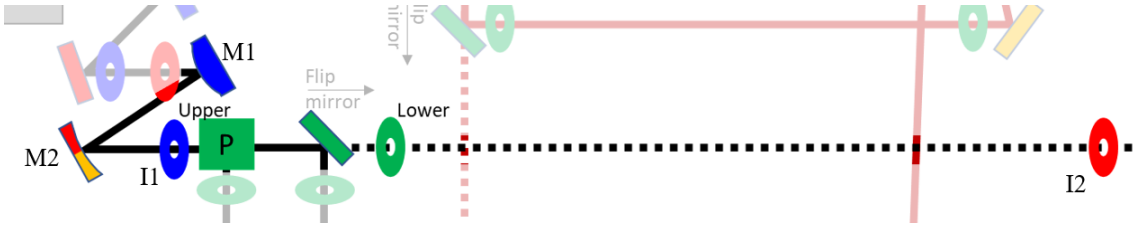

Fig. A.6. Alignment resizing the pump beam. Upper periscope mirror (P) is flipped out of the path. M1 and M2 align the beam through I1 and I2, respectively.

Periscope Part 1. PER irises are used. One-mirror alignment procedures with special instructions are used. Fig. A.7 shows optics layout. The lower periscope mirror

mounted on a magnetic baseplate is removed. WARNING: WEAR APPROPRIATE LASER GOGGLES DURING VERTICAL ALIGNMENT. A screw and post spacer (Thorlabs part RS5M) are screwed into the laser table. The screw serves as I2. If possible, use an anodized screw for this. I1 is a tube-mounted iris. The tube has a side viewing window. It fits over the post spacer. Follow the 1-mirror alignment procedures.

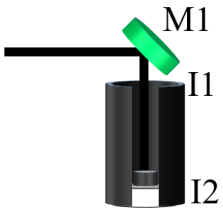

Fig. A.7. Alignment down periscope. A screw and spacer are mounted on the table. The center of the screw head is I2. An iris (I1) and optical tube are fit around the spacer. M1 aligns beam through I1 onto I2.

Periscope Part 2. BP irises are used. One-mirror alignment procedures with special instructions are used. Fig. A.8 shows optics layout. Fig. A.9 shows periscope mirror orientation for horizontal-to-horizontal and vertical-to-horizontal polarization changes. The upper mirror of the periscope is mounted on a translation stage. The lower mirror is mounted on a magnetic mount. When the polarization from the OPA is horizontal, the lower mirror sends the beam in the same direction as it entered the periscope. When the polarization from the OPA is vertical, the lower mirror turns the beam 90° towards the prism compressor.

Fig. A.8. Horizontal-to-horizontal polarization alignment out of periscope (P). M2 is flipped out of the path. The lower periscope mirror (M1) aligns the beam through I1 and I2.

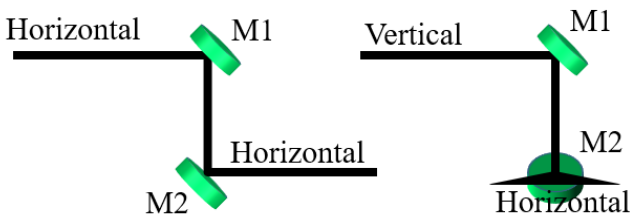

Fig. A.9. Horizontal-to-horizontal (left) and vertical-to-horizontal (right) polarization periscope mirror orientation. M1 is flipped out of the path for section Periscope Part 1. M2 is removed for vertical alignment in the periscope.

Horizontal polarization methods are described here. The first mirror after the periscope is flipped down, M2 in Fig. A.8. One-mirror alignment procedures are used with the D knob correcting for the vertical axis on I1. The translation stage for the upper mirror of the periscope may also be used for correcting the vertical axis on I1.

Vertical-to-horizontal polarization optics layout is shown in Fig. A. 10. The beam splitter going into the traditional TA prism compressor line is NOT removed. The mirror going into the second prism compressor is removed. One-mirror alignment procedures are used with the D knob correcting for the vertical axis on I1. The translation stage for the upper mirror of the periscope may be used for correcting the horizontal axis on I1. After this alignment and before the alignment into the SSTA prism compressor, align into the traditional TA prism compressor. The instructions for aligning into the traditional TA prism compressor are the same for aligning into the SSTA prism compressor described below.

Line Before Prism Compressor. BP irises are used. One-mirror alignment procedures are used. Fig. A.10 shows optics layout (Horizontal). This alignment is only used for horizontal polarization from the OPA. The beam splitter going into the first prism compressor line is NOT removed. The mirror going into the second prism compressor is removed. After this alignment and before the alignment into the SSTA

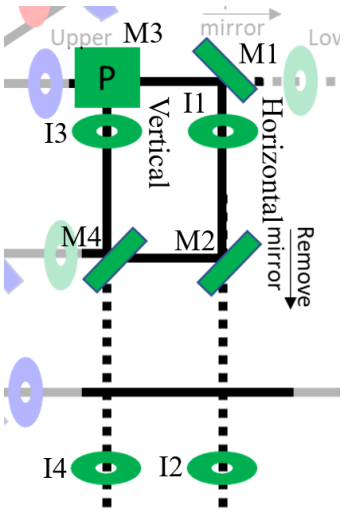

Fig. A.10. Alignment after periscope (P). Horizontal-to-horizontal alignment: Remove M2; M1 aligns the beam through I1 and I2. Vertical-to-horizontal alignment: Remove M4; M3 (lower mirror of P) aligns beam through I3 and I4.

prism compressor, align into the traditional TA prism compressor. The instructions for aligning into the traditional TA are the same for aligning into the SSTA prism compressor described next.

Into the Prism Compressor. BP irises are used. One-mirror alignment procedures are used. Fig. A.11 shows optics layout. M1 will be in mounted on the right (left) for horizontal-to-horizontal (vertical-to-horizontal) polarization configuration.

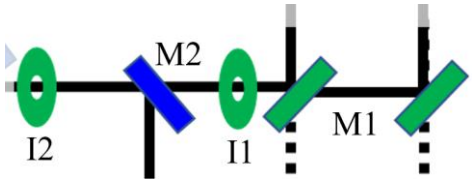

Fig. A.11. Alignment into the prism compressor. M1 is vertical-to-horizontal (left) or horizontal-to-horizontal (right) alignment. M1 aligns beam through I1 and I2 over the top of M2.

Prism Compressor. No irises are used. Special alignment instructions are used. Fig. A.12 shows optics layout. The entrance mirror going into the prism compressor (light blue) is not adjusted. Unless the wavelength has changed (from the OPA) and/or the beam needs to be recompressed, the prisms do not need to be adjusted. The back-

reflecting mirror is adjusted so that the outgoing beam sits directly beneath the incoming beam before the entrance mirror. This is typically done using a notecard. Position the notecard so it clips the bottom of the incoming beam and catches the top of the outgoing beam. Use the H knob of the back-reflecting mirror to align the two beams horizontally. Vertical alignment is adjusted using the V knob of the back-reflecting mirror such that the beam does not clip at the top of M2.

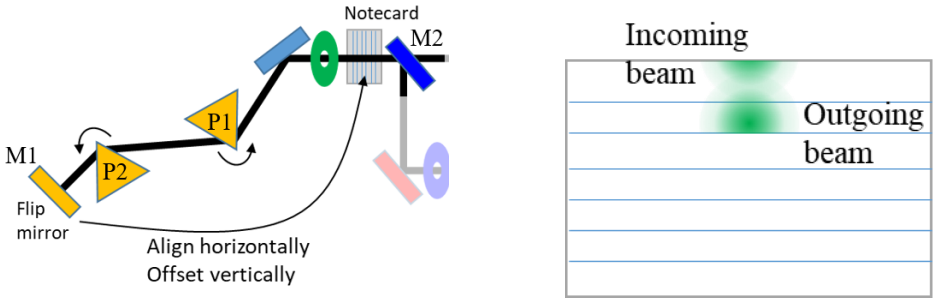

Fig. A.12. Alignment through prism (P1, P2) compressor (left) and back reflection image on notecard (right). M1 aligns beam back through P1 and P2 onto a notecard. Outgoing beam should align directly beneath the incoming beam. M1 is adjusted to avoid clipping the beam on the top of M2.

The prisms (P1, P2) must be oriented at the Brewster angle to the incident light. P2 is mounted on a rotation stage and translation stage. The back-reflecting mirror is mounted on a flipper mount. The Brewster angle is found by adjusting the angle of the prism to minimize the angle of deviation from the unaltered beam path, Fig. A.13. For P1, move P2 out of the beam path using the translation stage. The beam should be able to reach the Astrella box. For P2, flip the back-reflecting mirror out of the way and send the beam across the room. WARNING: ALERT OTHERS IN THE ROOM, PUT UP A BEAM BLOCK (a rolling chair works well).

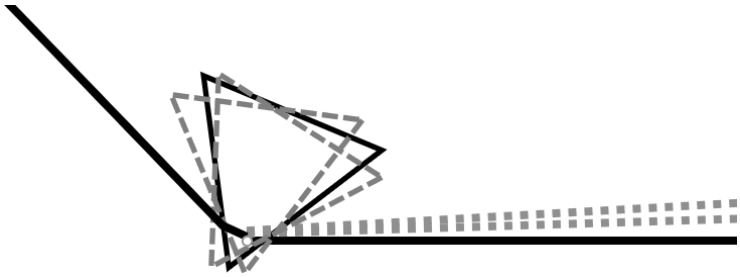

Fig. A.13. Prism alignment for Brewster angle. The incoming beam (left) is diffracted through the prism. At the Brewster angle the refractive angle is minimized (black). Other prism angle yield larger refractive angles (dotted).

Single-color wavelength resolved SSTA measurements of a simple dye are used as a reference for the compression. Compression is coarsely controlled by adjusting the distance between P1 and P2. Compression is fine controlled by adjusting the translation stage position of P2. When moving P2, ensure that P2 points along the direction of translation for the stage. Position the translation stage to the middle of its range. If the beam clips off the edge of the prism, move P2 further from P1. If the beam clips off the base of the prism, move P2 closer to P1. Ensure that the P2 is at the Brewster angle after each movement.

To Stage 2. AP irises are used. Two-mirror alignment procedures are used. Fig. A.14 shows optics layout. If the beam hits M1 too high and starts clipping, adjust the vertical pointing of the back-reflecting mirror in the prism compressor. The back-reflecting mirror can also be used if the V knob of M1 reaches the end of the threads.

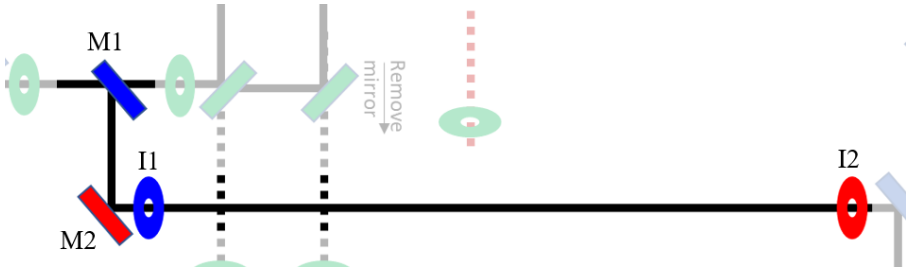

Fig. A.14. Alignment to the SSTA setup. Mirrors 1 (blue) and 2 (red) align to irises 1 (blue) and 2 (red), respectively.

Probe

The 800 nm beam is converted to a supercontinuum beam using white light generation (WLG) in an argon gas cell. The argon cell is ~1.6 m long with sapphire windows at each end. The cell is evacuated using a vacuum pump. The vacuum pump is located in the galley but is connected to a valve located over the traditional TA camera. A tube connects the cell to the vacuum tube. The argon gas cylinder is located next to the optics cabinet. The tube is pressurized to 0.95 bar above atmospheric pressure. The beam is focused into the cell using a 2-m focal length mirror. After collimation, the beam travels through a periscope to be at the same height as the pump after the prism compressor. The polarization is changed from horizontal to vertical (to accommodate the spatial light modulator) using a periscope. The broadband probe intersects with the single-color probe path as shown in Fig. A.4. The following irises are used for alignment:

1. "Argon Tall" (ARG)
2. WLG attenuating iris (ATT)
3. Periscope irises (PER)
4. "After Prism" (AP)

ARG is used from outside the Astrella to the periscope. ATT attenuates the 800 nm beam going into the argon cell. AP is the same set of irises used for the pump after the prism compressor.

Into Focusing Mirror. ARG irises are used. Two-mirror alignment procedures are used. Fig. A.15 shows optics layout. The 2-m focal length mirror is mounted on a magnetic baseplate and is removed for alignment.

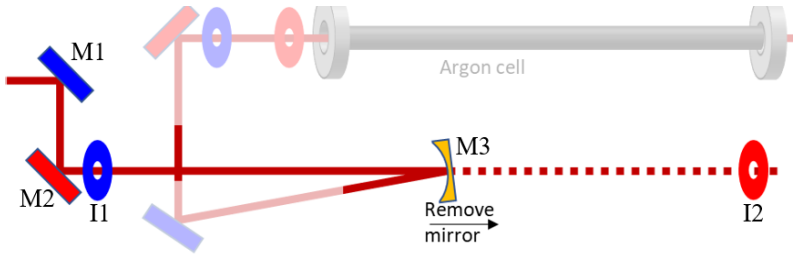

Fig. A.15. Alignment into focusing mirror. M3 is removed. M1 and M2 align the beam through I1 and I2, respectively.

Focusing Mirror. No irises are used. Special alignment instructions are used. Fig. A.16 shows optics layout. The pointing of the focusing mirror is adjusted such that the beam hits approximately the center of M2.

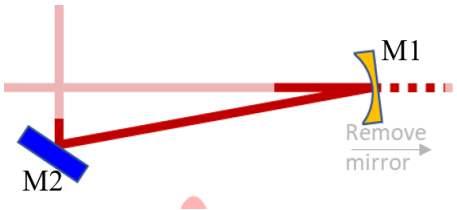

Fig. A.16. Alignment from concave mirror. M1 aligns the beam to the center of M2.

Argon Cell and WLG. ARG irises are used. Two-mirror alignment procedures with special instructions are used. Fig. A.17 shows optics layout. WARNING! PLACE A BEAM BLOCK BEFORE THE CELL WHILE ALIGNING. FAILURE TO DO SO WILL BURN CELL WINDOWS! Alignment through the cell can be challenging. To pre-align through the tube, place both I1 and I2 before the tube. Follow the 2-mirror alignment procedures. Once aligned, place ATT in the place of I2. Adjust the height so that the beam passes through the center of the iris. Place I2 after the cell. Close down ATT completely and let the beam through the cell. If round, small beam exits the cell, then use M2 to align to I2. If no light or scattered light exit the cell, using small adjustments repoint the beam using M2 until it can be seen exiting the cell. If it cannot be found. Replace I2 before the cell and realign. Repeat the process. Slowly open ATT until the beam begins to change color (usually an orange red). Adjust the alignment through I2

using M2 again. Open the iris until WLG occurs. Increase the ATT aperture size just past the point of WLG where no flickering occurs. It should have a blueish hue to it. DO NOT OPEN ATT TOO FAR; IT WILL DAMAGE THE WINDOWS OF THE ARGON CELL. If needed, adjust the pointing to I2 again.

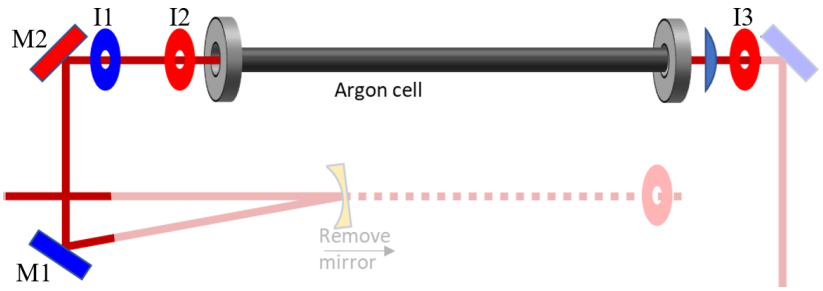

Fig. A.17. Alignment through the argon cell. For initial alignment, M1 and M2 align the beam through I1 and I2, respectively. I2 attenuates the beam going into argon cell. For final alignment, M1 and M2 align the beam through I1 and I3, respectively.

Into the Periscope. ARG irises are used. Two-mirror alignment procedures are used. Fig. A18. shows optics layout. Flip the top mirror of the periscope out of the way. M1 is a dichroic and only reflects <750 nm light.

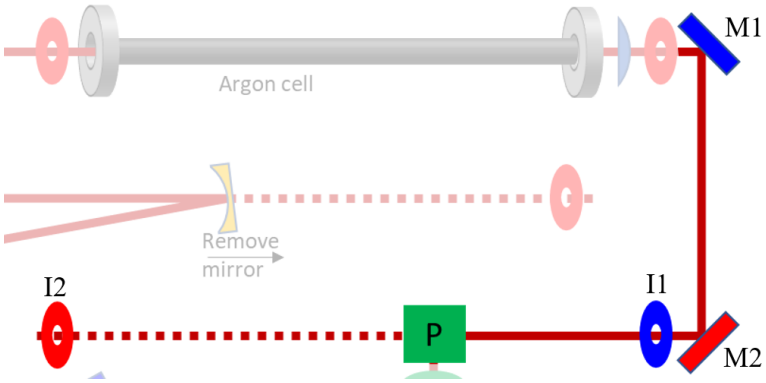

Fig. A.18. Alignment into the periscope (P). Upper periscope mirror is flipped out of path. M1 and M2 align the beam through I1 and I2, respectively.

Periscope Part 1. PER irises are used. One-mirror alignment procedures are used. Fig. A.7 shows optics layout. The lower mirror mounted on a magnetic baseplate is removed. WARNING: WEAR APPROPRIATE LASER GOGGLES DURING VERTICAL ALIGNMENT. A screw and post spacer (Thorlabs part RS5M) is screwed

into the laser table after the lower mirror is removed. The screw serves as I2. If possible, use an anodized screw for this. I1 is a tube mounted iris. The tube has a side viewing window. It fits over the post spacer. Follow the 1-mirror alignment procedures.

Periscope Part 2. AP irises are used. One-mirror alignment procedures with special instructions are used. Fig. A.7 shows optics layout. The upper mirror of the periscope is mounted on a translation stage. The lower mirror is mounted on a magnetic mount. The lower mirror turns the beam 90° towards the prism compressor.

The mirror after the periscope is mounted on a flipper mount and is flipped down for alignment. One-mirror alignment procedures are used with the D knob correcting for the vertical axis on I1. The translation stage for the upper mirror of the periscope may be used for correcting the horizontal axis on I1. After this alignment and before the alignment into the SSTA prism compressor, align into the traditional TA prism compressor.

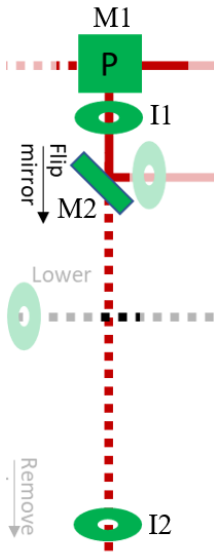

Fig. A.19. Alignment out of periscope (P). M2 is flipped out path. Lower periscope mirror (M1) aligns beam through I1 and I2.

Down the Table. AP irises are used. One-mirror alignment procedures are used. Fig. A.20 shows optics layout.

Fig. A.20. Alignment down table. M1 aligns beam through I1 and I2.

Path Compensation. No irises are used. Fig. A.21 shows optics layout. M2 is mounted on a track to compensate for path length changes in the pump line. M2 is only moved for two circumstances. First, the polarization of the pump out of the OPA is changed. Second, the distance between the prisms in the prism compressor is changed. Move M2 to increase or decrease the path length accordingly. Adjust M1 such that the beam hits the center of M2. Adjust M2 such that the beam hits the center of the next mirror M3.

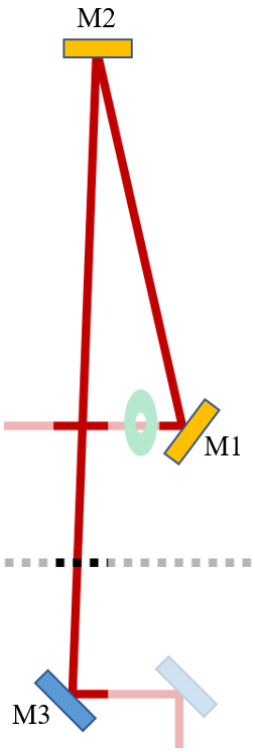

Fig. A.21. Path compensation alignment. M1 aligns beam to center of M2. M2 aligns beam to center of M3.

Stage 2

Fig. A.22 shows the general alignment procedures for the pump and probe beams through Stage 2 of the setup. For single-color measurements, the probe comes from the straight path through the beam splitter. For single-color measurements, a mirror on a magnetic baseplate, a half-wave plate, and a polarizer are placed in the setup. For broadband measurements, they are removed and the beam comes from the beam path compensation section.

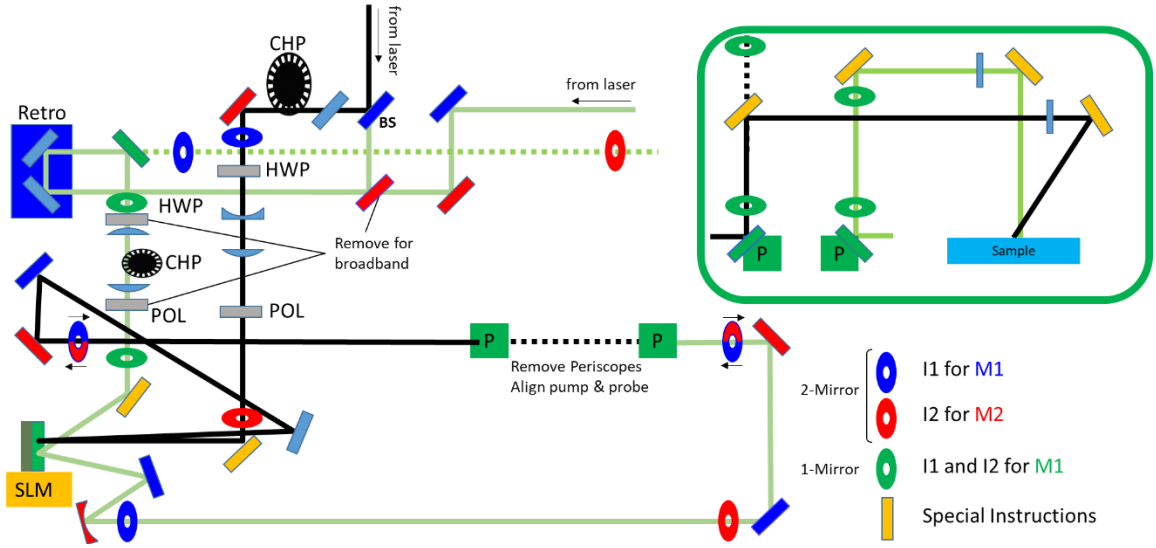

Fig. A.22. Stage 2 alignment procedures. The pump path (black) and probe path (red) are shown. Mirror colors correspond to 1-mirror (green) and 2-mirror (blue and red) alignment procedures. Special instructions are marked with orange. Pale blue optics are rarely adjusted or not described in this section. BS, beam splitter; CHP, optical chopper; HWP, half-wave plate; P, periscope; POL, polarizer; SLM, spatial light modulator.

Pump

The pump reflects off of the beam splitter and passes through a wedged window and optical chopper. The wedged window compensates for the probe passing through the beam splitter in single-color measurements. Optical chopper frequencies are described elsewhere. The pump is resized using a concave-plano lens and plano-convex lens telescope. The polarization is rotated from horizontal to vertical using a half-wave plate.

A polarizer filters the light to a vertical polarization. The SLM requires vertical polarization. The beam is reshaped using the SLM. The first order is directed towards a periscope. The beam is focused by a cylindrical lens to a line at the sample plane. The pump is imaged at the sample plane using a photoluminescence dye. The following irises are used:

1. "After Prism" small (APS)
2. "After Prism" large (APL)
3. SLM iris (SLMI)
4. "SSTA H" (SSTA)

APS is used before the beam is expanded. APL is used after the beam is expanded. SLMI is a computer-controlled iris built into the SLM software. SSTA is used to align up the periscope.

After the Beam Splitter. APS and APL irises are used. Two-mirror alignment procedures are used. Fig. A.23 shows optics layout. APS is placed before the half-wave plate. APL is placed after the polarizer. The beam splitter (BS) is used as M1. For single-color measurements, this alignment procedure must be performed before the probe is aligned into the retroreflector.

Through the SLM. SLMI iris is used with special alignment instructions. Fig. A.24 shows optics layout. Using the SLM software, put up the phase pattern used for alignment. The horizontal shift imposed by the SLM should always be the same. Put a beam block before M3 and let the beam hit the beam block. The 0^{th} order and 1^{st} order beam will both hit the beam block (Fig. A.24, Open). Close down SLMI iris (on the software) for the pump beam until the 0^{th} and 1^{st} order look like Fig. A.24, Closed. Adjust M1 to center the box in the 0^{th} order beam. Use M2 to align the beam to the center of M3.

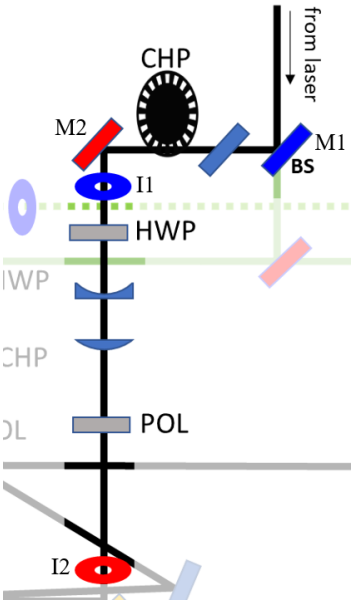

Fig. A.23. Alignment beam splitter. M1 and M2 align the beam through I1 and I2, respectively. BS, beam splitter; CHP, optical chopper; HWP, half-wave plate; POL, polarizer.

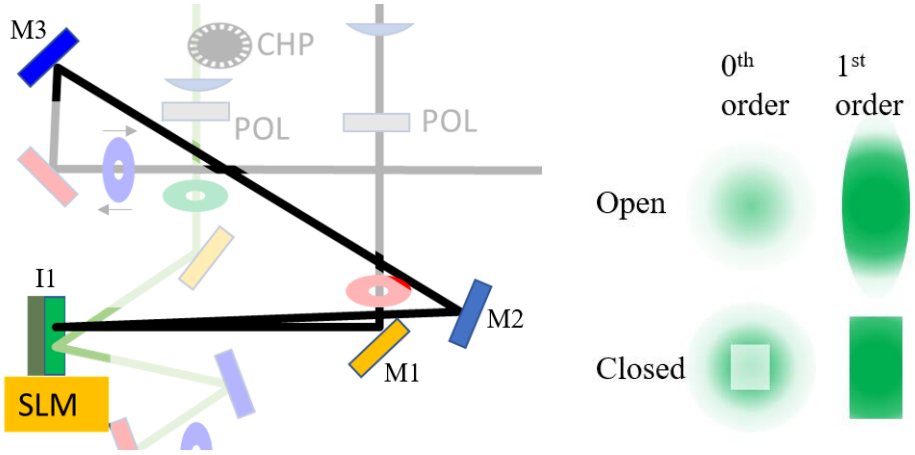

Fig. A.24. Alignment through SLM (left) and software iris (I1) examples (right). M1 centers beam on pump side (top) of SLM. M2 centers beam on M3. With software iris open (closed), beam at M3 resembles 0^{th} and 1^{st} order Open (Closed) patterns.

Into the Periscope. APL irises are used. Two-mirror alignment procedures are used. Fig. A.25 shows optics layout. For this alignment, the periscope mirrors (mounted on magnetic base plates) are removed. The beam is oblong for this alignment. Adjust the iris aperture size according to the axis being align (Fig. A.25, vertical or horizontal).

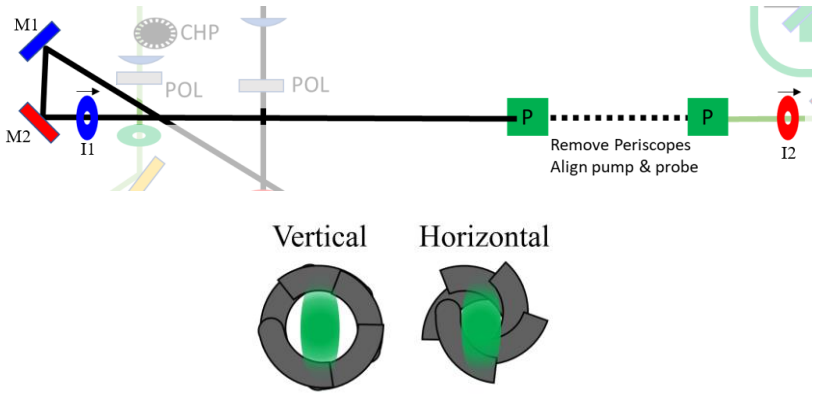

Fig. A.25. Alignment into periscope (top) and schematic of beam on iris (bottom). Periscopes (P) are both removed. M1 and M2 align the beam through I1 and I2, respectively. (Bottom) Recommended iris aperture size for vertical and horizontal alignment.

Up the Periscope. SSTA irises are used. One-mirror alignment procedures are used. Fig. A.26 shows optics layout. Align both the pump and probe into their periscopes before performing this step. M2 is flipped out of the beam path. WARNING! CONTROL THE BEAM DURING VERTICAL ALIGNMENT. DO NOT PUT YOUR HEAD OVER THE IRISES OR BEND DOWN TO LOOK AT THE FACE OF THE IRISES. The beam is too faint to wear laser goggles during alignment but can still damage eyes. To align, look at the leak-through of the beam on a notecard, Fig. A.26 (right).

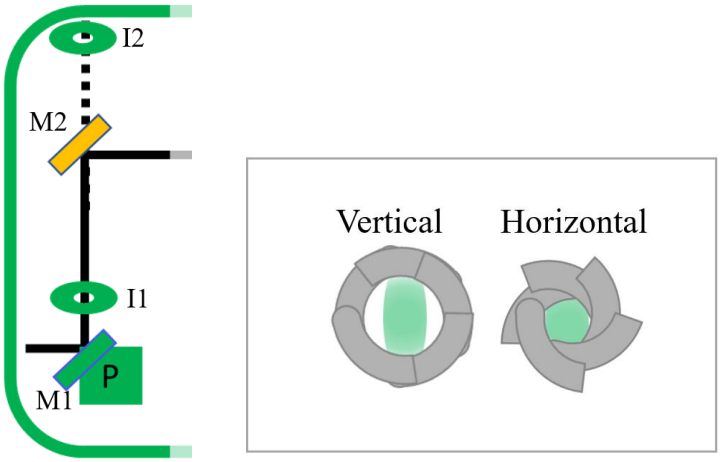

Fig. A.26. Alignment up periscope (left) and projection of beam on iris through notecard (right). M2 is flipped out of the path. M1 aligns the beam through I1 and I2. A notecard is placed above I2 to view the projection of the beam onto the iris for alignment. (Right) Recommended iris aperture size for vertical and horizontal alignment.

Onto the Sample: Part 1. No irises are used. Special alignment procedures are used. Fig. A.27 shows optics layout. Fig. A.28 show beam on sample slit viewed from above. Center the beam onto the cylindrical lens (CYL) using M1. Place a photoluminescent sample resonant with the pump at the sample stage and start imaging the sample plane using the SSTA software. The exposure should be set to ~0.2 s. WARNING: BEFORE SETTING THE EXPOSURE, ENSURE THAT THE PROBE BEAM IS BLOCKED AND WILL NOT HIT THE DETECTOR. THIS COULD IRREPARABLY DAMAGE THE DETECTOR. The spectral range imaged by the camera should include the photoluminescence wavelength range. Adjust H on M2 until signal is observed on the detector. The focal line of the sample probably will not be aligned with the imaged slit and only a small portion will actually hit the detector, Fig. A.28a. Adjust H on M2 and the signal peak will shift across the slit, Fig. A.28b, A.28c. Alternate adjusting H in opposite directions on M1 and M2 (e.g. clockwise on M1 and counterclockwise on M2) to rotate the beam to align with the slit as shown in Fig. A.28d-f.

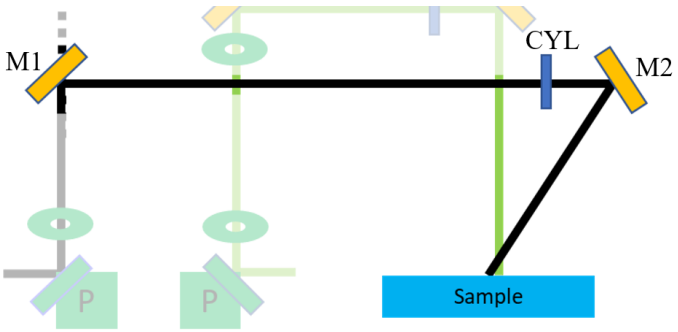

Fig. A.27. Alignment onto the sample. M1 and M2 align the beam onto the sample. CYL, cylindrical lens.

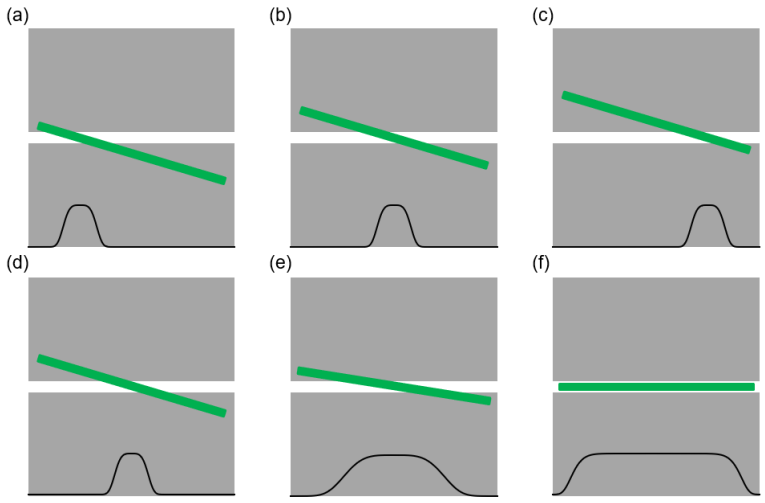

Fig. A.28. Imaged projection of pump beam onto sample slit with integrated intensity profile (black) for light overlapped onto slit and imaged by detector. (a-c) Effect of vertical position on integrated intensity. (d-f) Effect of angle between beam and slit on integrated intensity.

Onto the Sample: Part 2. No irises are used. Special alignment instructions are used. Fig. A.29a shows the path of the pump from the cylindrical lens to the sample slit. The steep incident angle of the pump beam at the sample results in non-uniform focusing at the sample position. The pump beam (Fig. A.29b) produces a bowtie-shaped area of excitation at the sample plane, resulting in a non-uniform energy density. Reshape the pump profile using the SLM to include three equal intensity peaks, once centered and one on either end. Adjust the variable focusing for each side of the beam until the intensity of the three beams matches, Fig. A.29c. Tweak H on M1 and M2 to optimize the angle of the beam. If the intensity on one of the edge peaks is low and the opposite peak is high and it is not due to the projection angle of the pump beam (previous step), then adjust the pointing onto the SLM using V on the mirror just before the SLM and compensate for the vertical offset using V on the mirror just after the SLM.

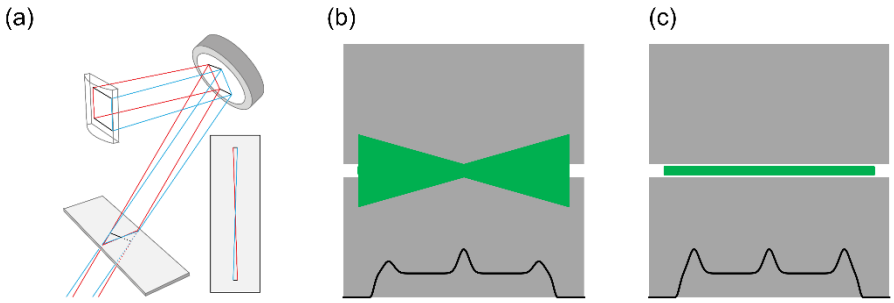

Fig. A.29. Pump beam focus correction. (a) Pump beam focused onto the sample plane using a cylindrical lens with each side of the beam traced to its projection on the sample. Inset: Projection of pump onto sample, viewed from top. (b) and (c) Imaged projection of 3-peak pump beam onto sample slit with integrated intensity profile (black) for light overlapped onto slit and imaged by detector. (b) Defocused pump edges cause lower intensity to hit the detector at the edges. (c) Beam profile with pump focus correction.

Probe

The probe can either be single-color using the transmitted light through the pump beam splitter or broadband, Fig. A.22. A mirror mounted on a magnetic mount after the beam splitter is removed for broadband measurements. The probe reflects off a retroreflector which serves as a delay line. The beam is resized by two plano-convex mirrors and is modulated using an optical chopper. A half-wave plate and polarizer combination is used for single-color measurements to rotate the polarization 90° (from horizontal to vertical) and adjust the probe fluency. For broadband measurements the polarization is already vertical in this region and these optics are removed. The beam profile is reshaped by the SLM. A cylindrical mirror is used to collimate the spectral diffraction induced by the SLM. A slit is used to filter out the 0^{th} order reflection of the beam. The first order is directed towards a periscope. The beam is focused by a cylindrical lens to a line at the sample plane. The probe is imaged at the sample plane onto the entrance slit of a spectrograph which is imaged onto a 2-dimensional array detector. The following irises are used:

1. “After Prism” small (APS)

2. “After Prism” large (APL)
3. SLM iris (SLMI)
4. “SSTA H” (SSTA)

APS is used before the beam is expanded. APL is used after the beam is expanded. SLMI is a computer-controlled iris built into the SLM software. SSTA is used to align up the periscope.

Into the Retroreflector. APS irises are used. Two-mirror alignment procedures with special instructions are used. Fig. A.30 and A.31 show optics layouts for single-color and broadband configurations, respectively. Flip M3 out of the beam path. For single color measurements M1 is placed after the beam splitter in the pump line. M2 is the retroreflector and is adjusted using the side-ways mounted translation stages. M1 aligns to I2 and the retroreflector (M2) aligns to I1 using the translation stages. For broadband measurements the single-color M1 is removed and the two mirrors before the retroreflector are M1 and M2. M1 aligns to I1 and M2 aligns to I2.

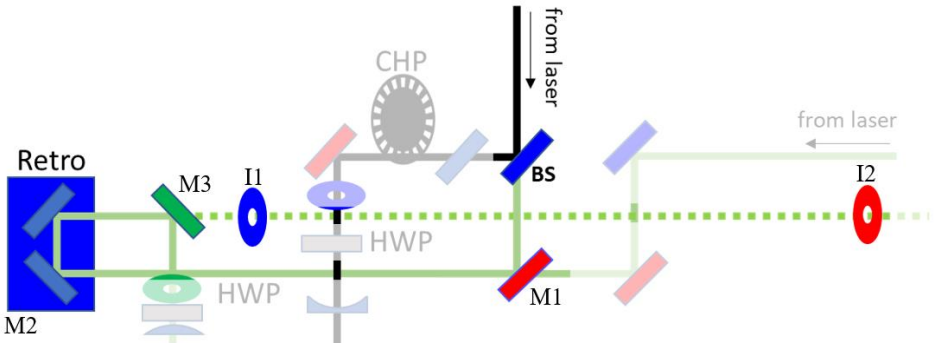

Fig. A.30. Single-color beam after beam splitter alignment through retroreflector. M3 is flipped out of the path. M1 aligns beam to I2. The retroreflector is mounted horizontally on manual translation stages with vertical and side-to-side control. M2 aligns beam onto I1 using stages.

After the Retroreflector. APS and APL irises are used. One-mirror alignment procedures are used. Fig. A.32 shows optics layout. The half-wave plate (HWP) and

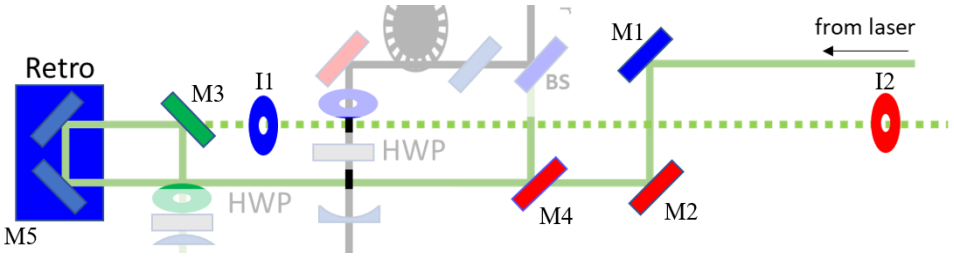

Fig. A.31. Broadband beam alignment through retroreflector (Retro). M3 is flipped out of the path. M4 is removed. M5 is not adjusted. M1 and M2 align the beam through I1 and I2, respectively.

polarizer (POL) are removed for broadband light. Use APS and APL to align beam to I1 and I2, respectively.

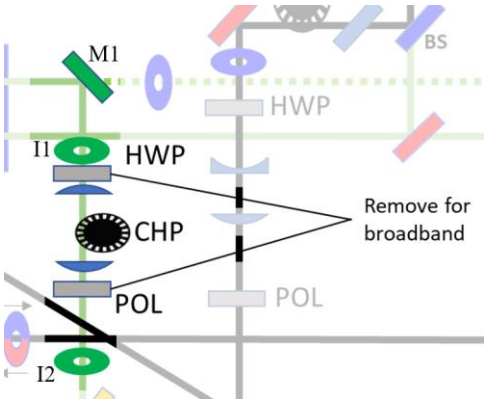

Fig. A.32. Alignment after retroreflector. HWP and POL are removed for broadband probe beam. M1 aligns the beam through I1 and I2. CHP, optical chopper; HWP, half-wave plate; POL, polarizer.

Through the SLM. SLMI iris is used. Special alignment procedures are used. Fig. A.33 shows optics layout. Using the SLM software, put up the phase pattern used for alignment. The horizontal shift imposed by the SLM should always be the same. Put a beam block before M3 and let the beam hit the beam block. The 0^{th} order and 1^{st} order beam will both hit the beam block (Fig. A.33, Open). Close down SLMI iris (on the software) for the pump beam until the 0^{th} and 1^{st} order look like Fig. A.33, Closed. Adjust M1 to center the box in the 0^{th} order beam. Use M2 to align the beam to the center of M3.

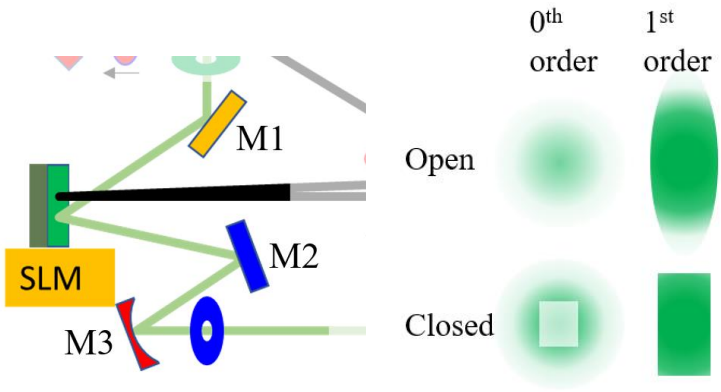

Fig. A.33. Alignment through SLM (left) and software iris (I1) examples (right). M1 centers beam on probe side (bottom) of SLM. M2 centers beam on M3. With software iris open (closed), beam at M3 resembles 0^{th} and 1^{st} order Open (Closed) patterns.

Down the Table. APS and APL irises are used. Two-mirror alignment procedures are used. Fig. A.34 shows optics layout. After two-mirror alignment, if the beam is not centered on M2 then repeat alignment onto the SLM. After the beam is well aligned, a slit may be added between the irises to filter out the 0^{th} and higher order beams.

Fig. A.34. Alignment down table after SLM. M1 and M2 align the beam through I1 and I2, respectively.

Into the Periscope. APL irises are used. Two-mirror alignment procedures are used. Fig. A.35 shows optics layout. The periscope mirrors (mounted on magnetic base plates) are removed. M1 and M2 align the beam through I1 and I2, respectively. The beam is oblong for this alignment. Adjust the opening of the iris according to which axis you are aligning (see Fig. A.25, bottom).

Up the Periscope. SSTA irises are used. One-mirror alignment procedures are used. Fig. A.36 shows optics layout. Align both the pump and probe into their periscopes before performing this step. WARNING! CONTROL THE BEAM DURING

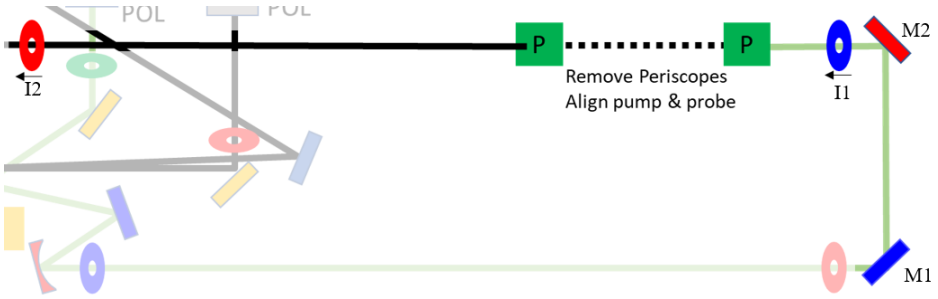

Fig. A.35. Alignment into periscope. Periscopes (P) are both removed. M1 and M2 align the beam through I1 and I2, respectively.

VERTICAL ALIGNMENT. DO NOT PUT YOUR HEAD OVER THE IRISES OR BEND DOWN TO LOOK AT THE FACE OF THE IRISES. The beam is too faint to wear laser goggles during alignment but can still damage eyes. To align, look at the leak-through of the beam on a notecard or hold a notecard after the top periscope mirror, see Fig. A.26 (right).

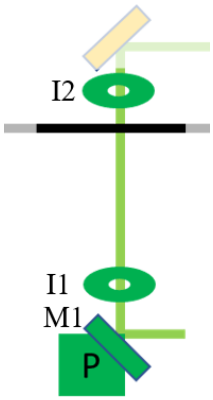

Fig. A.36. Alignment up periscope. M1 aligns the beam through I1 and I2. A notecard is placed above I2 to view the projection of the beam onto the iris for alignment. (Right) Recommended iris aperture size for vertical and horizontal alignment.

Onto the Sample. No irises are used. Special alignment procedures are used. Fig. A.37 shows optics layout. Use M1 to approximately center the beam onto the cylindrical lens (CYL). Using the SSTA software align the beam onto the sample position using M2. WARNING! ENSURE THAT THE DETECTOR EXPOSURE IS SET LOW ENOUGH TO PREVENT DETECTOR DAMAGE! Adjust H on M2 until signal is observed on the

detector. The focal line of the sample probably will not be aligned with the imaged slit and only a small portion will actually hit the detector, Fig. A.28a. Adjust H on M2 and the signal peak will shift across the slit, Fig. A.28b, A.28c. Alternate adjusting H in opposite directions on M1 and M2 (e.g. clockwise on M1 and counterclockwise on M2) to rotate the beam to align with the slit as shown in Fig. A.28d-f.

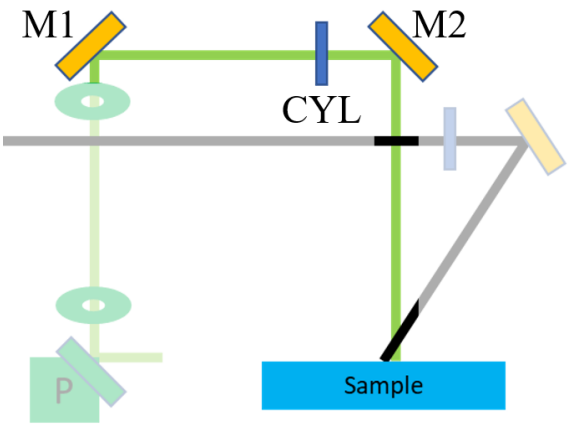

Fig. A.37. Alignment onto sample through cylindrical lens (CYL). M1 and M2 align beam to sample slit.

REFERENCES CITED

(1) Berera, R.; van Stokkum, I. H. M.; d'Haene, S.; Kennis, J. T. M.; van Grondelle, R.; Dekker, J. P. A Mechanism of Energy Dissipation in Cyanobacteria. *Biophysical Journal* **2009**, *96* (6), 2261–2267. https://doi.org/10.1016/j.bpj.2008.12.3905.

(2) Berera, R.; Herrero, C.; Stokkum, I. H. M. van; Vengris, M.; Kodis, G.; Palacios, R. E.; Amerongen, H. van; Grondelle, R. van; Gust, D.; Moore, T. A.; Moore, A. L.; Kennis, J. T. M. A Simple Artificial Light-Harvesting Dyad as a Model for Excess Energy Dissipation in Oxygenic Photosynthesis. *PNAS* **2006**, *103* (14), 5343–5348. https://doi.org/10.1073/pnas.0508530103.

(3) El-Khouly, M. E.; Fukuzumi, S.; D'Souza, F. Photosynthetic Antenna–Reaction Center Mimicry by Using Boron Dipyrromethene Sensitizers. *ChemPhysChem* **2014**, *15* (1), 30–47. https://doi.org/10.1002/cphc.201300715.

(4) Xing, G.; Mathews, N.; Sun, S.; Lim, S. S.; Lam, Y. M.; Grätzel, M.; Mhaisalkar, S.; Sum, T. C. Long-Range Balanced Electron- and Hole-Transport Lengths in Organic-Inorganic CH3NH3PbI3. *Science* **2013**, *342* (6156), 344–347. https://doi.org/10.1126/science.1243167.

(5) Qian, D.; Zheng, Z.; Yao, H.; Tress, W.; Hopper, T. R.; Chen, S.; Li, S.; Liu, J.; Chen, S.; Zhang, J.; Liu, X.-K.; Gao, B.; Ouyang, L.; Jin, Y.; Pozina, G.; Buyanova, I. A.; Chen, W. M.; Inganäs, O.; Coropceanu, V.; Bredas, J.-L.; Yan, H.; Hou, J.; Zhang, F.; Bakulin, A. A.; Gao, F. Design Rules for Minimizing Voltage Losses in High-Efficiency Organic Solar Cells. *Nature Materials* **2018**, *17* (8), 703–709. https://doi.org/10.1038/s41563-018-0128-z.

(6) Wilson, K. S.; Wong, C. Y. In Situ Measurement of Exciton Dynamics During Thin-Film Formation Using Single-Shot Transient Absorption. *J. Phys. Chem. A* **2018**, *122* (31), 6438–6444. https://doi.org/10.1021/acs.jpca.8b06248.

(7) Yang, J.; Siempelkamp, B. D.; Liu, D.; Kelly, T. L. Investigation of CH3NH3PbI3 Degradation Rates and Mechanisms in Controlled Humidity Environments Using in Situ Techniques. *ACS Nano* **2015**, *9* (2), 1955–1963. https://doi.org/10.1021/nn506864k.

(8) Bhattacharyya, R.; Key, B.; Chen, H.; Best, A. S.; Hollenkamp, A. F.; Grey, C. P. In Situ NMR Observation of the Formation of Metallic Lithium Microstructures in Lithium Batteries. *Nature Materials* **2010**, *9* (6), 504–510. https://doi.org/10.1038/nmat2764.

(9) Malley, M. M.; Rentzepis, P. M. Picosend Molecular Relaxation Displayed with Crossed Laser Beams. *Chemical Physics Letters* **1969**, *3* (7), 534–536. https://doi.org/10.1016/0009-2614(69)85055-4.

(10) Topp, M. R.; Rentzepis, P. M.; Jones, R. P. Time-Resolved Absorption Spectroscopy in the 10−12 -sec Range. *Journal of Applied Physics* **1971**, *42* (9), 3415–3419. https://doi.org/10.1063/1.1660747.

(11) Salin, F.; Georges, P.; Roger, G.; Brun, A. Single-Shot Measurement of a 52-Fs Pulse. *Appl. Opt., AO* **1987**, *26* (21), 4528–4531. https://doi.org/10.1364/AO.26.004528.

(12) Dhar, L.; Fourkas, J. T.; Nelson, K. A. Pulse-Length-Limited Ultrafast Pump–Probe Spectroscopy in a Single Laser Shot. *Opt. Lett., OL* **1994**, *19* (9), 643–645. https://doi.org/10.1364/OL.19.000643.

(13) Furukawa, N.; Mair, C. E.; Kleiman, V. D.; Takeda, J. Femtosecond Real-Time Pump–Probe Imaging Spectroscopy. *Appl. Phys. Lett.* **2004**, *85* (20), 4645–4647. https://doi.org/10.1063/1.1823039.

(14) Wilson, K. S.; Wong, C. Y. Single-Shot Transient Absorption Spectroscopy with a 45 Ps Pump-Probe Time Delay Range. *Opt. Lett., OL* **2018**, *43* (3), 371–374. https://doi.org/10.1364/OL.43.000371.

(15) Wilson, K. S.; Mapile, A. N.; Wong, C. Y.; Wong, C. Y.; Wong, C. Y. Broadband Single-Shot Transient Absorption Spectroscopy. *Opt. Express, OE* **2020**, *28* (8), 11339–11355. https://doi.org/10.1364/OE.390938.

(16) Wakeham, G. P.; Nelson, K. A. Dual-Echelon Single-Shot Femtosecond Spectroscopy. *Optics Letters* **2000**, *25* (7), 505–507. https://doi.org/10.1364/OL.25.000505.

(17) Wakeham, G. P.; Chung, D. D.; Nelson, K. A. Femtosecond Time-Resolved Spectroscopy of Energetic Materials. *Thermochimica Acta* **2002**, *384* (1), 7–21. https://doi.org/10.1016/S0040-6031(01)00774-2.

(18) Shin, T.; Wolfson, J. W.; Teitelbaum, S. W.; Kandyla, M.; Nelson, K. A. Dual Echelon Femtosecond Single-Shot Spectroscopy. *Review of Scientific Instruments* **2014**, *85* (8), 083115. https://doi.org/10.1063/1.4893641.

(19) Poulin, P. R.; Nelson, K. A. Irreversible Organic Crystalline Chemistry Monitored in Real Time. *Science* **2006**, *313* (5794), 1756–1760. https://doi.org/10.1126/science.1127826.

(20) Teitelbaum, S. W.; Shin, T.; Wolfson, J. W.; Cheng, Y.-H.; Porter, I. J.; Kandyla, M.; Nelson, K. A. Real-Time Observation of a Coherent Lattice Transformation into a High-Symmetry Phase. *Phys. Rev. X* **2018**, *8* (3), 031081. https://doi.org/10.1103/PhysRevX.8.031081.

(21) Katayama, I.; Sakaibara, H.; Takeda, J. Real-Time Time–Frequency Imaging of Ultrashort Laser Pulses Using an Echelon Mirror. *Jpn. J. Appl. Phys.* **2011**, *50* (10R), 102701. https://doi.org/10.1143/JJAP.50.102701.

(22) Sakaibara, H.; Ikegaya, Y.; Katayama, I.; Takeda, J. Single-Shot Time-Frequency Imaging Spectroscopy Using an Echelon Mirror. *Opt. Lett., OL* **2012**, *37* (6), 1118–1120. https://doi.org/10.1364/OL.37.001118.

(23) Minami, Y.; Yamaki, H.; Katayama, I.; Takeda, J. Broadband Pump–Probe Imaging Spectroscopy Applicable to Ultrafast Single-Shot Events. *Appl. Phys. Express* **2014**, *7* (2), 022402. https://doi.org/10.7567/APEX.7.022402.

(24) Takeda, J.; Oba, W.; Minami, Y.; Saiki, T.; Katayama, I. Ultrafast Crystalline-to-Amorphous Phase Transition in Ge2Sb2Te5 Chalcogenide Alloy Thin Film Using Single-Shot Imaging Spectroscopy. *Appl. Phys. Lett.* **2014**, *104* (26), 261903. https://doi.org/10.1063/1.4886969.

(25) Beddard, G. S.; McFadyen, G. G.; Reid, G. D.; Thorne, J. R. G. Pulse Transform Transient Absorption Spectroscopy. *Chemical Physics Letters* **1992**, *198* (6), 641–644. https://doi.org/10.1016/0009-2614(92)85042-9.

(26) Shkrob, I. A.; Oulianov, D. A.; Crowell, R. A.; Pommeret, S. Frequency-Domain "Single-Shot" Ultrafast Transient Absorption Spectroscopy Using Chirped Laser Pulses. *Journal of Applied Physics* **2004**, *96* (1), 25–33. https://doi.org/10.1063/1.1711178.

(27) Kobayashi, M.; Minami, Y.; Johnson, C. L.; Salmans, P. D.; Ellsworth, N. R.; Takeda, J.; Johnson, J. A.; Katayama, I. High-Acquisition-Rate Single-Shot Pump-Probe Measurements Using Time-Stretching Method. *Scientific Reports* **2016**, *6*, 37614. https://doi.org/10.1038/srep37614.

(28) Fujimoto, M.; Aoshima, S.; Tsuchiya, Y. Ultrafast Imaging to Measure Instantaneous Intensity Distributions of Femtosecond Optical Pulses Propagating in a Medium. *Meas. Sci. Technol.* **2002**, *13* (11), 1698. https://doi.org/10.1088/0957-0233/13/11/306.

(29) Malley, M. M.; Rentzepis, P. M. Picosecond Time-Resolved Stimulation Light Emission. *Chemical Physics Letters* **1970**, *7* (1), 57–60. https://doi.org/10.1016/0009-2614(70)80248-2.

(30) Mead, G.; Katayama, I.; Takeda, J.; Blake, G. A. An Echelon-Based Single Shot Optical and Terahertz Kerr Effect Spectrometer. *Review of Scientific Instruments* **2019**, *90* (5), 053107. https://doi.org/10.1063/1.5088377.

(31) Wilson, K. S.; Wong, C. Y. Calibrating a Spatially Encoded Time Delay for Transient Absorption Spectroscopy. In *Physical Chemistry of Semiconductor Materials and Interfaces XVI*; International Society for Optics and Photonics, 2017; Vol. 10348, p 1034805. https://doi.org/10.1117/12.2272535.

(32) Cook, S.; Furube, A.; Katoh, R. Analysis of the Excited States of Regioregular Polythiophene P3HT. *Energy & Environmental Science* **2008**, *1* (2), 294–299. https://doi.org/10.1039/B805643A.

(33) Cook, S.; Liyuan, H.; Furube, A.; Katoh, R. Singlet Annihilation in Films of Regioregular Poly(3-Hexylthiophene): Estimates for Singlet Diffusion Lengths and the Correlation between Singlet Annihilation Rates and Spectral Relaxation. *J. Phys. Chem. C* **2010**, *114* (24), 10962–10968. https://doi.org/10.1021/jp101340b.

(34) Makishima, Y.; Furukawa, N.; Ishida, A.; Takeda, J. Femtosecond Real-Time Pump-Probe Imaging Spectroscopy Implemented on a Single Shot Basis. *Jpn. J. Appl. Phys.* **2006**, *45* (7R), 5986–5989. https://doi.org/10.1143/JJAP.45.5986.

(35) Aagedal, H.; Schmid, M.; Egner, S.; Müller-Quade, J.; Beth, T.; Wyrowski, F. Analytical Beam Shaping with Application to Laser-Diode Arrays. *J. Opt. Soc. Am. A, JOSAA* **1997**, *14* (7), 1549–1553. https://doi.org/10.1364/JOSAA.14.001549.

(36) Rick van Bijnen. Quantum Engineering with Ultracold Atoms.

(37) Brodeur, A.; Chin, S. L. Ultrafast White-Light Continuum Generation and Self-Focusing in Transparent Condensed Media. *J. Opt. Soc. Am. B, JOSAB* **1999**, *16* (4), 637–650. https://doi.org/10.1364/JOSAB.16.000637.

(38) Ferrari, R.; D'Andrea, C.; Bassi, A.; Valentini, G.; Cubeddu, R. Time-Gated Real-Time Pump-Probe Imaging Spectroscopy. In *Novel Optical Instrumentation for Biomedical Applications III (2007), paper 6631_46*; Optical Society of America, 2007; p 6631_46. https://doi.org/10.1364/ECBO.2007.6631_46.

(39) Dubietis, A.; Tamošauskas, G.; Šuminas, R.; Jukna, V.; Couairon, A. Ultrafast Supercontinuum Generation in Bulk Condensed Media (Invited Review). *arXiv:1706.04356 [physics]* **2017**.

(40) Kumar, R. S. S.; Deepak, K. L. N.; Rao, D. N. Depolarization Properties of the Femtosecond Supercontinuum Generated in Condensed Media. *Phys. Rev. A* **2008**, *78* (4), 043818. https://doi.org/10.1103/PhysRevA.78.043818.

(41) Werley, C. A.; Teo, S. M.; Ofori-Okai, B. K.; Sivarajah, P.; Nelson, K. A. High-Resolution, Low-Noise Imaging in THz Polaritonics. *IEEE Transactions on Terahertz Science and Technology* **2013**, *3* (3), 239–247. https://doi.org/10.1109/TTHZ.2013.2250580.

(42) Wilson, K. S.; Scott, M. N.; Wong, C. Y. Excited State Dynamics of Organic Semiconductors Measured with Shot-to-Shot Correction of Scatter and Photoluminescence. *Synthetic Metals* **2019**, *250*, 115–120. https://doi.org/10.1016/j.synthmet.2019.03.007.

(43) Fourkas, J. T.; Dhar, L.; Nelson, K. A. Spatially Encoded, Single-Shot Ultrafast Spectroscopies. *J. Opt. Soc. Am. B* **1995**, *12* (1), 155–165. https://doi.org/10.1364/JOSAB.12.000155.

(44) Sadighian, J. C.; Wilson, K. S.; Crawford, M. L.; Wong, C. Y. Evolving Stark Effect During Growth of Perovskite Nanocrystals Measured Using Transient Absorption. *Front. Chem.* **2020**, *8*, 897. https://doi.org/10.3389/fchem.2020.585853.

(45) Wilson, K. S.; Scott, M. N.; Wong, C. Y. Single-Shot Transient Absorption Spectroscopy of an Organic Film. *MRS Advances* **2018**, *3* (59), 3453–3457. https://doi.org/10.1557/adv.2018.402.

(46) Marsh, R. A.; Hodgkiss, J. M.; Albert-Seifried, S.; Friend, R. H. Effect of Annealing on P3HT:PCBM Charge Transfer and Nanoscale Morphology Probed by Ultrafast Spectroscopy. **2010**. https://doi.org/10.1021/nl9038289.

(47) Pace, N. A.; Reid, O. G.; Rumbles, G. Delocalization Drives Free Charge Generation in Conjugated Polymer Films. *ACS Energy Lett.* **2018**, *3* (3), 735–741. https://doi.org/10.1021/acsenergylett.8b00108.

(48) Amassian, A.; Pozdin, V. A.; Li, R.; Smilgies, D.-M.; Malliaras, G. G. Solvent Vapor Annealing of an Insoluble Molecular Semiconductor. *Journal of Materials Chemistry* **2010**, *20* (13), 2623. https://doi.org/10.1039/b923375j.

(49) Kolb, F.; Busby, Y.; Houssiau, L.; List-Kratochvil, E. J. W. In-Depth Investigation of the Charge Extraction Efficiency for Thermally Annealed Inverted Bulk-Heterojunction Solar Cells. *Journal of Applied Physics* **2019**, *125* (3), 034502. https://doi.org/10.1063/1.5052409.

(50) Yan, L.; Hu, J.; Guo, Z.; Chen, H.; Toney, M. F.; Moran, A. M.; You, W. General Post-Annealing Method Enables High-Efficiency Two-Dimensional Perovskite Solar Cells. *ACS Appl. Mater. Interfaces* **2018**, *10* (39), 33187–33197. https://doi.org/10.1021/acsami.8b10230.

(51) Yeon Yang, H.; Park, H.-W.; Jin Kim, S.; Hong, J.-M.; Whan Kim, T.; Hwan Kim, D.; Ah Lim, J. Intense Pulsed Light Induced Crystallization of a Liquid-Crystalline Polymer Semiconductor for Efficient Production of Flexible Thin-Film Transistors. *Physical Chemistry Chemical Physics* **2016**, *18* (6), 4627–4634. https://doi.org/10.1039/C5CP06989K.

(52) T. Hoke, E.; J. Slotcavage, D.; R. Dohner, E.; R. Bowring, A.; I. Karunadasa, H.; D. McGehee, M. Reversible Photo-Induced Trap Formation in Mixed-Halide Hybrid Perovskites for Photovoltaics. *Chemical Science* **2015**, *6* (1), 613–617. https://doi.org/10.1039/C4SC03141E.

(53) Kosma, K.; Trushin, S. A.; Fuß, W.; Schmid, W. E. Characterization of the Supercontinuum Radiation Generated by Self-Focusing of Few-Cycle 800 Nm Pulses in Argon. *Journal of Modern Optics* **2008**, *55* (13), 2141–2177. https://doi.org/10.1080/09500340801979325.

(54) Cladé, P. *PyDAQmx: A Python Interface to the National Instruments DAQmx Driver*; 2016.

(55) Brazard, J.; Bizimana, L. A.; Turner, D. B. Accurate Convergence of Transient-Absorption Spectra Using Pulsed Lasers. *Review of Scientific Instruments* **2015**, *86* (5), 053106. https://doi.org/10.1063/1.4921479.

(56) Koprinkov, I. G.; Suda, A.; Nurhuda, M.; Wang, P.; Midorikawa, K. Observation of Two Different Types of Optical Supercontinua: Structured and Structureless. *Phys. Rev. A* **2006**, *74* (5), 053819. https://doi.org/10.1103/PhysRevA.74.053819.

(57) Wang, Z.; Liu, J.; Li, R.; Xu, Z. Supercontinuum Generation and Pulse Compression from Gas Filamentation of Femtosecond Laser Pulses with Different Durations. *Opt. Express, OE* **2009**, *17* (16), 13841–13850. https://doi.org/10.1364/OE.17.013841.

(58) Champeaux, S.; Bergé, L. Femtosecond Pulse Compression in Pressure-Gas Cells Filled with Argon. *Phys. Rev. E* **2003**, *68* (6), 066603. https://doi.org/10.1103/PhysRevE.68.066603.

(59) Aagedal, H.; Schmid, M.; Egner, S.; Müller-Quade, J.; Beth, T.; Wyrowski, F. Analytical Beam Shaping with Application to Laser-Diode Arrays. *J. Opt. Soc. Am. A, JOSAA* **1997**, *14* (7), 1549–1553. https://doi.org/10.1364/JOSAA.14.001549.

(60) Davis, J. A.; Cottrell, D. M.; Lilly, R. A.; Connely, S. W. Multiplexed Phase-Encoded Lenses Written on Spatial Light Modulators. *Opt. Lett., OL* **1989**, *14* (9), 420–422. https://doi.org/10.1364/OL.14.000420.

(61) Leach, J.; Wulff, K.; Sinclair, G.; Jordan, P.; Courtial, J.; Thomson, L.; Gibson, G.; Karunwi, K.; Cooper, J.; Laczik, Z. J.; Padgett, M. Interactive Approach to Optical Tweezers Control. *Appl. Opt., AO* **2006**, *45* (5), 897–903. https://doi.org/10.1364/AO.45.000897.

(62) Polli, D.; Lüer, L.; Cerullo, G. High-Time-Resolution Pump-Probe System with Broadband Detection for the Study of Time-Domain Vibrational Dynamics. *Review of Scientific Instruments* **2007**, *78* (10), 103108. https://doi.org/10.1063/1.2800778.

(63) Spano, F. C.; Silva, C. H- and J-Aggregate Behavior in Polymeric Semiconductors. *Annual Review of Physical Chemistry* **2014**, *65* (1), 477–500. https://doi.org/10.1146/annurev-physchem-040513-103639.

(64) Polder, G.; Heijden, G. W. A. M. van der; Keizer, L. C. P.; Young, I. T. Calibration and Characterisation of Imaging Spectrographs. *J. Near Infrared Spectrosc., JNIRS* **2003**, *11* (3), 193–210.

(65) Rompotis, D.; Baumann, A.; Schepp, O.; Maltezopoulos, T.; Wieland, M.; Drescher, M. Single-Shot Nonlinear Spectroscopy in the Vacuum-Ultraviolet. *Optica, OPTICA* **2017**, *4* (8), 871–878. https://doi.org/10.1364/OPTICA.4.000871.

(66) Nishiyama, K.; Asano, Y.; Hashimoto, N.; Okada, T. Solvation Dynamics of Dye Molecules in Polar Solvents Studied by Time Resolved Hole Burning Spectroscopy. *Journal of Molecular Liquids* **1995**, *65–66*, 41–48. https://doi.org/10.1016/0167-7322(95)00843-9.

(67) Darling, S. B.; You, F. The Case for Organic Photovoltaics. *RSC Adv.* **2013**, *3* (39), 17633–17648. https://doi.org/10.1039/c3ra42989j.

(68) Janssen, R. A. J.; Nelson, J. Factors Limiting Device Efficiency in Organic Photovoltaics. *Adv. Mater.* **2013**, *25* (13), 1847–1858. https://doi.org/10.1002/adma.201202873.

(69) Walker, B.; Kim, C.; Nguyen, T.-Q. Small Molecule Solution-Processed Bulk Heterojunction Solar Cells. *Chem. Mater.* **2011**, *23* (3), 470–482. https://doi.org/10.1021/cm102189g.

(70) Mishra, A.; Baeuerle, P. Small Molecule Organic Semiconductors on the Move: Promises for Future Solar Energy Technology. *Angew. Chem.-Int. Edit.* **2012**, *51* (9), 2020–2067. https://doi.org/10.1002/anie.201102326.

(71) Brédas, J.-L.; Norton, J. E.; Cornil, J.; Coropceanu, V. Molecular Understanding of Organic Solar Cells: The Challenges. *Acc. Chem. Res.* **2009**, *42* (11), 1691–1699. https://doi.org/10.1021/ar900099h.

(72) Sirringhaus, H. 25th Anniversary Article: Organic Field-Effect Transistors: The Path Beyond Amorphous Silicon. *Adv. Mater.* **2014**, *26* (9), 1319–1335. https://doi.org/10.1002/adma.201304346.

(73) Anthony, J. E.; Facchetti, A.; Heeney, M.; Marder, S. R.; Zhan, X. N-Type Organic Semiconductors in Organic Electronics. *Adv. Mater.* **2010**, *22* (34), 3876–3892. https://doi.org/10.1002/adma.200903628.

(74) Figueira-Duarte, T. M.; Muellen, K. Pyrene-Based Materials for Organic Electronics. *Chem. Rev.* **2011**, *111* (11), 7260–7314. https://doi.org/10.1021/cr100428a.

(75) Kim, F. S.; Ren, G.; Jenekhe, S. A. One-Dimensional Nanostructures of Pi-Conjugated Molecular Systems: Assembly, Properties, and Applications from Photovoltaics, Sensors, and Nanophotonics to Nanoelectronics. *Chem. Mat.* **2011**, *23* (3), 682–732. https://doi.org/10.1021/cm102772x.

(76) Mei, J.; Hong, Y.; Lam, J. W. Y.; Qin, A.; Tang, Y.; Tang, B. Z. Aggregation-Induced Emission: The Whole Is More Brilliant than the Parts. *Adv. Mater.* **2014**, *26* (31), 5429–5479. https://doi.org/10.1002/adma.201401356.

(77) Zhong, C.; Duan, C.; Huang, F.; Wu, H.; Cao, Y. Materials and Devices toward Fully Solution Processable Organic Light-Emitting Diodes. *Chem. Mat.* **2011**, *23* (3), 326–340. https://doi.org/10.1021/cm101937p.

(78) Thejo Kalyani, N.; Dhoble, S. J. Organic Light Emitting Diodes: Energy Saving Lighting Technology—A Review. *Renewable and Sustainable Energy Reviews* **2012**, *16* (5), 2696–2723. https://doi.org/10.1016/j.rser.2012.02.021.

(79) Liu, K.; Trofod Larsen-Olsen, T.; Lin, Y.; Beliatis, M.; Bundgaard, E.; Jørgensen, M.; C. Krebs, F.; Zhan, X. Roll-Coating Fabrication of Flexible Organic Solar Cells: Comparison of Fullerene and Fullerene-Free Systems. *Journal of Materials Chemistry A* **2016**, *4* (3), 1044–1051. https://doi.org/10.1039/C5TA07357J.

(80) Sondergaard, R. R.; Hosel, M.; Krebs, F. C. Roll-to-Roll Fabrication of Large Area Functional Organic Materials. *J. Polym. Sci. Pt. B-Polym. Phys.* **2013**, *51* (1), 16–34. https://doi.org/10.1002/polb.23192.

(81) Giri, G.; Verploegen, E.; Mannsfeld, S. C. B.; Atahan-Evrenk, S.; Kim, D. H.; Lee, S. Y.; Becerril, H. A.; Aspuru-Guzik, A.; Toney, M. F.; Bao, Z. Tuning Charge Transport in Solution-Sheared Organic Semiconductors Using Lattice Strain. *Nature* **2011**, *480* (7378), 504–508. https://doi.org/10.1038/nature10683.

(82) Haverkort, F.; Stradomska, A.; Knoester, J. First-Principles Simulations of the Initial Phase of Self-Aggregation of a Cyanine Dye: Structure and Optical Spectra. *J. Phys. Chem. B* **2014**, *118* (29), 8877–8890. https://doi.org/10.1021/jp5049277.

(83) Würthner, F.; Kaiser, T. E.; Saha-Möller, C. R. J-Aggregates: From Serendipitous Discovery to Supramolecular Engineering of Functional Dye Materials. *Angewandte Chemie International Edition 50* (15), 3376–3410. https://doi.org/10.1002/anie.201002307.

(84) Pollard, W. T.; Mathies, R. A. Analysis of Femtosecond Dynamic Absorption Spectra of Nonstationary States. *Annual Review of Physical Chemistry* **1992**, *43* (1), 497–523. https://doi.org/10.1146/annurev.pc.43.100192.002433.

(85) Lanzani, G. Pump Probe and Other Modulation Techniques. In *The Photophysics Behind Photovoltaics and Photonics*; Wiley-VCH Verlag GmbH & Co. KGaA., 2012; p 177.

(86) Megerle, U.; Pugliesi, I.; Schriever, C.; Sailer, C. F.; Riedle, E. Sub-50 Fs Broadband Absorption Spectroscopy with Tunable Excitation: Putting the Analysis of Ultrafast Molecular Dynamics on Solid Ground. *Appl. Phys. B* **2009**, *96* (2–3), 215–231. https://doi.org/10.1007/s00340-009-3610-0.

(87) Giri, G.; Li, R.; Smilgies, D.-M.; Li, E. Q.; Diao, Y.; Lenn, K. M.; Chiu, M.; Lin, D. W.; Allen, R.; Reinspach, J.; Mannsfeld, S. C. B.; Thoroddsen, S. T.; Clancy, P.; Bao, Z.; Amassian, A. One-Dimensional Self-Confinement Promotes Polymorph Selection in Large-Area Organic Semiconductor Thin Films. *Nat Commun* **2014**, *5*, 3575. https://doi.org/10.1038/ncomms4573.

(88) Hernandez, J. L.; Reichmanis, E.; Reynolds, J. R. Probing Film Solidification Dynamics in Polymer Photovoltaics. *Organic Electronics* **2015**, *25*, 57–65. https://doi.org/10.1016/j.orgel.2015.05.025.

(89) Griffin, J. M.; Forse, A. C.; Tsai, W.-Y.; Taberna, P.-L.; Simon, P.; Grey, C. P. *In Situ* NMR and Electrochemical Quartz Crystal Microbalance Techniques Reveal the Structure of the Electrical Double Layer in Supercapacitors. *Nature Materials* **2015**, *14* (8), 812–820. https://doi.org/10.1038/nmat4318.

(90) Frank, O.; Dresselhaus, M. S.; Kalbac, M. Raman Spectroscopy and in Situ Raman Spectroelectrochemistry of Isotopically Engineered Graphene Systems. *Acc. Chem. Res.* **2015**, *48* (1), 111–118. https://doi.org/10.1021/ar500384p.

(91) Wilson, K. S.; Wong, C. Y. Single-Shot Transient Absorption Spectroscopy with a 45 Ps Pump-Probe Time Delay Range. *Opt. Lett., OL* **2018**, *43* (3), 371–374. https://doi.org/10.1364/OL.43.000371.

(92) Kopainsky, B.; Kaiser, W. Ultrafast Transient Processes of Monomers, Dimers, and Aggregates of Pseudoisocyanine Chloride (PIC). *Chemical Physics Letters* **1982**, *88* (4), 357–361. https://doi.org/10.1016/0009-2614(82)83025-X.

(93) Struganova, I. Dynamics of Formation of 1,1‘-Diethyl-2,2‘-Cyanine Iodide J-Aggregates in Solution. *J. Phys. Chem. A* **2000**, *104* (43), 9670–9674. https://doi.org/10.1021/jp994190f.

(94) Neumann, B. On the Aggregation Behavior of Pseudoisocyanine Chloride in Aqueous Solution as Probed by UV/Vis Spectroscopy and Static Light Scattering. *J. Phys. Chem. B* **2001**, *105* (34), 8268–8274. https://doi.org/10.1021/jp0111259.

(95) Dhar, L.; Fourkas, J. T.; Nelson, K. A. Pulse-Length-Limited Ultrafast Pump–Probe Spectroscopy in a Single Laser Shot. *Opt. Lett., OL* **1994**, *19* (9), 643–645. https://doi.org/10.1364/OL.19.000643.

(96) Salin, F.; Georges, P.; Roger, G.; Brun, A. Single-Shot Measurement of a 52-Fs Pulse. *Appl. Opt., AO* **1987**, *26* (21), 4528–4531. https://doi.org/10.1364/AO.26.004528.

(97) Fourkas, J. T.; Dhar, L.; Nelson, K. A.; Trebino, R. Spatially Encoded, Single-Shot Ultrafast Spectroscopies. *J. Opt. Soc. Am. B* **1995**, *12* (1), 155–165. https://doi.org/10.1364/JOSAB.12.000155.

(98) Weinkauf, R.; Lehr, L.; Georgiev, D.; Schlag, E. W. Time Multiplexing: A New Single Shot Femtosecond Pump-Probe Technique. *Appl Phys B* **1997**, *64* (5), 515–519. https://doi.org/10.1007/s003400050208.

(99) Fujimoto, M.; Aoshima, S.; Tsuchiya, Y. Ultrafast Imaging to Measure Instantaneous Intensity Distributions of Femtosecond Optical Pulses Propagating in a Medium. *Meas. Sci. Technol.* **2002**, *13* (11), 1698. https://doi.org/10.1088/0957-0233/13/11/306.

(100) Furukawa, N.; Mair, C. E.; Kleiman, V. D.; Takeda, J. Femtosecond Real-Time Pump–Probe Imaging Spectroscopy. *Appl. Phys. Lett.* **2004**, *85* (20), 4645–4647. https://doi.org/10.1063/1.1823039.

(101) Makishima, Y.; Furukawa, N.; Ishida, A.; Takeda, J. Femtosecond Real-Time Pump-Probe Imaging Spectroscopy Implemented on a Single Shot Basis. *Jpn. J. Appl. Phys.* **2006**, *45* (7R), 5986. https://doi.org/10.1143/JJAP.45.5986.

(102) Ferrari, R.; D'Andrea, C.; Bassi, A.; Valentini, G.; Cubeddu, R. Time-Gated Real-Time Pump-Probe Imaging Spectroscopy. In *Novel Optical Instrumentation for Biomedical Applications III 2007*; Optical Society of America, 2007; p 663118. https://doi.org/10.1364/ECBO.2007.6631_46.

(103) Harel, E.; Fidler, A. F.; Engel, G. S. Single-Shot Gradient-Assisted Photon Echo Electronic Spectroscopy. *J. Phys. Chem. A* **2011**, *115* (16), 3787–3796. https://doi.org/10.1021/jp107022f.

(104) Poulin, P. R.; Nelson, K. A. Irreversible Organic Crystalline Chemistry Monitored in Real Time. *Science* **2006**, *313* (5794), 1756–1760. https://doi.org/10.1126/science.1127826.

(105) Wakeham, G. P.; Nelson, K. A. Dual-Echelon Single-Shot Femtosecond Spectroscopy. *Opt. Lett.* **2000**, *25* (7), 505–507. https://doi.org/10.1364/OL.25.000505.

(106) Shin, T.; Wolfson, J. W.; Teitelbaum, S. W.; Kandyla, M.; Nelson, K. A. Dual Echelon Femtosecond Single-Shot Spectroscopy. *Review of Scientific Instruments* **2014**, *85* (8), 083115. https://doi.org/10.1063/1.4893641.

(107) Sakaibara, H.; Ikegaya, Y.; Katayama, I.; Takeda, J. Single-Shot Time-Frequency Imaging Spectroscopy Using an Echelon Mirror. *Opt. Lett., OL* **2012**, *37* (6), 1118–1120. https://doi.org/10.1364/OL.37.001118.

(108) Minami, Y.; Yamaki, H.; Katayama, I.; Takeda, J. Broadband Pump–Probe Imaging Spectroscopy Applicable to Ultrafast Single-Shot Events. *Appl. Phys. Express* **2014**, *7* (2), 022402. https://doi.org/10.7567/APEX.7.022402.

(109) Sorokin, A. V.; Pereverzev, N. V.; Grankina, I. I.; Yefimova, S. L.; Malyukin, Y. V. Evidence of Exciton Self-Trapping in Pseudoisocyanine J-Aggregates Formed in Layered Polymer Films. *J. Phys. Chem. C* **2015**, *119* (49), 27865–27873. https://doi.org/10.1021/acs.jpcc.5b09940.

(110) Cooper, W. Multiplet Structure of Aggregated States in 1,1′-Diethyl-2,2′-Cyanine Dye. *Chemical Physics Letters* **1970**, *7* (1), 73–77. https://doi.org/10.1016/0009-2614(70)80252-4.

(111) Fidder, H. Absorption and Emission Studies on Pure and Mixed J-Aggregates of Pseudoisocyanine. *Chemical Physics* **2007**, *341* (1), 158–168. https://doi.org/10.1016/j.chemphys.2007.06.016.

(112) Smilgies, D.-M.; Li, R.; Giri, G.; Chou, K. W.; Diao, Y.; Bao, Z.; Amassian, A. Look Fast: Crystallization of Conjugated Molecules during Solution Shearing Probed in-Situ and in Real Time by X-Ray Scattering. *Phys. Status Solidi RRL* **2013**, *7* (3), 177–179. https://doi.org/10.1002/pssr.201206507.

(113) Li, R.; Khan, H. U.; Payne, M. M.; Smilgies, D.-M.; Anthony, J. E.; Amassian, A. Heterogeneous Nucleation Promotes Carrier Transport in Solution-Processed Organic Field-Effect Transistors. *Adv. Funct. Mater.* **2013**, *23* (3), 291–297. https://doi.org/10.1002/adfm.201201264.

(114) Schmidt, L. C.; Pertegás, A.; González-Carrero, S.; Malinkiewicz, O.; Agouram, S.; Mínguez Espallargas, G.; Bolink, H. J.; Galian, R. E.; Pérez-Prieto, J. Nontemplate Synthesis of CH3NH3PbBr3 Perovskite Nanoparticles. *J. Am. Chem. Soc.* **2014**, *136* (3), 850–853. https://doi.org/10.1021/ja4109209.

(115) Li, G.; Rivarola, F. W. R.; Davis, N. J. L. K.; Bai, S.; Jellicoe, T. C.; Peña, F. de la; Hou, S.; Ducati, C.; Gao, F.; Friend, R. H.; Greenham, N. C.; Tan, Z.-K. Highly Efficient Perovskite Nanocrystal Light-Emitting Diodes Enabled by a Universal Crosslinking Method. *Advanced Materials* **2016**, *28* (18), 3528–3534. https://doi.org/10.1002/adma.201600064.

(116) Yakunin, S.; Protesescu, L.; Krieg, F.; Bodnarchuk, M. I.; Nedelcu, G.; Humer, M.; Luca, G. D.; Fiebig, M.; Heiss, W.; Kovalenko, M. V. Low-Threshold Amplified Spontaneous Emission and Lasing from Colloidal Nanocrystals of Caesium Lead Halide Perovskites. *Nat Commun* **2015**, *6* (1), 1–9. https://doi.org/10.1038/ncomms9056.

(117) Rainò, G.; Becker, M. A.; Bodnarchuk, M. I.; Mahrt, R. F.; Kovalenko, M. V.; Stöferle, T. Superfluorescence from Lead Halide Perovskite Quantum Dot Superlattices. *Nature* **2018**, *563* (7733), 671–675. https://doi.org/10.1038/s41586-018-0683-0.

(118) Dong, Y.; Zhao, Y.; Zhang, S.; Dai, Y.; Liu, L.; Li, Y.; Chen, Q. Recent Advances toward Practical Use of Halide Perovskite Nanocrystals. *J. Mater. Chem. A* **2018**, *6* (44), 21729–21746. https://doi.org/10.1039/C8TA06376A.

(119) Pan, A.; He, B.; Fan, X.; Liu, Z.; Urban, J. J.; Alivisatos, A. P.; He, L.; Liu, Y. Insight into the Ligand-Mediated Synthesis of Colloidal CsPbBr3 Perovskite Nanocrystals: The Role of Organic Acid, Base, and Cesium Precursors. *ACS Nano* **2016**, *10* (8), 7943–7954. https://doi.org/10.1021/acsnano.6b03863.

(120) Sun, S.; Yuan, D.; Xu, Y.; Wang, A.; Deng, Z. Ligand-Mediated Synthesis of Shape-Controlled Cesium Lead Halide Perovskite Nanocrystals via Reprecipitation Process at Room Temperature. *ACS Nano* **2016**, *10* (3), 3648–3657. https://doi.org/10.1021/acsnano.5b08193.

(121) Huang, H.; Xue, Q.; Chen, B.; Xiong, Y.; Schneider, J.; Zhi, C.; Zhong, H.; Rogach, A. L. Top-Down Fabrication of Stable Methylammonium Lead Halide Perovskite Nanocrystals by Employing a Mixture of Ligands as Coordinating Solvents. *Angewandte Chemie International Edition* **2017**, *56* (32), 9571–9576. https://doi.org/10.1002/anie.201705595.

(122) Peterson, M. D.; Cass, L. C.; Harris, R. D.; Edme, K.; Sung, K.; Weiss, E. A. The Role of Ligands in Determining the Exciton Relaxation Dynamics in Semiconductor Quantum Dots. *Annual Review of Physical Chemistry* **2014**, *65* (1), 317–339. https://doi.org/10.1146/annurev-physchem-040513-103649.

(123) Teunis, M. B.; Liyanage, T.; Dolai, S.; Muhoberac, B. B.; Sardar, R.; Agarwal, M. Unraveling the Mechanism Underlying Surface Ligand Passivation of Colloidal Semiconductor Nanocrystals: A Route for Preparing Advanced Hybrid Nanomaterials. *Chem. Mater.* **2017**, *29* (20), 8838–8849. https://doi.org/10.1021/acs.chemmater.7b03240.

(124) Sadighian, J. C.; Crawford, M. L.; Suder, T. W.; Wong, C. Y. Surface Ligation Stage Revealed through Polarity-Dependent Fluorescence during Perovskite Nanocrystal Growth. *Journal of Materials Chemistry C* **2020**, *8* (21), 7041–7050. https://doi.org/10.1039/C9TC06545H.

(125) Sadighian, J. C.; Crawford, M. L.; Wong, C. Y. Rapid Sampling during Synthesis of Lead Halide Perovskite Nanocrystals for Spectroscopic Measurement. *MRS Advances* **2019**, *4* (36), 1957–1964. https://doi.org/10.1557/adv.2019.263.

(126) Righetto, M.; Lim, S. S.; Giovanni, D.; Lim, J. W. M.; Zhang, Q.; Ramesh, S.; Tay, Y. K. E.; Sum, T. C. Hot Carriers Perspective on the Nature of Traps in Perovskites. *Nature Communications* **2020**, *11* (1), 2712. https://doi.org/10.1038/s41467-020-16463-7.

(127) Wang, L.; Williams, N. E.; Malachosky, E. W.; Otto, J. P.; Hayes, D.; Wood, R. E.; Guyot-Sionnest, P.; Engel, G. S. Scalable Ligand-Mediated Transport Synthesis of Organic–Inorganic Hybrid Perovskite Nanocrystals with Resolved Electronic Structure and Ultrafast Dynamics. *ACS Nano* **2017**, *11* (3), 2689–2696. https://doi.org/10.1021/acsnano.6b07574.

(128) Brus, V. V.; Lee, J.; Luginbuhl, B. R.; Ko, S.-J.; Bazan, G. C.; Nguyen, T.-Q. Solution-Processed Semitransparent Organic Photovoltaics: From Molecular Design to Device Performance. *Advanced Materials* **2019**, *31* (30), 1900904. https://doi.org/10.1002/adma.201900904.

(129) Ghani, F.; Gojzewski, H.; Riegler, H. Nucleation and Growth of Copper Phthalocyanine Aggregates Deposited from Solution on Planar Surfaces. *Applied Surface Science* **2015**, *351*, 969–976. https://doi.org/10.1016/j.apsusc.2015.06.020.

(130) Ghani, F.; Kristen, J.; Riegler, H. Solubility Properties of Unsubstituted Metal Phthalocyanines in Different Types of Solvents. *J. Chem. Eng. Data* **2012**, *57* (2), 439–449. https://doi.org/10.1021/je2010215.

(131) Paternò, G. M.; Skoda, M. W. A.; Dalgliesh, R.; Cacialli, F.; Sakai, V. G. Tuning Fullerene Intercalation in a Poly (Thiophene) Derivative by Controlling the Polymer Degree of Self-Organisation. *Scientific Reports* **2016**, *6* (1), 34609. https://doi.org/10.1038/srep34609.

(132) Miller, N. C.; Cho, E.; Gysel, R.; Risko, C.; Coropceanu, V.; Miller, C. E.; Sweetnam, S.; Sellinger, A.; Heeney, M.; McCulloch, I.; Brédas, J.-L.; Toney, M. F.; McGehee, M. D. Factors Governing Intercalation of Fullerenes and Other Small Molecules Between the Side Chains of Semiconducting Polymers Used in Solar Cells. *Advanced Energy Materials* **2012**, *2* (10), 1208–1217. https://doi.org/10.1002/aenm.201200392.

(133) Lim, J. A.; Liu, F.; Ferdous, S.; Muthukumar, M.; Briseno, A. L. Polymer Semiconductor Crystals. *Materials Today* **2010**, *13* (5), 14–24. https://doi.org/10.1016/S1369-7021(10)70080-8.

(134) Chuang, S.-Y.; Chen, H.-L.; Lee, W.-H.; Huang, Y.-C.; Su, W.-F.; Jen, W.-M.; Chen, C.-W. Regioregularity Effects in the Chain Orientation and Optical Anisotropy of Composite Polymer/Fullerene Films for High-Efficiency, Large-Area Organic Solar Cells. *J. Mater. Chem.* **2009**, *19* (31), 5554–5560. https://doi.org/10.1039/B904870G.

(135) Kohn, P.; Rong, Z.; Scherer, K. H.; Sepe, A.; Sommer, M.; Müller-Buschbaum, P.; Friend, R. H.; Steiner, U.; Hüttner, S. Crystallization-Induced 10-Nm Structure Formation in P3HT/PCBM Blends. *Macromolecules* **2013**, *46* (10), 4002–4013. https://doi.org/10.1021/ma400403c.

(136) Yin, W.; Dadmun, M. A New Model for the Morphology of P3HT/PCBM Organic Photovoltaics from Small-Angle Neutron Scattering: Rivers and Streams. *ACS Nano* **2011**, *5* (6), 4756–4768. https://doi.org/10.1021/nn200744q.

(137) Erb, T.; Zhokhavets, U.; Gobsch, G.; Raleva, S.; Stühn, B.; Schilinsky, P.; Waldauf, C.; Brabec, C. J. Correlation Between Structural and Optical Properties of Composite Polymer/Fullerene Films for Organic Solar Cells. *Advanced Functional Materials* **2005**, *15* (7), 1193–1196. https://doi.org/10.1002/adfm.200400521.

(138) Munshi, J.; Dulal, R.; Chien, T.; Chen, W.; Balasubramanian, G. Solution Processing Dependent Bulk Heterojunction Nanomorphology of P3HT/PCBM Thin Films. *ACS Appl. Mater. Interfaces* **2019**, *11* (18), 17056–17067. https://doi.org/10.1021/acsami.9b02719.

(139) Kim, J.-H.; Hwan Park, J.; Hwang Lee, J.; Soo Kim, J.; Sim, M.; Shim, C.; Cho, K. Bulk Heterojunction Solar Cells Based on Preformed Polythiophene Nanowires via Solubility-Induced Crystallization. *Journal of Materials Chemistry* **2010**, *20* (35), 7398–7405. https://doi.org/10.1039/C0JM00666A.